Dante Campagnoli Napolitano

Meso and submesoscale dynamics of the western boundary currents in the Vitória Trindade Ridge region

São Paulo

2020

Dante Campagnoli Napolitano

Meso and submesoscale dynamics of the western boundary currents in the Vitória Trindade Ridge region

A thesis submitted to the Instituto Oceanográfico of the Universidade de São Paulo in partial fulfillment for the degree of Doctor of Science, Oceanography, with emphasis in Physical Oceanography.

Advisor:
Prof. Dr. Ilson Carlos Almeida da Silveira

São Paulo

2020

NAPOLITANO, Dante Campagnoli. **Meso and submesoscale dynamics of the western boundary currents in the Vitória Trindade Ridge region**. A thesis submitted to the Instituto Oceanográfico of the Universidade de São Paulo in partial fulfillment for the degree of Doctor of Science, Oceanography, with emphasis in Physical Oceanography.

Approved on: 03 / 07 / 2020

Corrected version

Judiging committee

Prof. Dr. ____________________ Institution ____________________
President Signature ____________________

Prof. Dr. ____________________ Institution ____________________
Grade ____________________ Signature ____________________

Prof. Dr. ____________________ Institution ____________________
Grade ____________________ Signature ____________________

Prof. Dr. ____________________ Institution ____________________
Grade ____________________ Signature ____________________

I dedicate this work to my father, Menotti Zanela Napolitano, from whom I first heard the word *oceanography*.

ACKNOWLEDGEMENTS

From the day I started veering my carreer toward physical oceanography, my advisor, Ilson Silveira, supported and encouraged me in an unprecedented way. Ilson, I thank you the most. I am grateful for all the lessons, challenges, and opportunities, which will accompany me for life. Thank you for caring so much. As with all of your students, this is not a goodbye—it is just a “see you soon.”

My unnoficial co-advisor, Amit Tandon, led me into a new view of the ocean, teaching me with unequal attention and hospitality, during my stay at UMASSD. To my academically dearest friend César Rocha, thank you for being, among many other things, an example of scientific conduct. I also thank my co-authors, from whom I have learned so much, Glenn Flierl, Paulo Calil, Iury Simoes-Souza, as well as Cauê Lazaneo and Frank Smith. To all friends and colleagues not listed here, I hope you feel my gratitude everytime we meet.

And to my family, which I cannot thank enough, I owe my every success.

I acknowledge the inestimable support of the Oceanographic Institute of the University of São Paulo and all its employees. I also thank the University of Massachusetts-Dartmouth and the SMAST staff, for hosting me as a visiting scholar. This study was financed in part by Coordenação de Aperfeiçoamento de Pessoal de Nível Superior — Brasil (CAPES) — Finance Code 001. A sandwich Ph.D. fellowship was granted by project REMARSUL (CAPES: 88882.158621/2014-01). I also thank the Petróleo Brasileiro S.A. (Petrobras) for funding my last year as a Ph.D. student through the Santos Project (Petrobras: 3368).

RESUMO

NAPOLITANO, Dante Campagnoli. Dinâmica de meso e submesoescala das correntes de contorno oester na região da Cadeia Vitória-Trindade. 2020. 130 p. Tese (Doutorado). Instituto Oceanográfico, Universidade de São Paulo, São Paulo, 2020.

Este trabalho aborda a dinâmica das correntes de contorno oeste na região da Cadeia Vitória-Trindade. Primeiro, aprofundamos nossa compreensão da dinâmica da recirculação da Corrente de Contorno Intermediária (CCI) no Embaiamento de Tubarão, utilizando observações diretas inéditas, uma climatologia de flutuadores Argo, e uma simulação numérica ROMS. Com um "modelo de camada intermediá ria" quase-geostrófico (QG), mostramos que o escoamento médio do ROMS é uma boa aproximação para o estado estacionário da CCI. Uma análise mais aprofundada do ROMS revela que vórtices não-lineares se propagando para oeste entram no Embaiamento de Tubarão, descaracterizando a estacionaridade da recirculação. As perturbações são advectadas através da cadeia e interagem fortemente com a CCI, intensificando-se através do cisalhamento horizontal, à medida que negociam a topografia local. Nas camadas superiores, a Corrente Brasil (CB) meandra ciclonicamente dentro do Embaiamento de Tubarão, ocasionalmente formando o Vórtice de Vitória nas camadas acima da recirculação da CCI. Neste trabalho, nós apresentamos uma análise das observações AVISO que sugerem que a formação do Vórtice de Vitória está condicionada à força CB a montante do Embaiamento de Tubarão. Construímos um modelo QG de duas camadas (no qual a recirculação da CCI atua como uma elevação topográfica) e realizamos diferentes experimentos, variando a velocidade do jato superior. Um jato fraco meandra lentamente, desenvolvolvendo um ciclone acima do vórtice da camada inferior. Por sua vez, um jato muito forte varre as anomalias de vorticidade potencial (PV) para fora do domínio, provocando um grande crescimento das perturbações à jusante. A dinâmica que leva à formação dos vórtices na camada superior é ao mesmo tempo linear (o gatilho inicial é dado pelo vórtice da camada inferior) e não-linear (advecção à jusante e crescimento de meandros), estando intimamente relacionada à razão entre a velocidade nas camadas. Em um terceiro estudo, usando amostragem de alta resolução, capturamos a CB e CCI escoando pelos bancos e canais da Cadeia Vitória-Trindade. Uma análise da PV revela regiões de PV negativo, onde as correntes interagem com a topografia. A partir dessa interação, instabilidades se desenvolvem abaixo da camada de mistura. Em seguida, usamos uma simulação numérica ROMS de 2 km para caracterizar a sazonalidade do escoamento: enquanto os transectos sem interação direta com a topografia mostram um ciclo sazonal claro, interações corrente-topografia, gerando instabilidades abaixo da camada de mistura durante todo o ano, mascaram esta sazonalidade.

Abstract

NAPOLITANO, Dante Campagnoli. Meso and submesoscale dynamics of the western boundary currents in the Vitória Trindade Ridge region. 2020. 130 p. Phd Dissertation. Instituto Oceanográfico, Universidade de São Paulo, São Paulo, 2020.

This work adresses the dynamics of western boundary currents in the region of the Vitória-Trindade Ridge and adjacent Tubarão Bight. First, we deepen into our understanding of the dynamics of the Intermediate Western Boundary Current (IWBC) recirculation at Tubarão Bight using new direct observations, an Argo float climatology, and a ROMS numerical simulation. With a quasi-geostrophic (QG) "intermediate-layer model", we show that the ROMS time-mean flow is a good proxy for the IWBC steady state. Constrained by the Tubarão Bight topography, the IWBC recirculation is part of its steady state. Further analysis of the ROMS simulation reveals that incoming westward-propagating nonlinear eddies enter Tubarão Bight, breaking the steadiness of the flow. The perturbations are advected downstream and strongly interact with the IWBC, experiencing explosive growth through horizontal shear production as they negotiate the local topography. In the upper layers, the Brazil Current (BC) meanders cyclonically within Tubarão Bight, occasionally forming the Vitória Eddy above the topographically-constrained IWBC recirculation. We present an analysis of AVISO observations which suggest that the Vitória Eddy formation is conditioned to the BC strength upstream of Tubarão Bight. We build a simple two-layer QG model (in which the IWBC recirculation effectively acts as a topographic bump) and conduct experiments varying the upper-layer jet speed. A weak upper-layer jet slowly meanders and develops a cyclone above the lower-layer eddy. But a too-strong jet sweeps away the potential vorticity anomalies, triggering downstream meander growth. The dynamics leading to eddy formation in the upper-layer are both linear (the initial trigger by the lower-layer eddy) and nonlinear (downstream advection and meander growth), being intimately related to the ratio between the velocity in the upper and lower layers. In a third study, we downscale from the meso to the submesoscale. Using original high-resolution sampling, we capture the BC and IWBC flowing across the Vitória-Trindade Ridge banks and channels. A potential vorticity (PV) analysis reveals large patches of low and negative PV where the flows interact with topography. From this interaction, symmetric instabilites develop below the mixed-layer depth. We then use a 2-km ROMS numerical simulation to characterize the seasonality of the flow: while transects without direct interaction with topography show a clear seasonal cycle in the submesoscale, flow-topography interactions—generating unstable conditions below the mixed layer throughout the year—mask this seasonality. As captured by the observations, symmetric instabilities account for nearly all the deeper patches of unstable flow.

List of Figures

List of Tables

Contents

CHAPTER 1.

INTRODUCTION

Along the southeast Brazilian Continental Margin, the Brazil Current System (Silveira et al., 2004) separates surface and intermediate waters by two opposing flows. In the upper ocean, the poleward-flowing Brazil Current (BC), originated at about 15 °S, develops strong mesoscale activity (Soutelino et al., 2011). Underneath the BC, the Intermediate Western Boundary Current (IWBC) flows equatorward from 28 °S (Boebel et al., 1999) as part of the South Atlantic Meridional Overturning Circulation (Rintoul, 1991). These western boundary currents first encounter at 20.5 °S, in one of the main topographic features of the southwestern Atlantic, the Vitória-Trindade Ridge.

Off east Brazil, the Vitória-Trindade Ridge is a quasi-zonal seamount chain that extends 950 km into the oligotrophic center of the South Atlantic subtropical gyre. This submarine chain contains about 30 seamounts that stretch over 50 m below the ocean surface, and two islands at its easternmost end (Motoki et al., 2012). The region is a *rendezvous* point of western boundary currents, where the BC and the IWBC meet important topographic constraints when forced to negotiate the ridge's topography, generating meso and submesoscale structures (Legeais et al., 2013; Costa et al., 2017; Napolitano et al., 2019).

Strategic for Brazilian sovereignty over more than 200 nmi around the islands, the Vitória-Trindade Ridge is also a hotspot for biodiversity. Moreover, recently-found mineral reserves brought intense oil and gas exploitation to the region. At present, little is known of the hydrodynamics across the Vitória-Trindade Ridge, and the lack of observational studies poses a risk to sustainable operations in such delicate environment.

Each one of the following papers of this dissertation is posed here as a chapter. We use data from two oceanographic cruises: the spring AMBES cruise, in partnership with Petróleo Brasileiro S.A. (Petrobras), and the summer *Ilhas* cruise, part of a three-project assemblage, financed partway between the Brazilian funding agencies CNPq, CAPES, and FAPESP. We also use online-available data from the Argo project and altimetry, by AVISO. To explore the dynamics of the observed phenomena, we built theoretical quasi-geostrophic layered models and run two regional simulations, with different horizontal resolutions. The papers are independent, although intrinsically related.

In the first paper (chapter 2), we discuss the equatorward pathways of the IWBC, transporting Antarctic Intermediate Water through the eastern Brazilian Continental Margin. Specifically, we target the steadiness of the intermediate circulation across the Vitória-Trindade Ridge, showing the effects of topography on the stabilization of the IWBC recirculation within Tubarão Bight, and how incoming perturbations alter its dynamics.

The IWBC recirculation was first described by Costa et al. (2017). Napolitano et al. (2019, see chapter 2) showed the first observed velocity sections of this feature and discussed its dynamics. The second paper (chapter 3) links the upper-layer and intermediate circulations within the Vitória-Trindade Ridge region. We study the steering of the BC by the IWBC recirculation as a mechanism for triggering the BC meandering within Tubarão Bight. With a simple theoretical model, we discuss whether this effect is strong enough to deflect the BC and consequently play a role in the formation of the upper-layer Vitória Eddy (Schmid et al., 1995).

Finally, in the third and last paper (chapter 4), we downscale from the mesoscale eddies and currents into the submesoscale motions. While mesoscale features generally present low Rossby number $R_o = {}^{U}/_{fL} << 1$ and high Richardson number $R_i = {}^{N^2H}/_{U} >> 1$, submesoscale motions are characterized by R_o and R_i of order 1 in localized regions. In subtropical regions, mesoscale motions typically occur at length scales of $\mathcal{O}(10)$ km and time scales of days to weeks; embeded in the mesoscale, submesoscale motions develop at $\mathcal{O}(1)$ km, persisting from hours to days.

In the Vitória-Trindade Ridge region, the shear produced by flow-topography interactions between the BC-IWBC system and the ridge seamounts present suitable conditions for the development of submesoscale features, such as eddies and filaments. In an oligotrophic region such as the Vitória-Trindade Ridge surroundings, topographically-driven submesoscale features occurring below the mixed-layer depth could provide important water mass exchanges, fueling productivity and enhancing particle sinking in scales of time and space not yet observed in the region.

CHAPTER 2.

ON THE STEADINESS AND INSTABILITY OF THE INTERMEDIATE WESTERN BOUNDARY CURRENT BETWEEN 18 °S AND 24 °S

Manuscript published in December 2019, in the *Journal of Physical Oceanography*. This manuscript is co-authored by Ilson C. A. Silveira, Cesar B. Rocha, Glenn R. Flierl, Paulo H. R. Calil and Renato P. Martins

DOI: 10.1175/JPO-D-19-0011.1

Abstract

The Intermediate Western Boundary Current (IWBC) transports Antarctic Intermediate Water across the Vitória-Trindade Ridge (VTR), a seamount chain at ∼20° S off Brazil. Recent studies suggest that the IWBC develops a strong cyclonic recirculation in Tubarão Bight, upstream of the VTR, with weak time dependency. We herein use new quasi-synoptic observations, data from the Argo array, and a regional numerical model to describe structure and variablity of the IWBC, and to investigate its dynamics. Both shipboard-ADCP data and trajectories of Argo floats confirm the existence of the IWBC recirculation, which is also captured by our ROMS simulation. An "intermediate-layer" quasi-geostrophic (QG) model indicates that the ROMS time-mean flow is a good proxy for the IWBC steady state, as revealed by largely parallel isolines of streamfunction ($\bar{\psi}$) and potential vorticity ($\bar{Q}$); a $\bar{\psi}$-$\bar{Q}$ scatter diagram also shows that the IWBC is potentially unstable. Further analysis of the ROMS simulation reveals that remotely-generated, westward-propagating nonlinear eddies are the main source of variability in the region. These eddies enter the domain through the Tubarão Bight eastern edge and strongly interact with the IWBC. As they are advected downstream and negotiate the local topography, the eddies grow explosively through horizontal shear production.

1 Introduction

North of 28° S, off the Brazilian coast, the Antarctic Intermediate Water (AAIW) flow bifurcation sets up an equatorward-flowing Intermediate Western Boundary Current (IWBC), opposing the Brazil Current (BC) direction (Boebel et al., 1997, 1999; Legeais et al., 2013). The IWBC was first predicted by Stommel (1965) in his seminal book *The Gulf Stream* as part of the South Atlantic Meridional Overturning Circulation (MOC). Observational evidence of the IWBC and the AAIW transport, however, dates to the late 1990s and early 2000s (Boebel et al., 1997; Müller et al., 1998; Boebel et al., 1999; Schmid et al., 2000; Silveira et al., 2004; Campos, 2006). More recent investigations define the IWBC as an equatorward jet, spanning from $\sim$ 400 m to greater than $\sim$1600 m depth, that carries about 6 Sv of intermediate waters (Silveira et al., 2008; Rocha et al., 2014; Biló et al., 2014). The most well-established of those water masses is the AAIW, traced oceanwide by its low-salinity core (Wüst, 1935) and surface-referenced potential density between 1027.1 and 1027.4 $\mathrm{kg\,m^{-3}}$ (Tsuchiya et al., 1994). This northward volume flux of intermediate water closes the MOC, and thus the AAIW is an essential component of the climate system (Rintoul, 1991; Schmitz, 1995).

The Vitória-Trindade Ridge (VTR)—a quasi-zonal seamount chain at 20° S—is a western boundary current rendezvous point, where the BC and IWBC meet important topographic constraints and are forced to go through the banks, generating mesoscale (and most likely submesoscale) structures. For the IWBC, three main obstacles are the probable causes for the current to meander: Cape São Tomé, Tubarão Bight, and the VTR topographic features (fig. 2.1).

Mesoscale variability in the IWBC has been explored in the last decade by the works of Silveira et al. (2008), Mano et al. (2009), Legeais et al. (2013), and Costa et al. (2017). Silveira et al. (2008) show baroclinic instability as the main forcing mechanism for the IWBC unstable meanders. Mano et al. (2009) showed that the BC-IWBC meandering starts at the IWBC and transfers energy from intermediate to upper layers. Legeais et al. (2013) presented evidence of abundant mesoscale motions at the IWBC level north of the VTR. Costa et al. (2017) described a tight cyclonic recirculation within Tubarão Bight, which is likely to be either permanent or semi-permanent. Previous results on the IWBC include current-meter mooring velocity measurements (Evans and Signorini, 1985; Müller et al., 1998; Costa et al., 2017), numerical models (Silveira et al., 2004, 2008; Costa et al., 2017), CTD-derived velocities (Silveira et al., 2004, 2008), and Lagrangian studies (Boebel et al., 1999; Schmid and Garzoli, 2009; Legeais et al., 2013; Costa et al., 2017); however, few have solely focused on the IWBC.

Given the recent findings of Costa et al. (2017) on the stationarity and supposed quasi-steadiness of the Tubarão Bight recirculation and its impact on the dynamics of the IWBC, we formulate the following questions: (i) What is the basic state of the IWBC off southeast Brazil (24° S—18° S) and how is this basic state related to the temporal mean spatial pattern depicted from observations and numerical simulations? (ii) Which mechanisms drive the observed mesoscale variability along the IWBC path?

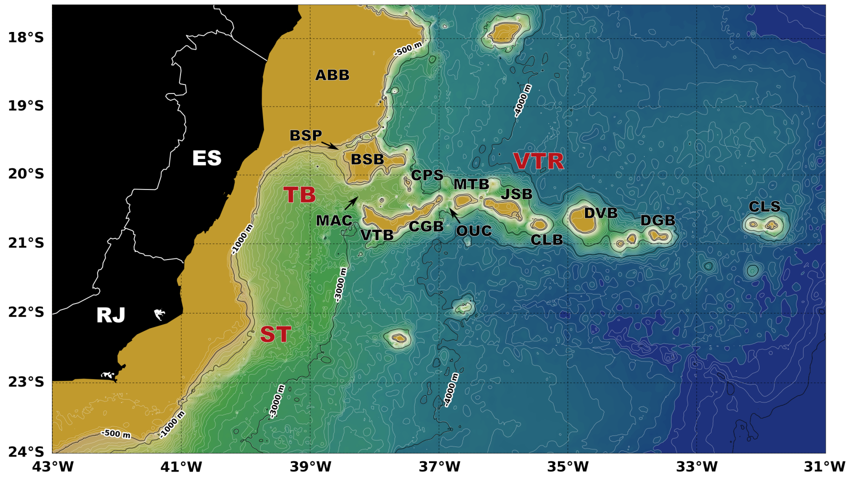

Figure 2.1: The study area and main topographic features: Cape São Tomé (ST), Tubarão Bight (TB) and Vitória-Trindade Ridge (VTR). Other keys represents the banks (ABB: Abrolhos Bank, BSB: Besnard Bank, VTB: Vitória Bank, CGB: Congress Bank, MTB: Montague Bank, JSB: Jaseur Bank, CLB: Columbia Bank, DVB: Davis Bank, DGB: Dogaressa Bank), seamounts (CPS: Champlaim Seamount, CLS: Columbia Seamount) and channels (BSP: Besnard Passage, MAC: Main Channel, OUC: Outer Channel) of the submarine chain. Bathymetry used is from the General Bathymetric Chart of the Oceans - GEBCO (Weatherall et al., 2015)

2 The intermediate circulation between 24° S and 18° S

Quasi-synoptic observations

We employ recent quasi-synoptic observations obtained in the “Marine Environment Characterization of the Espírito Santo Sedimentary Basin” Experiment (hereafter AMBES), conducted through a partnership of the Oceanographic Institute of the University of São Paulo (IOUSP) and Petróleo Brasileiro S.A. (Petrobras). The spring 2012 AMBES cruise obtained direct velocity measurements with a 38 kHz RDI shipboard Acoustic Doppler Current Profiler (ADCP), which sampled the upper 650–850 m of the water column. We processed the shipboard-ADCP data following the guidelines of Firing et al. (1995). We used 10-minute ensemble averages and discarded data with a return signal (the so-called “percent good”) below 85%. To the best of our knowledge, these are the first quasi-synoptic velocity observations within the IWBC in the VTR region.

Figure 2.2-A displays ADCP velocity observations at 600 m along the ship track, collected during the AMBES cruise. Figures 2.2-B, C and D show cross-transect velocity vertical sections for three selected transects (I, II and III). Transect I in figure 2.2-B shows a typical BC-IWBC system pattern: the opposing flows of the southward-flowing BC and the northward-flowing IWBC on the Brazilian southeast continental slope (e.g., Boebel et al., 1999; Silveira et al., 2008; Lima et al., 2016). The IWBC, which is apparently meandering in transect I, presents a core speed of $0.25\,\mathrm{m\,s^{-1}}$—the weakest measured during the cruise. (Although treated here as a meander, without additional data south of transect I we cannot rule out other possibilities, e.g., the presence of an isolated eddy by the IWBC.) The meandering of the BC-IWBC jet near Cape São Tomé and Cape Frio ($\sim$23.5° S) was also investigated by Silveira et al. (2008), Mano et al. (2009) and Rocha et al. (2014).

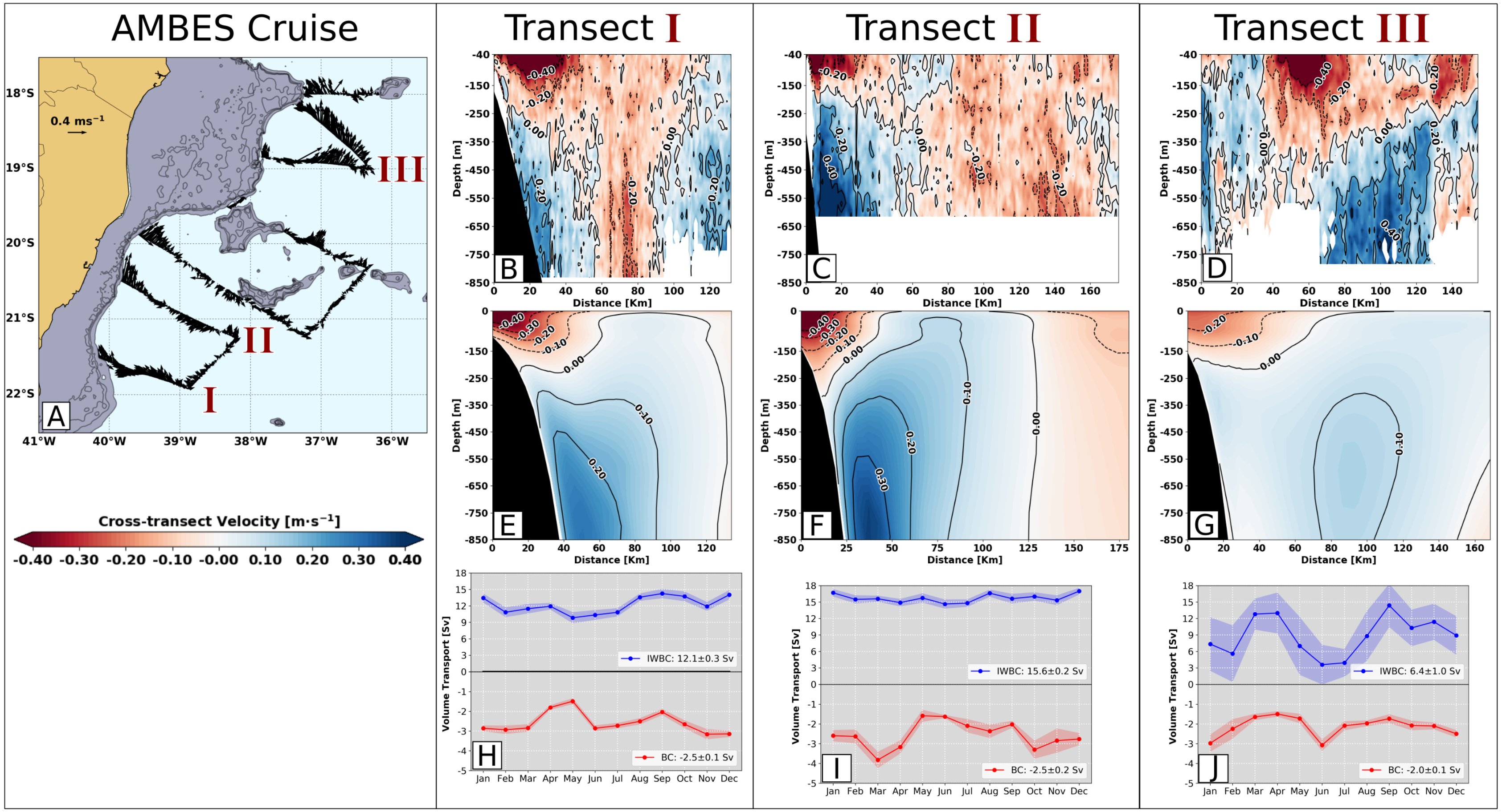

Figure 2.2: (A): Horizontal circulation pattern at 600 m (therefore within the depth range of the IWBC core layer) from shipboard-ADCP data obtained during the AMBES cruise (05-18 Oct 2012, black arrows). (B, C and D): Shipboard-ADCP vertical sections from three transects (I,II and III) of the AMBES campaign. (E, F and G): ROMS two-month averages (Sep—Oct) for the 7 years of simulation at transects I, II and III. Solid (dashed) black contours represent equatorward (poleward) velocities. (H, I and J): Monthly mean transport and associated error for the BC (red line) and the IWBC (blue line) for the ROMS simulation at transects I, II and III.

Figure 2.2-C shows that the intermediate-level circulation inside Tubarão Bight resembles a cyclone structure. The lobe adjacent to the continental margin exhibits velocities up to $0.50\,\mathrm{m\,s^{-1}}$. This pattern in transect II confirms the description by Costa et al. (2017): an IWBC cyclonic recirculation within Tubarão Bight. These authors used data from two current-meter moorings, together with Argo float trajectories and the output of a numerical model. Their findings indicated that this recirculation weakens the northward flow that crosses the VTR, and consequently intensifies the flow downstream along the western boundary. This intensification of the IWBC inside Tubarão Bight was also described by Legeais et al. (2013). Moreover, Costa et al. (2017) observed the shoaling of the IWBC within the bight, using mooring velocity data, with a mean velocity reversal depth of 370 m, but with instantaneous reversals at 150 m. As for the BC, our observations depict a $\sim$200 m-deep jet confined to the shelf break.

The IWBC crosses the VTR through a narrow channel between the Besnard and Vitória-Congress Banks, which is the main IWBC path out of the Tubarão Bight (Legeais et al., 2013; Costa et al., 2017). Transect III in figure 2.2-D captures the main branch of the intermediate current reorganized downstream of the seamounts region, where the IWBC shows strong instantaneous velocities (up to $0.48\,\mathrm{m\,s^{-1}}$) and the BC is detached from the slope.

The features presented in figure 2.2-A, B, C and D are consistent with what has been described by Silveira et al. (2004, 2008), Legeais et al. (2013), and Costa et al. (2017), namely, an organized IWBC off Cape São Tomé (transect I), a strengthened and recirculating IWBC within Tubarão Bight (transect II), and an IWBC branch reorganizing north of the VTR (transect III). However, the data are restricted to a few transects and occupied over a month. These quasi-synoptic observations include a number of transients, and thus cannot be used to assess the stationarity of the IWBC flow and its recirculation.

The regional ocean modeling experiment

To fully examine the steadiness and stability of the circulation within the AAIW layer in the study area, long time-series of potential density and velocity are required. Given the paucity of such observations in the region, we opt to answer the questions posed herein with the aid of a regional circulation experiment output. We use the Regional Ocean Modeling System (ROMS) with a configuration for the western portion of the South Atlantic ocean (41° 16' S—10° 01' S; 62° 34' W—19° 49' W). The model has a horizontal resolution of 6 km and 30 vertical levels in terrain-following coordinates, which suffices to resolve mesoscale eddies in the region. After a spin-up of 6 years, we started with the Simple Ocean Data Assimilation (SODA) temperature and salinity on 1 Jan 2000 and ran the model for seven additional years (2000–2006) using SODA fields as boundary conditions. The model is forced by climatological monthly surface wind and heat fluxes from QuikSCAT and COADS, respectively. We emphasize that our goal in using a model forced with monthly mean climatologies of wind and heat fluxes is to obtain a consistent dynamical simulation of the area rather than a hindcast simulation of the observed events.

Figures 2.2-E, F and G present the September–October cross-transect velocity averages for transects I, II and III over the 7 years of ROMS output. We also show in figure 2.2-H, I and J, 7-year monthly averages of transports of the BC and the IWBC.

The model simulated the typical BC-IWBC vertical structure in transect I (fig. 2.2-E). The modeled IWBC transport shows no significant seasonal variability and is consistent with the simulation in Costa et al. (2017). Our simulated BC transport displays two annual maxima (2.2-H), while Schmid and Majumder (2018) reported one (summer) or two (summer and spring) annual maxima.

The observed BC-IWBC structure in transect II is qualitatively well-reproduced by ROMS. As in the ADCP data, the simulated IWBC is strongest inside Tubarão Bight; this enhanced transport is present in the model, although the recirculating branch is not well captured by the simulation's transect II (compare fig. 2.2-C and F). The recirculation in ROMS is more confined within Tubarão Bight than the one inferred from Argo, as well as displaced northward (more on this in the next section). The modeled BC displays large transport monthly variations in transect II (fig. 2.2-I), most likely associated with the BC negotiating topography while crossing the VTR (cf. Costa et al., 2017).

ROMS two-month average in figure 2.2-G depicts a weak and shallow BC, with a transport of 2 Sv. Soutelino et al. (2011) characterized the BC north of the VTR as a shallow and eddy-dominated flow, consistent with our simulation. Just north of the VTR, the simulated IWBC is highly variable on a monthly time scale, alternating northward and eastward flows. The IWBC transport is largest in months of predominantly northward flow (March, April, and September); on the other hand, transport through transect III is nearly zero when the IWBC veers eastward (February, June, and July); see figure 2.2-J. Although apparently overestimated by our simulation, this eastward flow north of the VTR was previously inferred by Wienders et al. (2000) and observed by Schmid and Garzoli (2009), who qualitatively associated it with eastward penetrations of AAIW. Legeais et al. (2013) suggested a link between the weakening of the IWBC north of 20° S and an exchange of AAIW between the western boundary and the ocean interior.

Both BC and IWBC transports in our ROMS simulation match those simulated by Costa et al. (2017). The eastward flow north of the VTR is not present in the simulation in Costa et al. (2017); this is the main inconsistency between the two models. In a literature survey presented in table 2.1, we detail a comparison between previous estimates of the BC/IWBC transports and our study.

The Argo float climatology

Given that the parking depths of Argo floats lie within the IWBC domain, we can use float trajectories to characterize the time-mean velocity pattern near the VTR (26° S— 16° S; 43° W—32° W). We obtained the Argo dataset from the AOML database (`http://tds0.ifremer.fr/thredds/catalog/CORIOLIS-ARGO-GDAC-OBS/aoml/catalog.html`) and selected floats that entered the domain from Jan 2000 through Apr 2019, drifting within the IWBC with parking depths between 600 and 1100 m.

We determined the location and period of an Argo cycle by the middle point of the float trajectory and its duration, respectively. (Figure 2.3 shows the spatial distribution of the number of Argo observations on a 12.5×12.5-km grid.) We identify each Argo cycle in the float trajectory and treat it as an independent sample. In doing so, we eliminate surface drift during data transmission and ignore the short profiling time (Park et al., 2005). Also, floats that dwelt for too short (<5 days) or too long (>15 days) in their parking depths were removed from the analysis. These criteria yield 5503 cycles from 90 floats that occupied the region, with an average cycle of 9.6 ± 0.18 days.

Table 2.1: Comparison between the AMBES cruise, ROMS outputs, and literature. ADCP transports are restricted to the depth-range presented Figure 2.2-B, C and D. And ROMS transports are averaged for the simulation period (7 years) in virtually the same ADCP transect position. Positive (negative) values indicate northward (southward) volume transport. Transport estimates are in Sverdrups [10^6 m^3 s^{-1}]. Keys: BC-Brazil Current; IWBC-Intermediate Western Boundary Current. REMO- Brazilian HYbrid Coordinate Ocean Model 1/12° run.

BC	**Data**	**Latitude (°S)**	**Transport (Sv)**
Schmid and Majumder (2018)	Argo/SSH	24	-2.3
Silveira et al. (2004)	Pegasus profiler	23	-5.6 ± 1.4
Mata et al. (2013)	hydrographic	22	-2.3
This study (Transect I)	ADCP	21.5	-2.4
This study (Transect I)	ROMS	21.5	-2.5 ± 0.1
This study (Transect II)	ADCP	20.5	1.0
This study (Transect II)	ROMS	20.5	-2.5 ± 0.2
Evans et al. (1983)	hydrographic	20	3.8
Stramma et al. (1990)	hydrographic	20	1.6
This study (Transect III)	ADCP	19	4.5
This study (Transect III)	ROMS	19	-2.0 ± 0.1
IWBC	**Data**	**Latitude (°S)**	**Transport (Sv)**
Boebel et al. (1999)	floats	28–02	4.0 ± 2.0
Müller et al. (1998)	current meter	23	1.3
Silveira et al. (2004)	Pegasus profiler	23	3.6 ± 0.8
Silveira et al. (2008)	hydrographic	23	3.0
Costa et al. (2017)	REMO	22	12.0 ± 5.0
This study (Transect I)	ADCP	21.5	2.4
This study (Transect I)	ROMS	21.5	12.0 ± 0.3
This study (Transect II)	ADCP	20.5	3.7
This study (Transect II)	ROMS	20.5	12.0 ± 0.2
Schmid and Garzoli (2009)	floats	20	10
This study (Transect III)	ADCP	19	6.5
This study (Transect III)	ROMS	19	6.4 ± 1.0

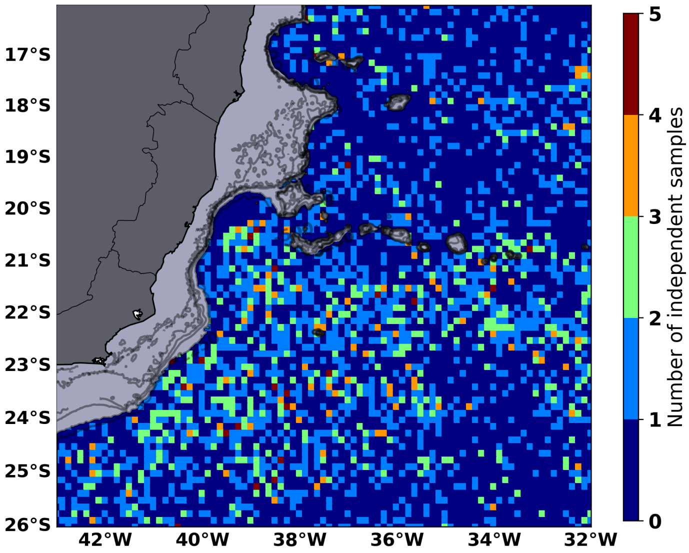

Figure 2.3: Spatial distribution of the number of samples per cell in the 12.5 x 12.5-km grid, from 5503 Argo cycles used to estimate the Argo-derived velocity.

We estimate horizontal velocity (u and v) at the parking depth from the position difference between the end and the beginning of each cycle divided by the average parking time (Lebedev et al., 2007). We then interpolate the parking-depth velocity onto a 12.5×12.5-km grid. Figure 2.3 shows that the Argo array presents good coverage in the region compared to previous datasets, but the number of Argo cycles per grid point is still small, particularly north of the VTR.

We calculate the streamfunction $\bar{\psi}$ by solving the elliptic equation

$$(\partial_x^2 + \partial_y^2)\bar{\psi} = \underbrace{v_x - u_y}_{\stackrel{\text{def}}{=}\zeta}\,, \tag{2.1}$$

where

$$(\bar{u}, \bar{v}) = (-\bar{\psi}_y, \bar{\psi}_x)\,. \tag{2.2}$$

We solve for the streamfunction $\bar{\psi}$ given the vorticity $v_x - u_y$ in (2.1) using a Fourier spectral method:

$$\hat{\psi} = \begin{cases} -\dfrac{\hat{\zeta}}{k^2 + l^2}\,, & k^2 + l^2 \neq 0\,, \\ 0 \quad , & k = l = 0\,, \end{cases} \tag{2.3}$$

where $\hat{\psi}$ is the Fourier transform of the streamfunction, $\hat{\zeta}$ is the Fourier transform of the relative vorticity, and (k, l) is the wavevector. Before calculating $\hat{\zeta}$, we periodize ζ using mirror reflections to obtain a doubly-periodic field (e.g., Isern-Fontanet et al., 2006). Next, we smooth $\bar{\psi}$ with a Gaussian filter (1.5 std) and enforce zero streamfunction in regions shallower than 700 m. Finally, we ensure that the gridded velocity preserves the variance of the float-derived velocity by multiplying the Argo-derived velocity by σ_a/σ_g, where σ_a is the RMS Argo velocity and σ_g is the RMS nondivergent velocity. Horizontal scales of the Argo gridded velocity (12.5 km) and the sampling time scales of the Argo array ($\sim$10 days) yield approximately geostrophic velocities, with maximum velocities ($\sim$0.30 $\mathrm{m\,s^{-1}}$) 12 % weaker than the maximum instantaneous Argo velocities ($\sim$0.34 $\mathrm{m\,s^{-1}}$).

The Argo-derived flow (fig. 2.4-A) depicts the IWBC flowing northward along the continental slope with maximum speed of $\sim$0.30 $\mathrm{m\,s^{-1}}$. Argo climatological speeds are close to the Costa et al. (2017) mooring time averages. Müller et al. (1998) analyzed moorings in the region, with mean velocities ranging from 6 to 21 $\mathrm{cm\,s^{-1}}$, both in the same ballpark as our estimates. Near Tubarão Bight northern limit, the flow splits into two branches, one exiting the bight flowing northward (Legeais et al., 2013; Costa et al., 2017), and the other veering southward and forming a cyclonic recirculation. This Argo climatology does not display an intermediate flow through the Besnard Passage, in contrast to the strong synoptic flow observed in the AMBES ADCP survey (fig. 2.2-A) and two RAFOS float trajectories that exited the bight through this passage (Legeais et al., 2013).

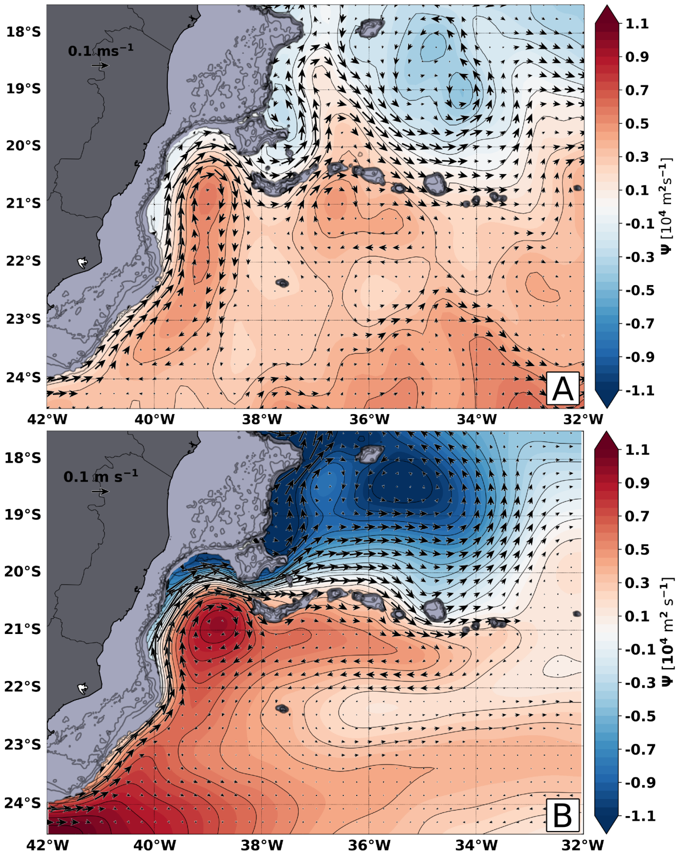

Figure 2.4: (A) Streamfunction (contours) and nondivergent velocity (arrows) inferred from Argo displacements within each cycle for the 2000-2019 period in the AAIW layer. (The grid resolution is 1/8°.) (B) Streamfunction (contours) and nondivergent velocity (arrows) calculated from ROMS for the 2000-2006 period in the AAIW layer. (The grid resolution is 1/16°.)

Comparison between Argo float climatology and ROMS

The horizontal mean velocity of our ROMS simulation is qualitatively consistent with the Argo intermediate circulation pattern (compare panels A and B of fig. 2.4). ROMS maximum velocities are 25% larger than maximum Argo velocities, and these quantitative differences are likely due to the smoothing nature of the trajectory-based Argo velocity (an average over 9.6 days and 12.5×12.5-km) compared to ROMS's daily snapshots on a 6-km horizontal grid.

According to the Argo estimates, about 58% of the flow that enters Tubarão Bight at Cape São Tomé exits it through the main channel; the remaining 42% recirculates. In

ROMS, 70% of the flow exits the bight through the main channel, and the remaining 30% recirculates. The flow that crosses the ridge through the main channel bifurcates: 58% flows north and 42% veers eastward. Similarly to ROMS, Argo presents an eastward flow between 36°–34° W. But Argo does not clearly depict a zonally elongated recirculation, which in ROMS extends east of Tubarão Bight and around the VTR for 400 km. As mentioned earlier, our simulation may be overestimating this eastward flow and, owing to paucity of observations, care must be taken in interpreting model results north of the VTR (see fig. 2.3 and the discussion of data density in Schmid and Garzoli, 2009).

Two mesoscale features appear in the lee of the VTR between ∼18–20° S: a cyclone centered at ∼37° W and a larger anticyclone at ∼35° W, off the Abrolhos Bank. Legeais et al. (2013) noted that some floats stalled for a long time off the Abrolhos Bank. Those floats were probably trapped by these features.

3 The IWBC steady state in the vicinity of the VTR

In the previous section, we show that mesoscale features appear in the time-mean IWBC flow. Are these time-mean features the result of strong unsteady eddies? Or are they permanent structures caused by the topographic steering of the IWBC?

If the mesoscale features are steady, then the flow should occur along potential vorticity contours (e.g., Bretherton and Haidvogel, 1976). On the other hand, mean potential vorticity contours cross streamlines when mesoscales features are unsteady (e.g., Vallis, 2017). To address this question, we formulate an intermediate-layer quasi-geostrophic model within the AAIW layer (1027.1–1027.4 kg m^{-3}; Tsuchiya et al., 1994). We diagnose quasi-geostrophic streamfunction ψ and potential vorticity Q, and investigate the properties of the mean flow using $\psi - Q$ scatter diagrams (Bretherton and Haidvogel, 1976; Read et al., 1986).

Model formulation

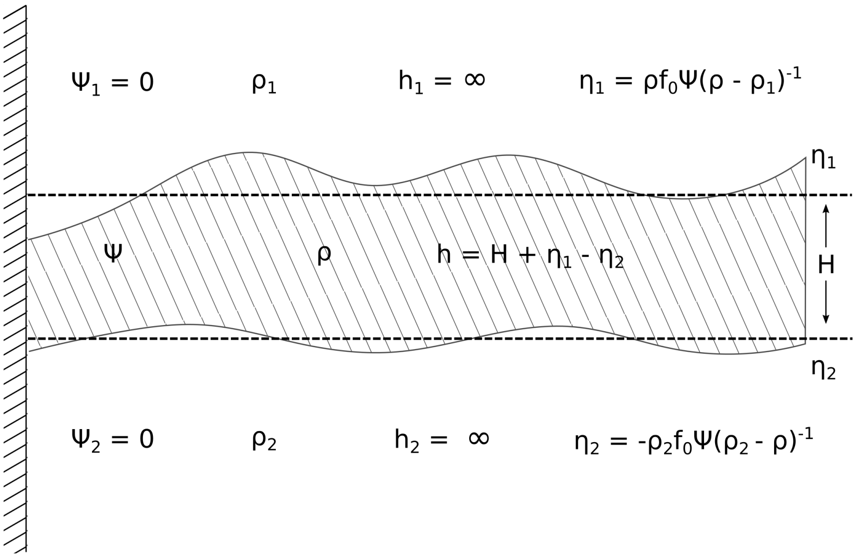

Figure 2.5: Representation of the intermediate layer model configuration: both upper and lower layers are infinite and have no motion. ρ represents density in kg m^{-3}. *H* represents the mean layer depth, and η represents the upper and lower boundaries.

The intermediate-layer model consists of three immiscible layers, with the intermediate layer—which contains all the flow—sandwiched by two stagnant, semi-infinite layers with $\psi = 0$ (see fig. 2.5). The potential vorticity in the model is given by

$$\begin{aligned} Q_1 &= \beta y \,, \\ Q &= \left(\nabla^2 - \frac{1}{R_d^2}\right)\psi + \beta y \,, \\ Q_2 &= \beta y \,, \end{aligned} \tag{2.4}$$

where β is the planetary potential vorticity gradient, and R_d is the deformation radius (details in the estimation of $g\prime$ are given in appendix A),

$$R_d^2 \overset{\text{def}}{=} \underbrace{\left(\frac{\rho - \rho_1}{\rho_2 - \rho_1}\right)\left(\frac{\rho_2 - \rho}{\rho}\right)}_{\overset{\text{def}}{=} g\prime/g} \frac{gH}{f_0^2} \,. \tag{2.5}$$

The planetary vorticities Q_1 and Q_2 have no dynamical role in the system (Silveira and Flierl, 2002). The total potential vorticity Q and streamfunction ψ can be split into a steady solution and a time-dependent perturbation:

$$\psi(x,y,t) = \bar{\psi}(x,y) + \tilde{\psi}(x,y,t)\,, \tag{2.6}$$

$$Q(x,y,t) = \bar{Q}(x,y) + \tilde{Q}(x,y,t)\,. \tag{2.7}$$

We are interested in the steady part of the flow, particularly the relation between $\bar{\psi}$ and $\bar{Q}$. As the flow enters a “free-mode” configuration, $\bar{\psi}$ and $\bar{Q}$ become correlated (Bretherton and Haidvogel, 1976):

$$\bar{Q} = \bar{Q}(\bar{\psi})\,. \tag{2.8}$$

From (2.8) follows the definition

$$J(\bar{\psi},\bar{Q}) \overset{\text{def}}{=} \bar{\psi}_x\bar{Q}_y - \bar{\psi}_y\bar{Q}_x = 0\,. \tag{2.9}$$

To assess whether the mean IWBC satisfies the zero Jacobian condition (2.9), we use the time-mean flow defined as a 7-year average of the ROMS output within the the AAIW layer.

The steady solution

Figure 2.6 shows the streamfunction $\bar{\psi}$ (fig. 2.4-B) overlaid on contours of quasi-geostrophic potential vorticity $\bar{Q}$ in (2.4), both calculated from ROMS; colors represent the Jacobian in (2.9) normalized by $|\nabla\bar{\psi}|\,|\nabla\bar{Q}|$. The quasi-geostrophic potential vorticity is nearly parallel to the streamfunction. Hence, the Jacobian is very small within the IWBC on the continental slope and in the recirculation within Tubarão Bight, indicating a steady geostrophic flow. However, it is fairly large in patches where the current is known to meander vigorously (see fig. 2.2) and in regions where the mean current is weak. This basic state shows the main path by which AAIW is transported equatorward to join the MOC downstream of our study region.

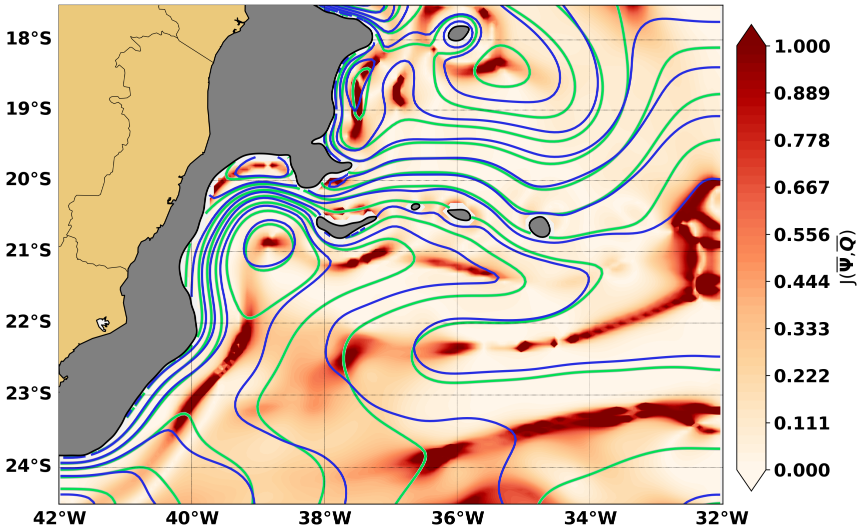

Figure 2.6: $\bar{\psi}$ $vs.$ $\bar{Q}$ mean state for the IWBC, averaged for the AAIW layer, between the 1027.1 and 1027.4 kg m^{-3} isopycnals. Blue lines represent streamfunction $\bar{\psi}$, green lines represent potential vorticity $\bar{Q}$), and background colors represent the normalized Jacobian $J(\bar{\psi}, \bar{Q})/(|\nabla\bar{\psi}|\,|\nabla\bar{Q}|)$.

Also about the IWBC steadiness, we observe a quasi-linear relation between $\bar{\psi}$ and $\bar{Q}$ (fig. 2.7), which confirms that the mean flow is largely steady, and therefore the time-mean potential vorticity can be calculated from the time-mean flow using the relation

$$\bar{Q}(\bar{\psi}) = \alpha\,\bar{\psi}\,, \tag{2.10}$$

where α is a constant. A linear fit gives $\alpha = -3.84 \times 10^{-9}\,\mathrm{m}^{-2}$. Small curvatures in figure 2.7 hint at two distinct regions (northern and southern parts of the domain) and a slightly nonlinear $\bar{Q}(\bar{\psi})$.

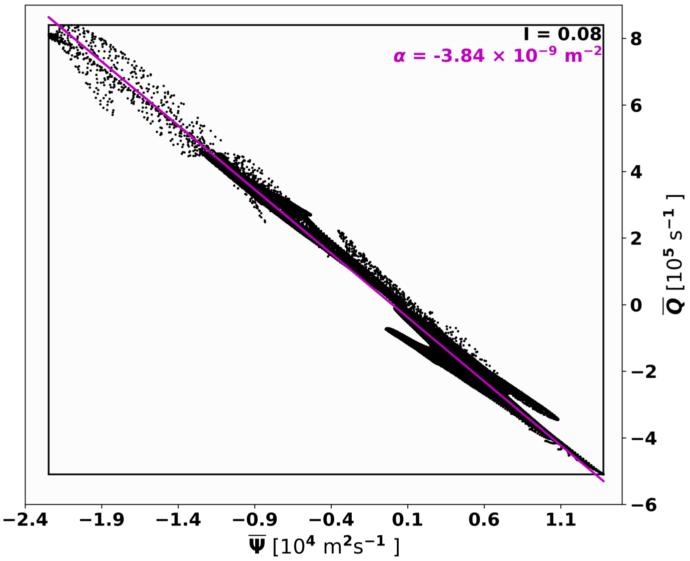

Figure 2.7: $\bar{\psi} \times \bar{Q}$ scatter diagram for the IWBC, averaged for the AAIW layer, between the 1027.1 and 1027.4 $\mathrm{kg\,m^{-3}}$ isopycnals. *I* is the free-mode departure index.

Stability of the steady state

The scatter about the straight line $\bar{Q} = \alpha\bar{\psi}$ quantifies the steadiness of the flow. In particular, Read et al. (1986) define an index of departure from the free-form mode:

$$I \overset{\text{def}}{=} \frac{A}{\Delta\psi\Delta Q} = \frac{\text{area enclosed on the } (\psi, Q) \text{ diagram}}{\text{area of the circumscribing rectangle}} . \tag{2.11}$$

A purely steady state has no scatter, and therefore *I*=0, while a strong unsteady flow presents large scatter, with *I* approaching 1. In figure 2.7, $I = 0.08$ indicating that the steady part of the flow is largely dominant. Details in estimating (2.11) and its caveats are discussed in Read et al. (1986) and in appendix B.

Focusing on smaller regions along the IWBC path, different values of *I* occur according to the flow characteristics: We see values in the Cape São Tomé region higher than in the recirculation and in the main channel, which is explained by the rich and frequent meandering activity of the IWBC that adds perturbation terms and weakens the mean flow (Silveira et al., 2008). This also implies that the flow in the vicinity of Tubarão Bight is steadier ($I = 0.05$, not shown).

The $\bar{\psi} - \bar{Q}$ scatterplot also sheds light on the stability of nonparallel flows such as the IWBC (Read et al., 1986). In particular, the flow is stable if $d\bar{Q}/d\bar{\psi} > 0$ (Arnold's theorem, e.g., Blumen, 1968; Read et al., 1986). Figure 2.7 shows that $\bar{\psi}$ and $\bar{Q}$ are negatively correlated, and thus the flow is potentially unstable.

So far, we have shown that the time-mean IWBC is representative of the steady state, although instabilities may be present. Hence, we shall ask: do local conversions account for all the variability? Or is the variability driven by remote forcing? We next address these questions, using a detailed analysis of the energetics of the eddy-mean flow interactions of the IWBC.

4 Energetics of the eddy-mean flow interaction

We follow Vallis (2017) in performing a standard eddy-mean flow interaction analysis. The dynamical fields are decomposed into mean and eddy components:

$$\theta(x, y, z, t) = \bar{\theta}(x, y, z, \bar{t}) + \tilde{\theta}(x, y, z, t)\,. \tag{2.12}$$

Here, the overbar denotes an average over fast time, so $\bar{\theta}$ varies on a slow time; operationally, we use a low-pass frequency filter of 60 days.

The total mechanical energy (E_T) is the sum of four components

$$E_T = P_m + P_e + K_m + K_e\,, \tag{2.13}$$

where

$$P_e \stackrel{\text{def}}{=} \frac{\tilde{b}^2}{2N^2} \qquad \text{and} \qquad K_e \stackrel{\text{def}}{=} \frac{1}{2}(\tilde{u}^2 + \tilde{v}^2)\,, \tag{2.14}$$

are the eddy available potential energy and the eddy kinetic energy. Above, (u, v) is the horizontal velocity, $b \stackrel{\text{def}}{=} -g\rho/\rho_0$ is the buoyancy and N is the Brünt-Väisälä frequency.

The mean available potential energy P_m and kinetic energy K_m are defined analogously to (2.14).

In oceanography, we must use density (buoyancy) to calculate the potential energy budget, especially in cases where salinity plays a major role in the fluid density, as in the AAIW. The potential energy above is only an exact definition for constant N^2 (Huang, 2005).

Energy conservation equations

Redistribution of energy across the eddy-mean reservoirs occurs through processes of barotropic, baroclinic, and mixed instability (Gill et al., 1974; Hart, 1974). The eddy kinetic energy and eddy potential energy conservation equations are given by

$$\partial_{\bar{t}} K_e + \boldsymbol{\nabla} \cdot (\mathbf{F}_e + \mathbf{P}_w) = -\overline{HSP} - \overline{VSP} + \overline{\tilde{w}\tilde{b}}\,, \tag{2.15}$$

$$\partial_{\bar{t}} P_e + \boldsymbol{\nabla} \cdot \mathbf{G}_e \approx -\overline{HBP} - \overline{VBP} - \overline{\tilde{w}\tilde{b}}\,. \tag{2.16}$$

Equations (2.15) and (2.16) are the budgets most relevant to our discussion below; table 2.2 contains a detailed description of each term. For a derivation of these energy budgets see, e.g., Vallis (2017).

Table 2.2: Main terms from the eddy energy conservation equations. Keys: $\mathbf{u} = (u, v, w)$ - velocity vector; ∇ - gradient operator; Ψ - horizontal streamfunction; N^2 - buoyancy frequency; p - pressure; b - buoyancy. Subscripted indices indicate derivatives.

Term	**Mathematical form**	**Effects**
HSP	$(\overline{\tilde{v}^2 - \tilde{u}^2})\psi_{xy} + \overline{\tilde{u}\tilde{v}}\,(\psi_{xx} - \psi_{yy})$	horizontal shear production
VSP	$\overline{\tilde{u}\tilde{w}}\,\bar{u}_z + \overline{\tilde{v}\tilde{w}}\,\bar{v}_z$	vertical shear production
HBP	$\frac{1}{N^2}(\overline{\tilde{u}\tilde{b}}\,\bar{b}_x + \overline{\tilde{v}\tilde{b}}\,\bar{b}_y)$	horizontal buoyancy production
VBP	$\frac{1}{N^2}\overline{\tilde{w}\tilde{b}}\,\bar{b}_z$	vertical buoyancy production
$\tilde{w}\tilde{b}$	$\tilde{w}\tilde{b}$	vertical buoyancy flux
$\nabla\cdot\mathbf{F}_e$	$\nabla\cdot\frac{1}{2}\overline{\boldsymbol{u}(\tilde{u}^2 + \tilde{v}^2)}$	redistribution of K through advection
$\nabla\cdot\mathbf{P_w}$	$\nabla\cdot\tilde{u}\tilde{p}$	redistribution of K through pressure work
$\nabla\cdot\mathbf{G}_e$	$\nabla\cdot\frac{\overline{\boldsymbol{u}\tilde{b}^2}}{2N^2}$	redistribution of P through advection

The time-varying budgets on the left side of (2.15) and (2.16) depend on the balance between the divergence of energy at the boundaries of the domain and the local energy production on their right-hand side. The conversion terms on the right quantify the transformations between the different forms of energy. The terms SP $\overset{\text{def}}{=} (\overline{\text{HSP}} + \overline{\text{VSP}})$ are associated with shear instabilities, and the BP $\overset{\text{def}}{=} (\overline{\text{HBP}} + \overline{\text{VBP}})$ terms are associated with eddy buoyancy fluxes (e.g., Chen et al., 2014). The vertical buoyancy flux $(\overline{\tilde{w}\tilde{b}})$ associated with the energy pathway $P_m \to P_e \to K_e$ is a telltale signal of baroclinic instability processes (e.g., Pedlosky, 1987). These processes—among others detailed below—are represented here in an eddy-focused version of the traditional Lorenz diagram (fig. 2.8).

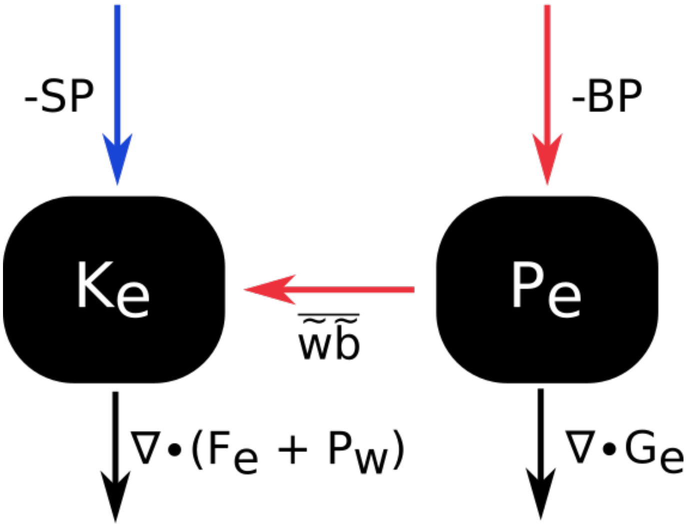

Figure 2.8: The modified Lorenz energy diagram focusing on eddy components of the eddy-mean flow interactions. Blue lines indicates the barotropic instability pathway; red lines indicate the baroclinic instability pathway, and black lines represent the redistribution of energy through the borders of the domain. Keys are SP $\overset{\text{def}}{=}$ $(\overline{\text{HSP}} + \overline{\text{VSP}})$ shear production; BP $\overset{\text{def}}{=}$ $(\overline{\text{HBP}} + \overline{\text{VBP}})$ buoyancy production; $\overline{\tilde{w}\tilde{b}}$ = vertical buoyancy flux; F_e = kinetic energy advection; P_w = pressure work; G_e = potential energy advection.

The flux divergence terms $\mathbf{G}_e$, $\mathbf{F}_e$ and $\mathbf{P}_w$ account for the redistribution of eddy energy through advection and pressure work. Although not computed explicitly, the residual term that represents horizontal and vertical mixing, heat and freshwater fluxes, wind forcing, and bottom drag is included to close the energy balance (Chen et al., 2014).

We calculate energy budgets in the IWBC using ROMS daily outputs to estimate the conversion and redistribution terms in table 2.2. We vertically average ROMS fields within the AAIW layer (1027.1 – 1027.4 $\mathrm{kg\,m^{-3}}$; Tsuchiya et al., 1994) and apply the decomposition (2.12) to the resulting 2D fields (terms with z-dependence are calculated prior to averaging). We define the eddy component as variability with timescales shorter than 60 days.

Energy conversions

Existing studies of the BC-IWBC system energetics focused on regions south of the VTR, restricted either to Cape São Tomé and Cape Frio (e.g., Mano et al., 2009) or to southeast Brazil (e.g., Oliveira et al., 2009; Magalhães et al., 2017). Those studies showed that baroclinic conversions account for most of the eddy generation, though barotropic conversions may be important in some regions.

Here, both barotropic and baroclinic conversions are at play (see fig. 2.9). In particular, barotropic conversion through horizontal shear production (HSP) is larger where the IWBC splits into two branches near the exit from Tubarão Bight and off the Abrolhos Bank (see fig. 2.9-A). Baroclinic conversion, through horizontal buoyancy production (HBP), is also enhanced north of the VTR; HSP is twice as large as HBP. Vertical conversions, through vertical shear production (VSP) and vertical buoyancy production (VBP), are small over most of the region but large near seamounts, becoming important in the energy budget of subregions such as Tubarão Bight. In the ocean, this is associated with enhanced vertical mixing (e.g., Polzin et al., 1997).

The theoretical analysis of section 3 suggests that the region south of the VTR is prone to instabilities of the IWBC mean flow, yet the energetics of the numerical model in this section show that most conversions occur north of the VTR. To solve this apparent contradiction, we next look into the details of the model output within the Tubarão Bight region.

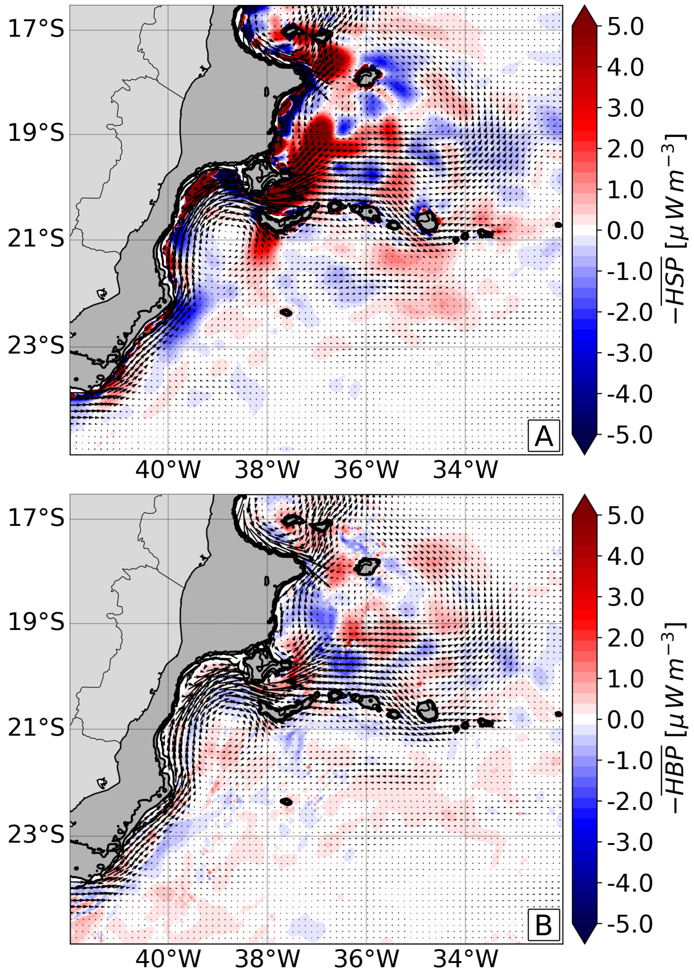

Figure 2.9: (A) Horizontal shear production: positive values indicate conversion from K_m to K_e due to barotropic instability processes. (B) Horizontal buoyancy production: positive values indicate conversion from P_m to P_e due to baroclinic instability processes. Arrows represent the mean model velocity.

Breaking the steadiness

Figure 2.10-C shows a Hovmöller diagram of ROMS meridional eddy velocity along the path in figure 2.10-A. We average $\tilde{v}$ along this envelope from the easternmost seamount at ∼32° W to the continental margin at ∼40° W, along the mean IWBC streamline within Tubarão Bight and downstream of the VTR at 19.5° S. Encompassing a larger area compared to a single path allows us to track perturbations advected by the IWBC which follow different paths within Tubarão Bight and grow in distinct regions downstream of the VTR. We also show the horizontal shear production (HSP) and

the cumulative HSP along this path in figure 2.10-B. Throughout the model time series, tilted alternating velocity patterns indicate perturbations propagating along the 22° S path, eventually reaching the continental margin in Tubarão Bight. Quasi-zonal bands of $\tilde{v}$ between 822 and 1001 km show a sudden increase in phase-velocity as the IWBC advects perturbations downstream of the VTR. Those perturbations trigger eddy-mean flow interactions, mostly by barotropic conversions (fig. 2.10-B). This interaction mechanism yields mean-to-eddy energy transfers through standard Reynolds-stress horizontal shear production (e.g., Vallis, 2017). These results are consistent with those of Mata et al. (2006), which, during eddy-shedding events of the East Australian Current, revealed the downstream growth of perturbations through horizontal shear production.

We track one of the strongest perturbation events in the simulation (fig. 2.11). This perturbation is enhanced at ∼36° W on 1 May 2002 (see fig. 2.11-A) and propagates westward at 4.47 km day^{-1}. About 25 days after this enhancement at ∼36° W, an anticyclonic structure begins to approach the eastern limit of Tubarão Bight (see fig. 2.11-B). Within the bight, the ring propagates to the southwest through the time-mean flow; the eddy velocity is perpendicular to the time-mean flow (see vectors and streamlines in fig. 2.11-C). Once the ring reaches the western boundary, it is strained by the mean flow and quickly advected downstream (see fig. 2.11-D). The perturbation grows significantly as it crosses the VTR, generating a strong eddy field north of the ridge (fig. 2.11-E and F). (This sequence of events occurs for most of the perturbations seen in the Hovmöller diagram.) The strong eddy field off the Abrolhos Bank is consistent with the swirly float trajectories reported by Legeais et al. (2013).

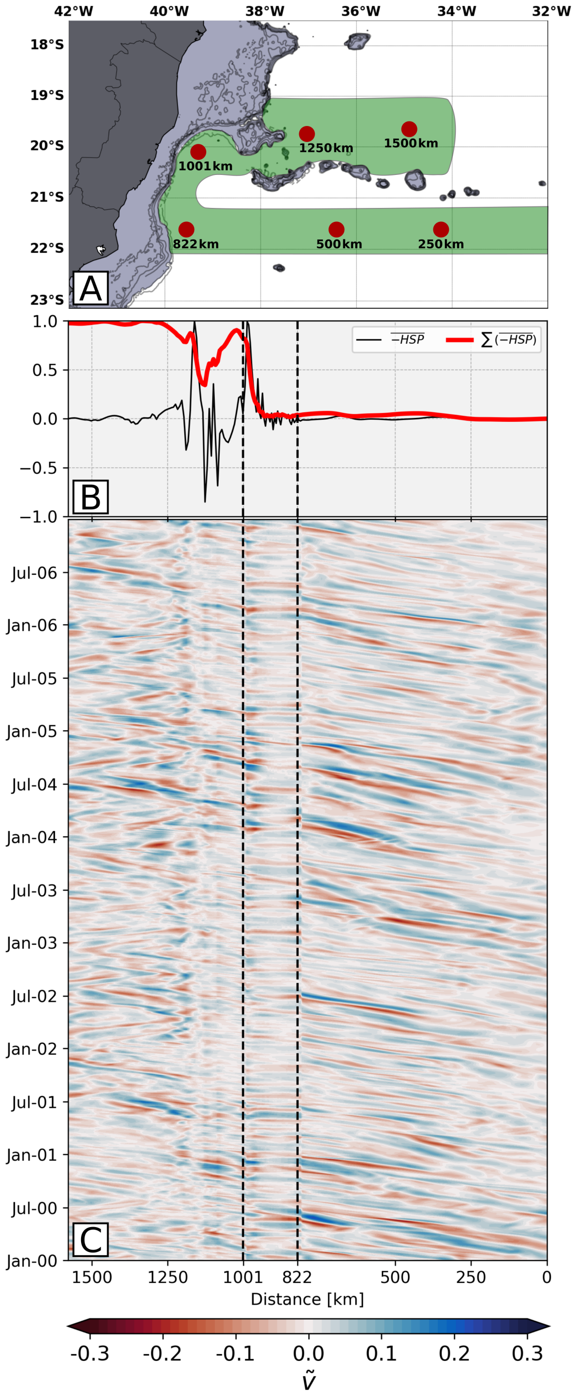

Figure 2.10: (A) Hovmöller diagram path including the zonal transect in 22°S, the IWBC path within Tubarão Bight and a 19.5°S transect north of the Vitória-Trindade Ridge. We averaged $\tilde{v}$ within this 22°S-IWBC-19.5°S path to capture different trajectories followed by perturbations advected by the IWBC. (B) Horizontal shear production (HSP) and cumulative HSP along the 22°S-IWBC-19.5°S path. Positive (negative) values in HSP indicate mean-eddy (eddy-mean) kinetic energy conversion. (C) Hovmöller diagram of $\tilde{v}$ along the 22°S-IWBC-19.5°S path. Tilted crests and troughs indicate propagation of perturbations. Dashed lines at 822 km and 1001 km show the limits of Tubarão Bight.

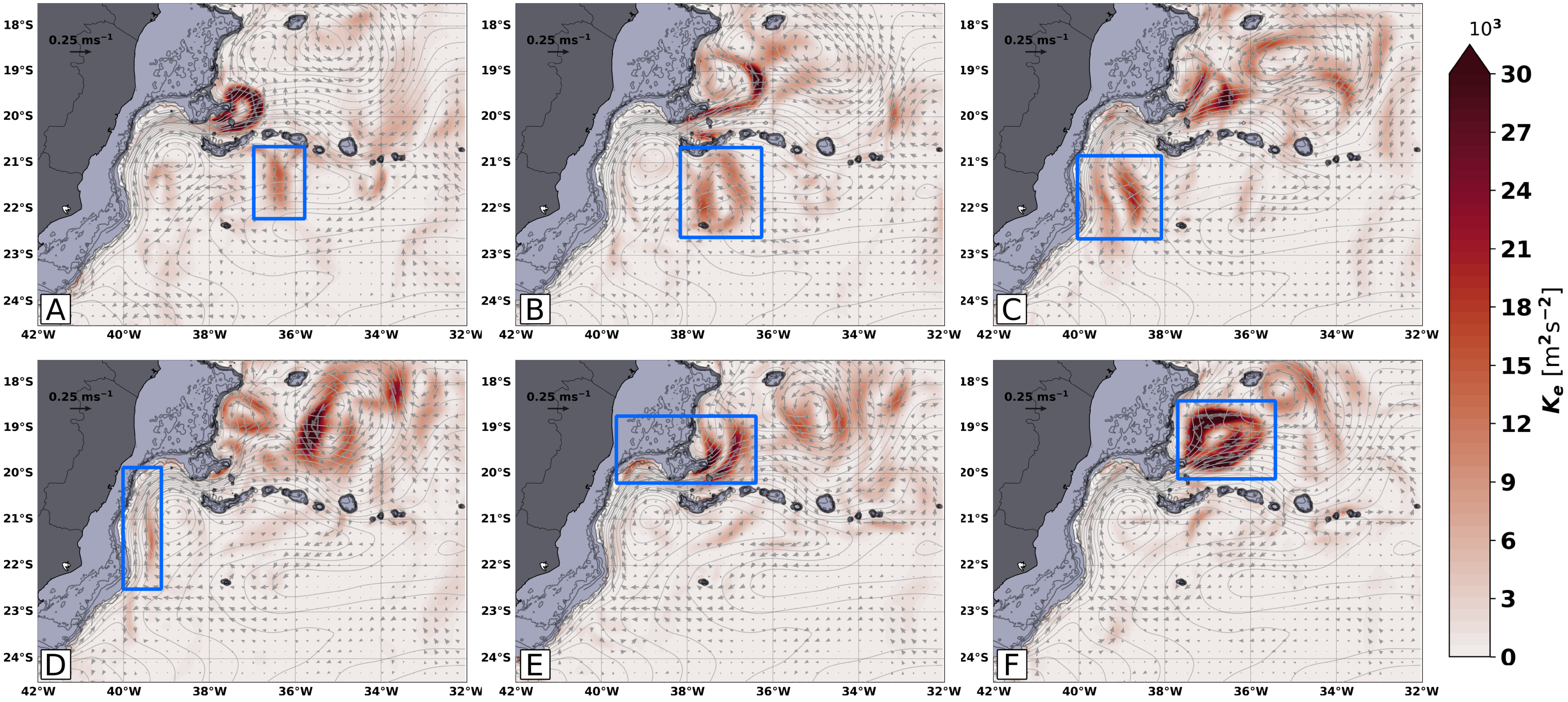

Figure 2.11: Tracking of a wave-like perturbation (highlighted by the blue rectangle) entering Tubarão Bight and being carried north of the VTR by the IWBC. From the detection of the perturbation at longitude 36° W at 5 Jan 2002, the panels represent the evolution of the signal at day (A):1, (B):25, (C):56, (D):71, (E):81, and (F):92. The red colors are the K_e calculated from ROMS outputs; arrows indicate ROMS daily total velocity; solid gray lines represent the steady-state streamfunction.

We select 29 events from the series and estimate a mean wavelength of $344 \pm 89\,\mathrm{km}$, a mean period of 36 ± 7 days, and a mean phase speed $c = 0.06 \pm 0.01\,\mathrm{m\,s^{-1}}$ ($5.18\,\mathrm{km\,day^{-1}}$). The mean eddy speed is $|\mathbf{u}| = 0.07 \pm 0.03\,\mathrm{m\,s^{-1}}$ ($6.05\,\mathrm{km\,day^{-1}}$), so $|\mathbf{u}|/c \approx 1.14 \pm 0.57$, suggesting nonlinearity (Chelton et al., 2011). We show that these nonlinear westward-propagating eddies have Eulerian phase speeds consistent with the nondispersive linear Rossby-wave dispersion relation (fig. 2.12-A), as previously remarked by Morten et al. (2017). A standard modal analysis of these subsurface-intensified eddies indicates that the first baroclinic mode accounts for most of the variance, about 40%. And a synthesis with the gravest four modes accounts for 80% of the eddy vertical structure (fig. 2.12-B, C and D).

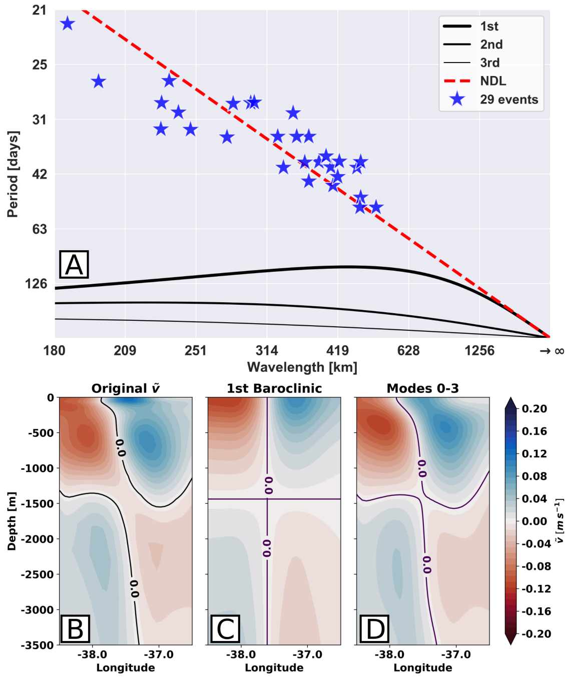

Figure 2.12: (A): Rossby wave dispersion relation diagram for Tubarão Bight. The thick black line represents the linear first mode Rossby wave dispersion relation (deformation radius $\cong 70\,\mathrm{km}$). The second and third modes are plotted with thinner lines (deformation radius $\cong 35$ and $20\,\mathrm{km}$, respectively). The dashed red line represents the nondispersive line (NDL) for the first mode waves. The blue stars indicate the characteristics based on the Eulerian phase-speeds of the signals tracked. (B) Vertical $\tilde{v}$ structure of the signal on 30 Jan 2002. (C) Reconstruction of the signal using the first baroclinic mode. (D) Reconstruction of the signal using the barotropic and the first three baroclinic modes.

Tubarão Bight energetics

We now turn to the energy budget in Tubarão Bight, defined as the $\sim$19–23° S domain west of $\sim$36° W. For this region, we calculate the energy conversion terms and the energy fluxes in table 2.2. Figure 2.13-A, B and C show in colors the total eddy kinetic energy generation, $-\overline{SP}+\overline{\tilde{w}\tilde{b}}$, and arrows indicate the kinetic energy flux $\mathbf{F}_e$ and pressure-work flux $\mathbf{P}_w$ through the boundaries. Kinetic energy enters the domain through pressure work and advection by the mean flow, mostly across the southeastern corner. This eddy energy is advected northward through the VTR by the IWBC mean flow. North of the VTR, copious eddy kinetic energy is generated by barotropic conversion $-\langle HSP\rangle$. The enhanced eddy kinetic energy is advected northeastward out of the domain or propagates southward through pressure work.

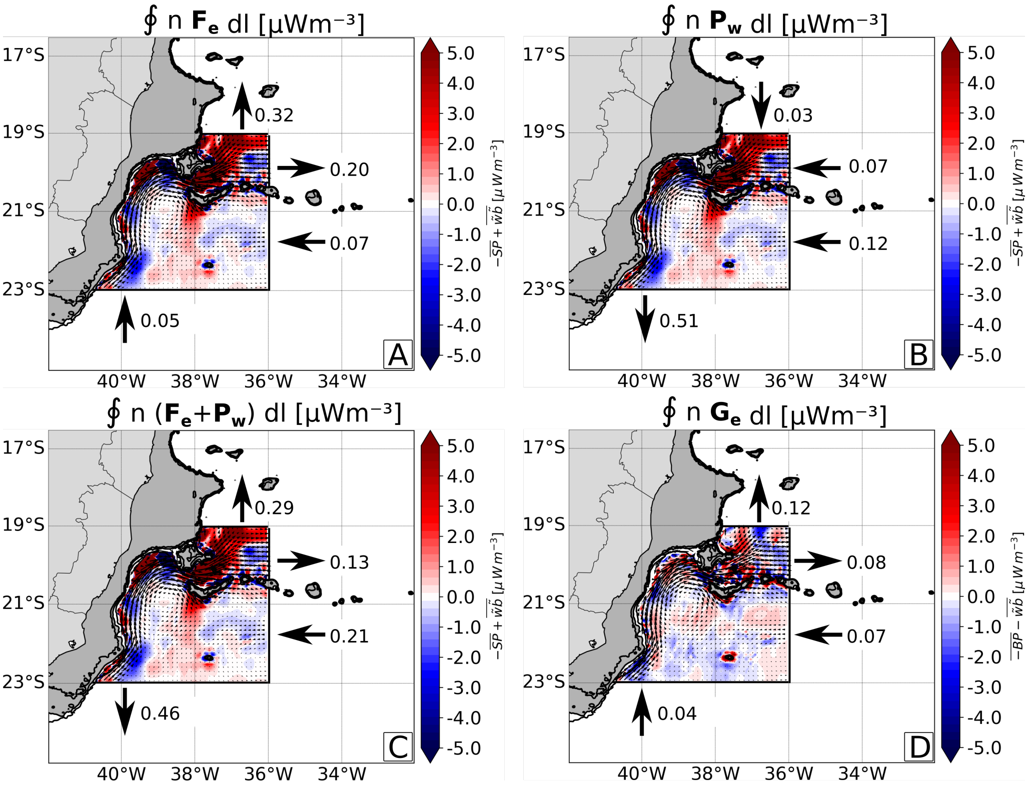

Figure 2.13: Divergence at the Tubarão Bight borders of (A) K_e advection, (B) pressure work, (C) K_e advection plus pressure work, and (D) potential energy advection. Arrows indicate flow through the borders, indicating a source (sink) of energy when the arrow points to the inside (outside) of the region.

The dominant eddy kinetic energy budget within Tubarão Bight is

$$\langle HSP \rangle \approx \oint \mathbf{n} \cdot \mathbf{F}_e \, dl + \oint \mathbf{n} \cdot \mathbf{P}_w \, dl \, . \tag{2.17}$$

In other words, the eddy kinetic energy flux (mostly through advection by the mean flow) and the pressure work balance horizontal shear production within Tubarão Bight (see detailed energy budget in fig. 2.14). Perturbations enter the domain through the southeastern boundary through $\mathbf{P}_w$ and $\mathbf{F}_e$, are advected through the VTR by the IWBC, and then grow explosively downstream of the ridge through horizontal shear production.

For completeness, we also present the eddy potential energy budget in figures 2.13-D and 2.15. The dominant budget is

$$\langle VBP \rangle + \langle \overline{\tilde{w}\tilde{b}} \rangle \approx \oint \mathbf{n} \cdot \mathbf{G}_e \, dl \, . \tag{2.18}$$

Eddy potential energy is advected into the domain mostly by the mean flow across the southern and southeastern boundaries. Within Tubarão Bight, eddy potential energy is generated by vertical buoyancy production, particularly near seamounts, and via conversions from the eddy kinetic energy reservoir through buoyancy flux $-\langle \overline{\tilde{w}\tilde{b}} \rangle$. The eddy potential energy generated within Tubarão Bight is advected out of the region by the mean flow across the northern and northeastern boundaries.

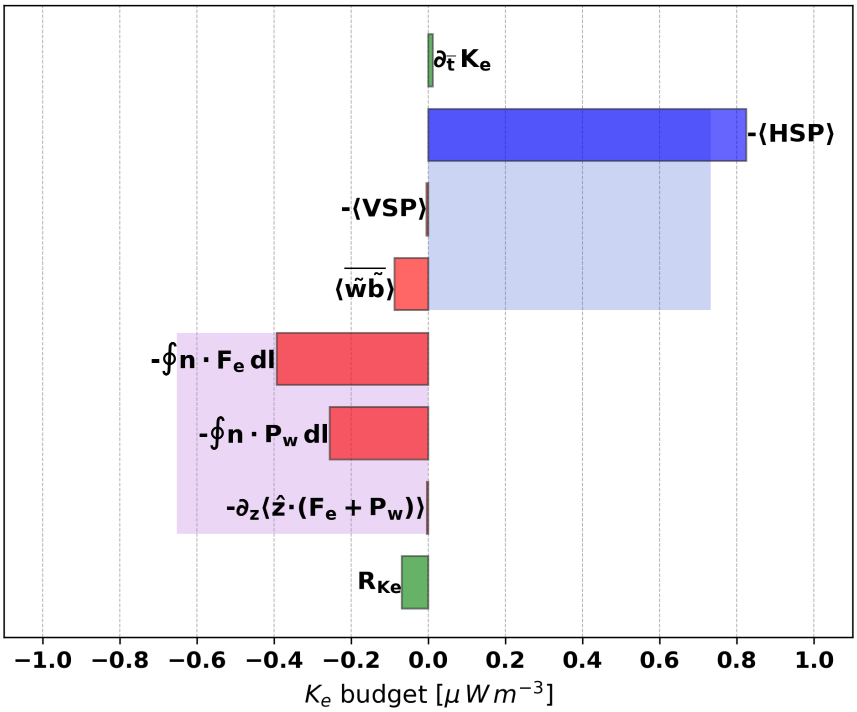

Figure 2.14: The kinetic energy budget for Tubarão Bight according to Equation (2.15). Blue/positive (red/negative) bars represent a source (sink) of energy. Green bars indicate the residuals of the time-varying K_e. Residuals are ∼9% to close 99% of the budget.

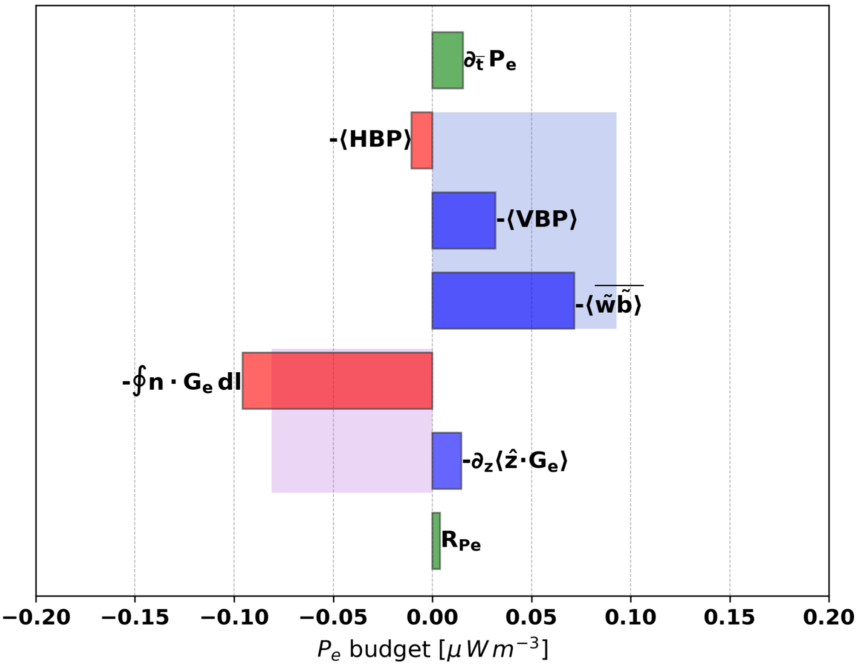

Figure 2.15: The potential energy budget for Tubarão Bight according to Equation (2.16). Blue/positive (red/negative) bars represent a source (sink) of energy. Green bars indicate the residuals of the time-varying P_e. Residuals are ∼3% to close 87% of the budget.

In summary, the energetics suggest that the westward-propagating features, such as the one in figure 2.11, interact with the mean flow as they are advected by the IWBC, experiencing explosive growth downstream of the VTR. The mechanism of interaction is barotropic conversions, and the process appears to be constrained by topography. A simple representation of the Tubarão Bight energy budget is shown in figure 2.16.

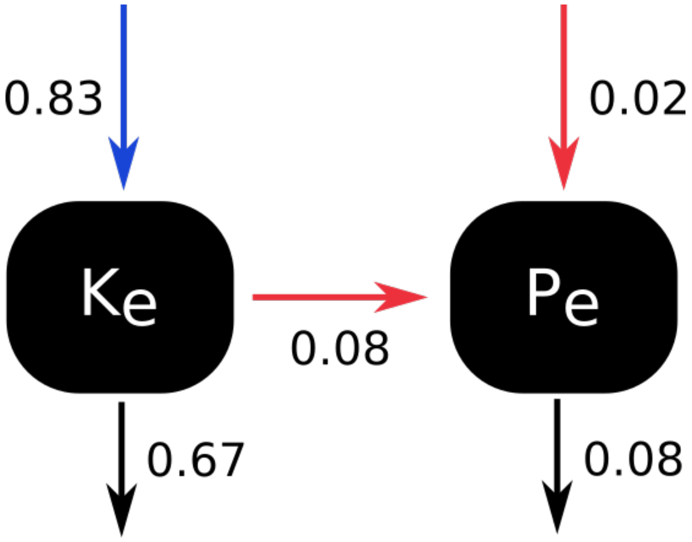

Figure 2.16: The TB energy budget represented by the Lorenz energy diagram. Blue lines indicate the barotropic instability pathway, red lines indicate the baroclinic instability pathway, and black lines represent the redistribution of energy through the borders of the domain. Values are expressed in $\mu W m^{-3}$.

5 Final remarks

New direct velocity measurements of the Intermediate Western Boundary Current (IWBC) show (and detail) a circulation pattern consistent with the existing literature, namely: (i) off Cape São Tomé, the IWBC flows northward along the continental slope, underneath the southward-flowing Brazil Current; (ii) at Tubarão Bight, topography steers the IWBC, generating a cyclonic recirculation that intensifies the flow along the continental slope south of the bight; and (iii) the remaining IWBC flow exits the bight through the Vitória-Trindade Ridge main channel. Argo float trajectories reveal a larger, zonally elongated IWBC recirculation around the VTR that extends to $\sim$35° W. A regional simulation with ROMS shows good skill in simulating these observational patterns, including the IWBC recirculation cells.

Analysis of an intermediate-layer QG model shows that the time-mean ROMS circulation is a good proxy for the IWBC steady state ($>$90%), with the linear inversion relation $\bar{Q}$ = -3.84$\times 10^{-9}\,\bar{\psi}$. And geostrophic scatterplots suggest that the IWBC is unstable along its path ($d\bar{\psi}/d\bar{Q} < 0$).

Despite a steadiness indicated by the QG analysis, ROMS eddy-mean energy exchanges are important throughout the model domain. A detailed energy analysis around Tubarão Bight shows that steadiness is broken by nonlinear eddies that enter the domain through the eastern boundary. Despite their nonlinearity, these eddies have phase speeds consistent with nondispersive linear Rossby-wave theory. The perturbations interact with the IWBC mean flow via barotropic conversions. As they are advected downstream, the eddies grow by feeding off the mean flow through standard Reynolds-stress horizontal shear production, with topography seemly playing an important role in this growth process.

The model results highlight the complexity of the eddy-mean flow interactions off east Brazil, with both remote forcing and downstream eddy growth playing critical roles. Process-oriented observational studies are needed to test these model predictions and further characterize local and nonlocal eddies in this region and their effects on the IWBC and the Meridional Overturning Circulation.

Appendix A: Calculation of g′

In the model schematic presented in section 3, layer thickness $h = h(x, y)$ is a function of space only, and density is constant for each layer. We evaluate the pressure in the upper layer $P_1 = \rho_1 g(h_1 + h + h_2 - z)$ and at $z = 0$ in the bottom layer $P_2(x, y, 0) = \rho_1 g h_1 + \rho g h + \rho_2 g h_2$. Setting the horizontal gradient of both to zero gives

$$\nabla h_2 + \nabla h + \nabla h_1 = 0\,,$$

$$\rho_2 \nabla h_2 + \rho \nabla h + \rho_1 \nabla h_1 = 0\,, \tag{2.19}$$

which can be solved to relate the height gradients above and below to ∇h

$$\nabla h_2 = -\left(\frac{\rho_1 - \rho}{\rho_2 - \rho_1}\right) \nabla h \quad \text{and} \quad \nabla \mathrm{h}_1 = \left(\frac{\rho - \rho_2}{\rho_2 - \rho_1}\right) \nabla \mathrm{h}\,. \tag{2.20}$$

We can find the pressure P in the middle layer by integrating from the bottom, with P_2 the (constant) pressure at a horizontal surface $z = 0$ deep within the layer

$$P \;=\; P_2 - \rho_2 g h_2 - \rho g(z - h_2)\,. \tag{2.21}$$

Taking the horizontal gradient of (2.21) and replacing ∇h_2 from (A2) yields

$$\frac{\nabla P}{\rho} = g\left(\frac{\rho - \rho_1}{\rho_2 - \rho_1}\right)\left(\frac{\rho_2 - \rho}{\rho}\right)\nabla h = g\prime \nabla h\,, \tag{2.22}$$

so that g′ is given by

$$g\prime = g\left(\frac{\rho - \rho_1}{\rho_2 - \rho_1}\right)\left(\frac{\rho_2 - \rho}{\rho}\right)\,. \tag{2.23}$$

Appendix B: Estimation of Scatter Cloud Relative Area

In $\psi - Q$ space, the scatter of points about the line correlating the variables represents the amount of departure from free-mode in a flow. From equation

$$I \overset{\text{def}}{=} \frac{A}{\Delta\Psi\Delta Q} = \frac{\text{area enclosed by the cloud of points}}{\text{area of the rectangle}}\,, \tag{2.24}$$

the area A was estimated from a polygon drawn graphically connecting values of Q_{min} and Q_{max} in a given $\delta\Psi$, as in figure B1.

In a high-resolution grid filling the rectangle $\Delta\Psi\Delta Q$, the area A enclosed by the cloud of points can be interpreted as the number of points inside the hatched polygon. In the illustrative example,

$$I = \frac{210000}{1000 \times 1000} = 0.21, \tag{2.25}$$

thus implying 79% correlation within this fictional dataset.

Read et al. (1986) discuss the caveats of this index, which depends on the orientation of the polygon, as well as on its shape in $\psi - Q$ space. The authors also propose an alternative metric based on the perpendicular width of the scatter cloud relative to its length: given a scatter cloud angle $\phi \leq \pi/2$, the width-to-length ratio is thus $\tan(\phi)/2$ and a measure of the departure from free-mode. For the IWBC, this metric yields ~ 0.15, against 0.08 of the **I** index.

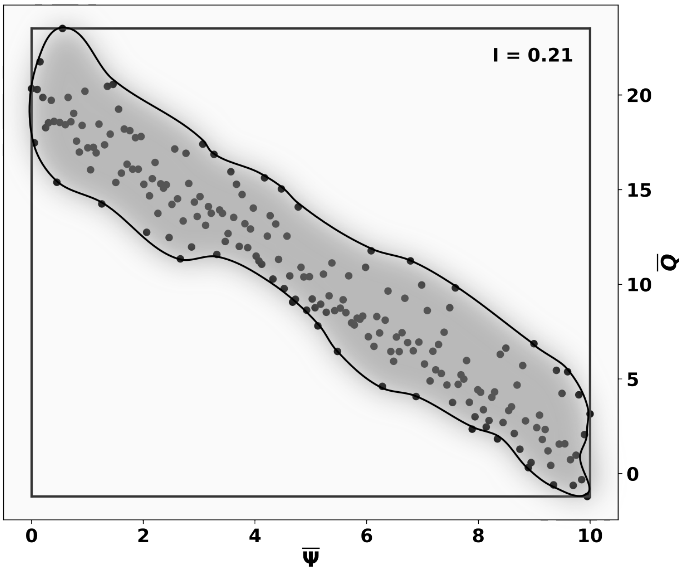

Figure B1: Representation of a random cloud of points in $\Psi - Q$ space and the area around it, occupying 21% of the maximum area delimited by the $\Delta\Psi\Delta Q$ rectangle.

Acknowledgements

We thank Frank O. Smith for copy-editing and proofreading this manuscript. This study was financed in part by Coordenação de Aperfeiçoamento de Pessoal de Nível Superior — CAPES, Brazil — Finance Code 001 and by Projeto REMARSUL (Processo CAPES 88882.158621/2014-01), Projeto VT-Dyn (Processo FAPESP 2015/21729-4) and Projeto SUBMESO (Processo CNPq 442926/2015-4). Rocha was supported by a WHOI Postdoctoral Scholarship.

CHAPTER 3.

IS THE VITÓRIA EDDY TRIGGERED BY THE INTERMEDIATE WESTERN BOUNDARY CURRENT RECIRCULATION WITHIN TUBARÃO BIGHT?

Manuscript submitted in May 2020, to the *Ocean Dynamics Journal*. This manuscript is co-authored by Cesar B. Rocha, Ilson C. A. Silveira, Iury T. Simoes-Sousa and Glenn R. Flierl

Abstract

South of the Vitória-Trindade Ridge, a seamount chain off East Brazil, the Brazil Current (BC) meanders cyclonically within Tubarão Bight, occasionally forming the Vitória Eddy. It was recently found that the Intermediate Western Boundary Current (IWBC), which flows equatorward below the BC, cyclonically recirculate within Tubarão Bight. We present an analysis of AVISO observations that suggest that the Vitória Eddy formation is conditioned by the strength of the BC upstream of Tubarão Bight. A weak BC is prone to local meandering and eddy formation in the bight, while a strong BC suppresses eddy formation in the bight but triggers downstream meander growth. To study the effects of the IWBC recirculation on the BC meandering and the Vitória Eddy formation, we formulate a simple two-layer quasi-geostrophic model. In the model, the BC is represented by a meridional jet in the upper layer and the IWBC recirculation is a steady eddy in the lower layer. The lower-layer eddy effectively acts as a topographic bump, affecting the upper-layer jet via the stretching term ψ_2/R_d^2, where ψ_2 is the lower-layer streamfunction and R_d is the baroclinic deformation radius. Based on the AVISO sea-surface height data and previous observational studies, we define a stationary eddy and reference jet. We conduct a number of initial-value problem experiments varying the upper-layer jet speed. A weak upper-layer jet slowly meanders and develops a cyclone above the lower-layer eddy. As we increase the jet velocity, the meandering is faster and the cyclone is larger. But a too-strong jet has an opposite effect: the potential vorticity anomalies induced by the lower-layer eddy are quickly swept away, leading to explosive downstream meander

growth; no cyclone is formed above the lower-layer eddy. In all cases, the initial meandering trigger is a linear process (the steering of the upper-layer jet by the lower-layer eddy). But even when the upper-layer jet is weak, nonlinearity quickly becomes important, dominating the dynamics after 10 days of simulation. The downstream meander growth is fully nonlinear.

1 Introduction

The Brazil Current (BC) is the subtropical western boundary current of the South Atlantic. The BC is formed at about 15 °S, developing quasi-stationary, recurrent anticyclones as it negotiates the Brazilian eastern continental margin (Soutelino et al., 2011). At 20 °S, the BC encounters the Vitória-Trindade Ridge, a zonal seamount chain.

The Abrolhos Bank and seamounts act as physical obstacles to the BC as it crosses the Vitória-Trindade Ridge poleward (see figure 3.1). South of the Vitória-Trindade Ridge, the BC meanders within Tubarão Bight, sometimes forming the Vitória Eddy (cf. Schmid et al., 1995). In the first description of the Vitória Eddy, Schmid et al. (1995) attributed its formation to the BC meandering, which was linked to strong coastal upwelling events. This topographically constrained eddy is quasi-stationary, with rare equatorward-translation events, first described by Campos (2006) using a numerical simulation. Arruda et al. (2013) attributed those Vitória Eddy translation events to dipole interactions with the Abrolhos Eddy (cf. Soutelino et al., 2011).

Flowing equatorward at intermediate layers, the Intermediate Western Boundary Current (IWBC; cf. Boebel et al., 1999), originating at 28 °S, reaches Tubarão Bight, forming a topographically forced cyclonic recirculation (Costa et al., 2017). This recirculation—hereafter the IWBC Eddy—is quasi-steady and constrained to Tubarão Bight. In other words, the recirculation barely changes its speed or its position in time compared to the time scale of the BC variability (see Costa et al., 2017; Napolitano et al., 2019, for details).

Interactions between the BC and the IWBC have been studied by Silveira et al. (2008), Mano et al. (2009) and Rocha et al. (2014). Silveira et al. (2008) showed that the meandering of the BC-IWBC system is caused by baroclinic instability. Using a numerical model, Mano et al. (2009) estimated baroclinic conversion during a cyclonic meandering event, showing that the perturbation starts at the IWBC and transfers energy from intermediate to upper layers as it grows. Based on the analysis of three moorings along the BC axis, Rocha et al. (2014) showed that the mean-to-eddy baroclinic conversion peaks around the BC-IWBC interface. The effects of a topographically-forced, slower-varying deep flow driving changes in the upper layers have also been addressed by Hurlburt and Hogan (2008), for the Gulf Stream separation region, and by Hurlburt et al. (2008), for the Japan/East Sea.

Given the formation site of the intermittent, quasi-standing Vitória Eddy located above the quasi-permanent, stationary IWBC Eddy, we ask: Is the stretching produced by the IWBC recirculation strong enough to deflect the BC in the upper layers? In other words, how the IWBC Eddy affects the formation of the Vitória Eddy?

As an initial step toward answering this question, we first look at the BC in the upper layer. We examine 26 years of altimetry data to identify (i) the path and velocity of the BC within Tubarão Bight; and (ii) the conditions sustaining or hindering the Vitória Eddy formation.

2 Altimeter observations within Tubarão Bight

Sea surface height (SSH) contours can be used as a proxy for the geostrophic signature of the western boundary currents (Vallis, 2017). To determine the main axis of the Kuroshio, Qiu and Chen (2005) used the 170-cm contour based on the maximum SSH meridional gradient in the region, whereas Andres (2016), using the same approach, selected the 25-cm contour for the Gulf Stream.

Here, we use the SSH contours from the AVISO dataset, distributed by the Copernicus Marine Environment Monitoring Service (CMEMS), at L4-level processing with $^1/_4{}^\circ$ of horizontal resolution. (The data are available at `www.aviso.altimetry.fr/duacs`.)

BC axis position and velocity

In our study region, we choose the 59-cm contour as a proxy for the BC axis streamline. This contour represents the approximate location of the maximum SSH gradient throughout the region. Figure 3.1 shows the BC paths, as indicated by the 59-cm SSH contours, obtained from 26 years of AVISO data. The blue lines depict the paths obtained from monthly-averaged SSH fields, and the red line is based on the 26-year average SSH. (South of 21 °S, we only considered contours in regions shallower than the 3500-m isobath.) In the upper layer, nearly every BC streamline crosses Tubarão Bight through the center of the intermediate-layer IWBC Eddy—the dashed black line in figure 3.1, which is based on Costa et al. (2017) and Napolitano et al. (2019). While monthly means in figure 3.1 show significant spreading of the BC paths north of 22 °S, there is much less variability south of 22 °S, where the BC organizes itself.

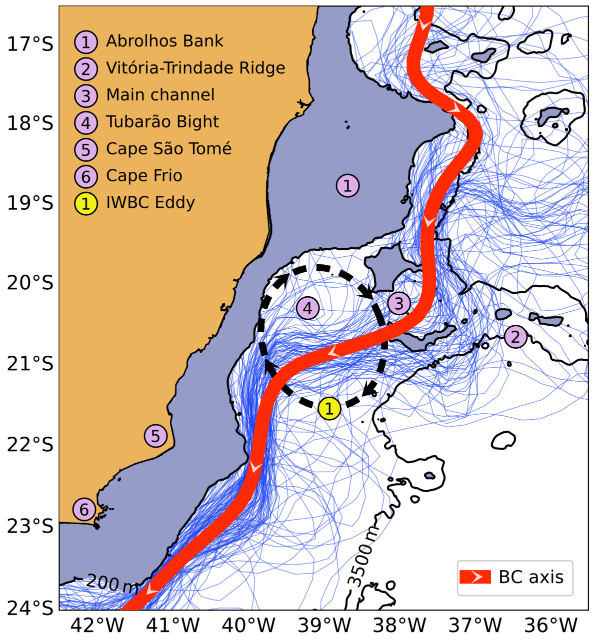

Figure 3.1: Southeastern Brazil main topographic features and the Brazil Current axis. The current axis is represented by the 59-cm SSH contours (from 1993 to 2018) over a schematic IWBC eddy. Blue lines represent the 59-cm contour on monthly SSH means; the red line represents the 59-cm contour in the mean SSH for the whole series. The IWBC eddy is represented by the black dashed ellipse.

From daily altimeter-derived geostrophic velocity we calculated the maximum velocity within Tubarão Bight. Figure 3.2-A displays a timeseries of the mean along-axis BC velocity above the IWBC Eddy. The mean BC speed within Tubarão Bight is $0.2\,\mathrm{m\,s^{-1}}$, ranging from $\sim$0.1 to $0.5\,\mathrm{m\,s^{-1}}$. Panel B shows the probability density function (PDF) of the BC speed, with frequent weak values close to half the mean, and episodic high velocities more than twice the mean. Previous mooring data in the region depicted mean velocities in the same ballpark as our estimates for the BC: in the Vitória-Trindade Ridge's main channel, Müller et al. (1998) reported $0.09\,\mathrm{m\,s^{-1}}$; within Tubarão Bight, Costa et al. (2017) reported $0.09\pm0.02\,\mathrm{m\,s^{-1}}$; downstream the bight, Rocha et al. (2014) reported $0.31\pm0.12\,\mathrm{m\,s^{-1}}$ at 22.8 °S. The maximum daily-velocity estimates in figure 3.2 is about $0.5\,\mathrm{m\,s^{-1}}$, close to shipboard-ADCP velocities in the Vitória-Trindade Ridge reported by Napolitano et al. (2019). Schmid et al. (1995) also found similar values within the innermost part of Tubarão Bight, using hydrographic sections and surface drifters. Off Cape Frio (23 °S), Silveira et al. (2004, 2008) analyzed data from synoptic velocity profilers and a mooring, and found maximum velocities of 0.5 $\mathrm{m\,s^{-1}}$ and 0.41 $\mathrm{m\,s^{-1}}$, respectively.

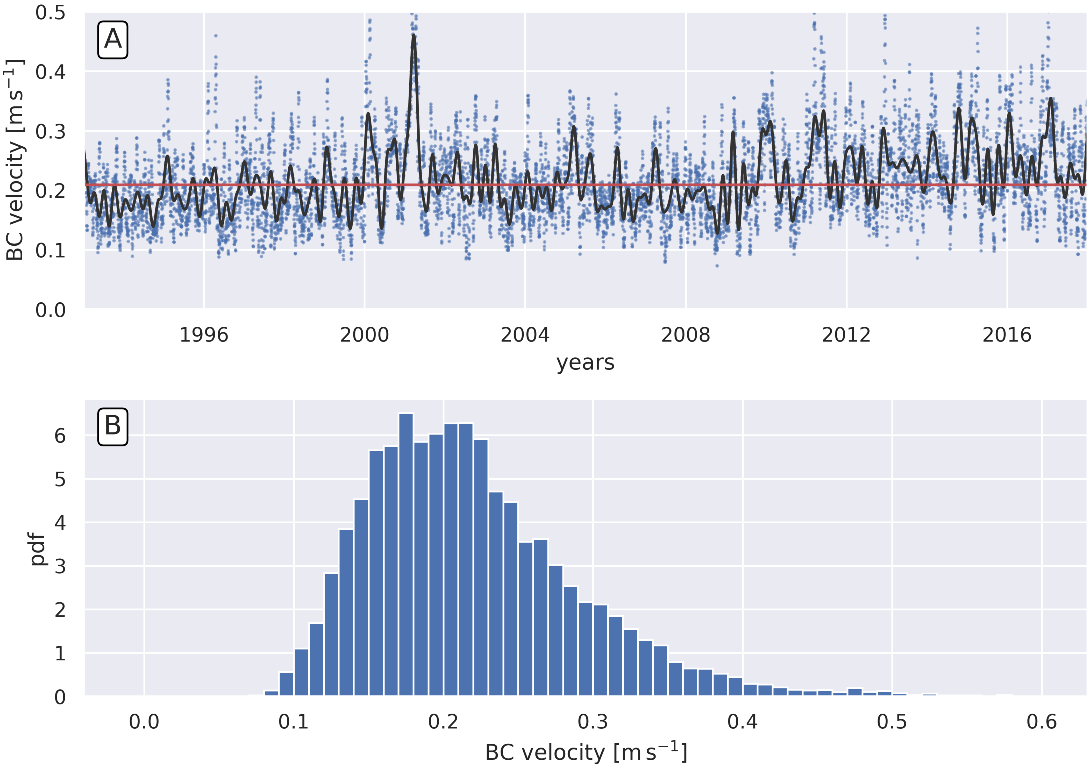

Figure 3.2: (A) Timeseries and (B) pdf for the Brazil Current geostrophic velocity within Tubarão Bight from AVISO altimetry. Blue dots represent daily velocity values; the black line represents the low-pass filtered velocity (60 days); the red solid line represents the mean velocity during the whole series.

Vitória Eddy formation and suppression events

We define three BC regimes according to figure 3.2: the WEAK BC, with a velocity of 0.1 $\mathrm{m\,s^{-1}}$; the MEAN BC, with 0.2 $\mathrm{m\,s^{-1}}$; and the STRONG BC, with 0.5 $\mathrm{m\,s^{-1}}$. Following this classification, we examined the AVISO timeseries and selected, for each regime, periods of 30 days in which the BC crossed Tubarão Bight above the center of the IWBC Eddy, assuming that the eddy is stationary and thus remains locked within the bight. (Since we use gridded geostrophic velocities, this classification may underestimate the BC strength during the events described next.) Analyzing AVISO's daily SSH, we find that both local and remote mesoscale eddies are responsible for the variability in Tubarão Bight (e.g., Mill et al., 2015). To isolate the local effects, we selected periods where remotely-generated perturbations rarely entered the region, i.e. periods that the Vitória Eddy formation resulted solely from the BC meandering. Figure 3.3 shows snapshots of these events for each of the BC regimes defined above.

On 21 May 1999, a WEAK BC enters Tubarão Bight through the Vitória-Trindade Ridge's main channel, flowing poleward along the Abrolhos Bank, and partially meandering in a cyclonic loop centered at ~21.5 °S–37 °W (figure 3.3-A). Although fully developed on 31 May, an asymmetric Vitória Eddy with a stronger oceanic lobe is shown in figure 3.3-B; north of the Vitória-Trindade Ridge, the BC is not well organized. Figure 3.3-C shows the stationary Vitória Eddy within the IWBC Eddy domain, and mesoscale activity in the shelf break around Cape Frio (e.g., Silveira et al., 2008). North of the Vitória-Trindade Ridge, the BC reorganizes starting on 16 June (see figure 3.3-C).

On 22 February 2015 a MEAN BC crosses the Vitória-Trindade Ridge mainly through its innermost channel (see figure 3.3-D). The BC meanders cyclonically, resulting in the Vitória Eddy. An anticyclone organizes itself north of the Vitória-Trindade Ridge at ~19.5 °S, and a meander grows downstream of Cape São Tomé. By 9 March the Vitória Eddy is well developed (figure 3.3-E), and it remains coherent at least until 24 March (figure 3.3-F); on 24 March a cyclone is also formed from the downstream meandering (the eddies's names are referenced in figure 3.3).

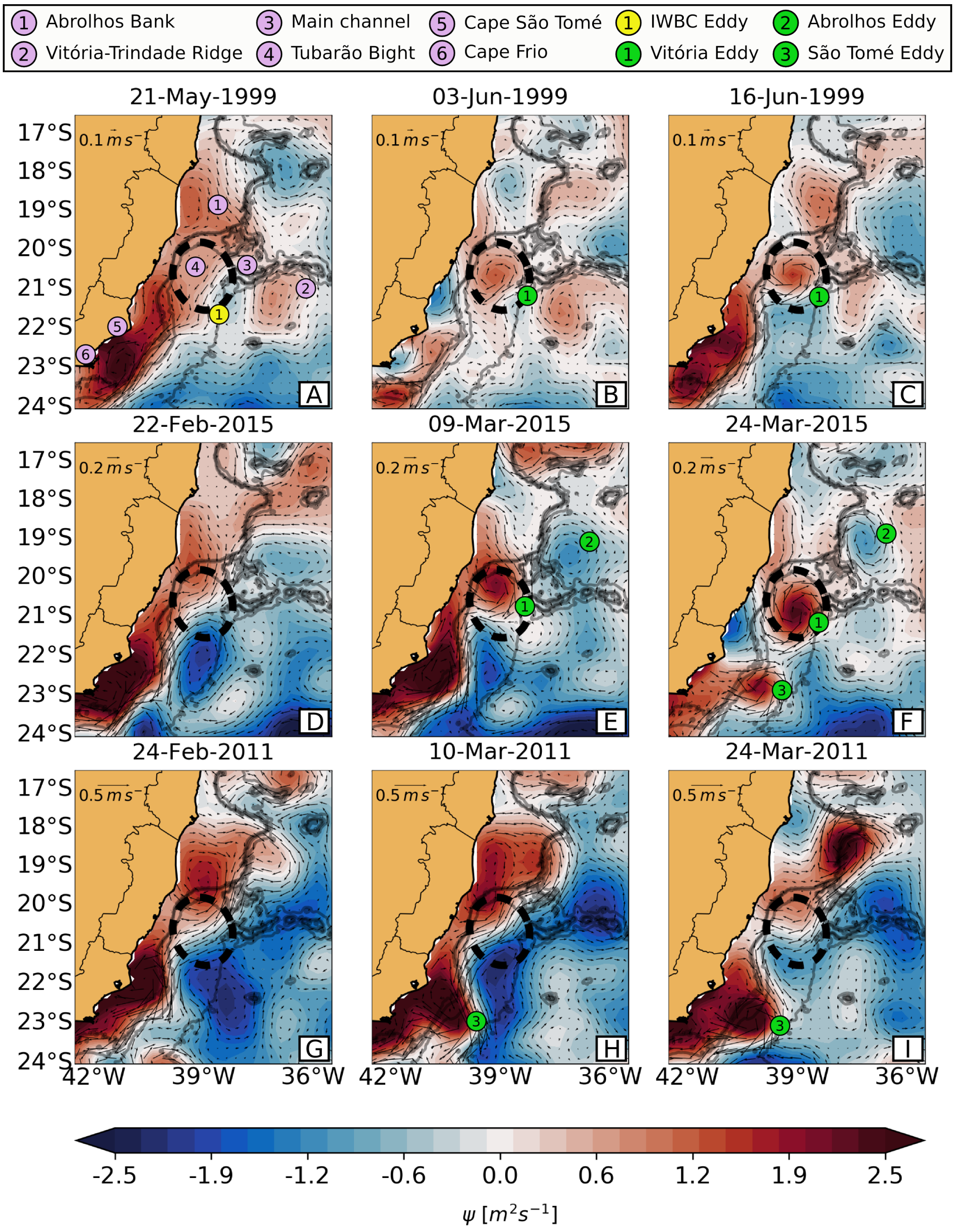

Figure 3.3: Snapshots for ∼30 days of AVISO SSH corresponding to (A–C) a WEAK BC with ∼0.1 m s^{-1} on 21 May 1999; (D–F) a MEAN BC with ∼0.2 m s^{-1} on 22 Feb 2015; and (G–I) a STRONG BC with ∼0.5 m s^{-1} on 24 Feb 2011. Velocities are computed within Tubarão Bight. Purple keys represent the topographic features, the dashed ellipse (yellow key) marks the position of the permanent IWBC Eddy, and green keys mark the mesoscale eddies.

Flowing poleward through the main channel of the Vitória-Trindade Ridge, on 24 February 2011 a STRONG BC crosses straight through Tubarão Bight, reattaching to the slope at 21 °S (see figure 3.3-G). This strong jet continues along the shelf break through Cape São Tomé, where a cyclonic meander grows (figure 3.3-H). In Tubarão Bight, the

BC appears to suppress the formation of the Vitória Eddy. Downstream, at the capes, figure 3.3-I shows a fully-developed cyclone.

In addition to the cyclones highlighted above, anticyclonic features in figures 3.3-E and F (the Abrolhos Eddy) appear associated with the BC. Before the formation of the Abrolhos Eddy in figure 3.3-D, a large anticyclone appears east of the BC, between ∼21–23 °S. As the Vitória Eddy grows, it displaces this anticyclone poleward, until it is no longer seen in figure 3.3-F. In figures 3.3-G and H, we observe the same structure, but without the formation of the Vitória Eddy. The anticyclone endures until the end of the analyzed period, although it weakens with time.

In the different AVISO sequences analyzed, the Vitória Eddy lasts for less than 2 months. The eddy is either absorbed by the BC, or decays close to the topography of Tubarão Bight and the Vitória-Trindade Ridge. As mentioned earlier, rare equatorward-translation events of the Vitória Eddy have also been described in the literature (e.g. Campos, 2006; Arruda et al., 2013).

Motivated by these AVISO observations, from which we obtained different BC conditions in which the Vitória Eddy is formed or suppressed, we hypothesize (i) that the IWBC Eddy influences the formation of the Vitória Eddy and (ii) that the BC strength affects this process. To test these hypotheses, in section 3 we formulate a quasi-geostrophic model to simulate the interaction of the IWBC Eddy with the BC in different regimes. This simple model isolates the effects of the stretching vorticity, which couples the IWBC Eddy with the BC jet. We study the eddy generation in the upper layer by fixing the lower-layer eddy amplitude and varying the upper-layer jet strength.

3 The quasi-geostrophic model

Model equations

In our model, the evolution of the upper-layer potential vorticity (PV) in the $f-$plane is given by

$$q_t + J\left(\psi, q\right) = \nu \nabla^4 \psi \,, \tag{3.1}$$

where the PV is

$$q = \underbrace{\nabla^2 \psi}_{\overset{\text{def}}{=}\zeta} + \frac{\psi_2 - \psi}{R_d^2} \,. \tag{3.2}$$

Above, ψ is the upper-layer streamfunction, ψ_2 is a steady streamfunction that represents the lower-layer flow, and R_d is the baroclinic deformation radius. The Jacobian in (3.1) is $J(\psi, q) = \psi_x q_y - \psi_y q_x$, and the Laplacian operator in (3.2) is $\nabla^2 = \partial_x^2 + \partial_y^2$. To ensure numerical stability, we included the dissipative term on the right of (3.1), where $\nabla^4 = \nabla^2 \nabla^2$ and ν is an effective viscosity.

In this simple model, the steady lower-layer flow is coupled with the upper-layer dynamics via the stretching term—the second term on the right of (3.2). To simulate the effects of the topographically constrained IWBC recirculation on the BC eddy formation above, we choose ψ_2 as a radially symmetric eddy (details below). We emphasize that $\psi_2 = \psi_2(x, y)$ and the dynamics in the lower layer is completely ignored. Thus (3.1)-(3.2) is effectively a barotropic quasi-geostrophic model with a topographic anomaly given by $h_b/H = \psi_2 / f_0 R_d^2$, where f_0 is the Coriolis parameter and H is the layer depth.

Assuming a steady state for the upper layer with $q_t = 0$, a linearized and inviscid form of (3.1) yields parallel streamfunction in the upper and lower layers,

$$J(\psi, \psi_2) = 0 \,, \tag{3.3}$$

which implies $\nabla\psi \times \nabla\psi_2 = 0$, i.e. that the upper layer flow adjusts to the steady lower layer flow, or the bottom topography.

We solve (3.1)-(3.2) numerically using Dedalus (Burns et al., 2019), a framework for solving partial differential equations with standard spectral methods. We use a re-entrant channel configuration, with a Fourier basis for the along-channel y-axis, and a Chebyshev basis for the cross-channel x-axis. We prescribe the initial streamfunction ψ, calculate q in (3.2) at $t = 0$, and then iterate the time-marching of q with (3.1) and the inversion for ψ with (3.2). Time-stepping is performed with a fourth-order implicit-explicit Runge–Kutta scheme. We enforce no-normal flow at the channel walls:

$$\psi_y = 0 \quad \text{for} \quad n \neq 0\,, \tag{3.4}$$

where n is the Fourier component. As with all quasi-geostrophic channel models, the zeroth-Fourier component requires Phillips's boundary conditions (Phillips, 1954; McWilliams, 1977) given by

$$\psi_{yt} - \nu\nabla^2\psi_y = 0 \quad \text{for} \quad n = 0\,. \tag{3.5}$$

At the channel walls, we also enforce

$$\nabla^4\psi = 0\,, \tag{3.6}$$

implying that there is no vorticity diffusion through the boundaries.

Model setup and initial conditions

We run a set of initial-value experiments initialized with a jet in the upper layer that represents the Brazil Current basic state. The steady lower-layer flow is a radially symmetric eddy whose velocity is given by

$$V(r) = v_e \tanh\left(\frac{\pi r}{5\,r_e}\right) B(r)\,, \tag{3.7}$$

where $r = \sqrt{(x-x_c)^2 + (y-y_c)^2}$ is the radial distance from the center of the eddy (x_c, y_c), and v_e and r_e are the IWBC Eddy maximum velocity and radius, respectively, obtained from previous studies (see below). Also in (3.7), $B(r)$ is a bell function,

$$B(r) = \left[\frac{2}{5} + \left(\frac{r}{r_e}\right)^{15}\right]^{-1} . \tag{3.8}$$

The asymmetric eddy shape in (3.7) is inspired by observations that depicted an IWBC Eddy with a faster decay toward the continental slope (Costa et al., 2017; Napolitano et al., 2019). Based on Napolitano et al.'s Argo climatological fields, we choose $r_e = 90\,\text{km}$ and $v_e = 0.2\,\text{m}\,\text{s}^{-1}$. These parameters are also consistent with values reported by Costa et al. (2017).

From $V(r)$ we compute the Cartesian x-y velocity components

$$(u, v) = V\left(\cos\theta\,, \sin\theta\right), \tag{3.9}$$

where $\theta = \tan^{-1}[(y-y_c)/(x-x_c)]$. The streamfunction ψ_2 is calculated numerically given u and v, using an iterative method in Dedalus.

The initial upper-layer flow is an along-channel Gaussian jet centered at x_c. The initial streamfunction is

$$\psi(t=0) = -v_0\, L\ \mathrm{erf}\left(\frac{x-x_c}{L}\right), \tag{3.10}$$

where erf is the error function,

$$\mathrm{erf}(\chi) \overset{\text{def}}{=} \frac{2}{\sqrt{\pi}} \int_{\xi=0}^{\chi} e^{-\xi^2} d\xi\,, \tag{3.11}$$

$L/\sqrt{2}$ is the Gaussian decaying scale, v_0 is the jet maximum speed, and we recall that x_c is the x-coordinate of the lower-layer eddy center.

Based on Napolitano et al.'s (2019) shipboard observations of the BC in Tubarão Bight, we set $L = 25\,\text{km}$, so that the jet width is 50 km. The AVISO analysis in section

2 reveals that the BC maximum speed in Tubarão Bight ranges from about 0.1 to about 0.5 $\mathrm{m\,s^{-1}}$ (figure 3.2). To study the model dependency on this variability, we conduct three sets of experiments with $v_0 = [0.1, 0.2, 0.5]\,\mathrm{m\,s^{-1}}$, representing a WEAK, MEAN, and STRONG BC regime. Figure 3.4 shows the model velocity profiles at $y = y_c$ for the lower-layer IWBC Eddy (dashed line) and the three selected velocities for the upper-layer BC jet (solid lines).

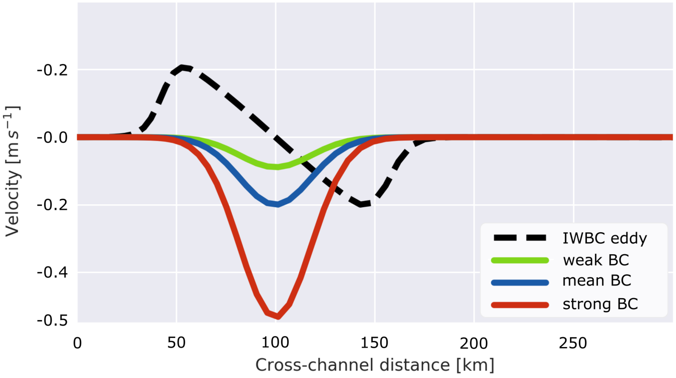

Figure 3.4: Velocity profiles of the model across the center of the eddy. The dashed line shows the simulated IWBC Eddy velocity in the lower layer. Solid lines represent the simulated BC in the upper layer: (i) the green line represents the WEAK BC case; (ii) the blue line represents the MEAN BC case; and (iii) the red line represents the STRONG BC case.

We choose a channel length long enough to prevent downstream-propagating anomalies from reentering the domain and spoiling the solutions in the lower-layer eddy region. Table 3.1 contains the parameters of all experiments discussed below. In these experiments, the channel width is 600 km, and the channel length varies from 2400 to 4800 km, with the longer channels for stronger jet experiments. The number of Chebyshev and Fourier modes are such that, in the middle of the domain, the grid space is $\Delta x \approx \Delta y \approx 10\,\mathrm{km}$. We tested the sensitivity of the solutions by running the model with double resolution and found only small differences.

We conduct both nonlinear and linear experiments for a WEAK, MEAN and STRONG upper-layer jet. The linear calculations are performed by suppressing the non-

Table 3.1: Parameters used in the Dedalus experiments. For every experiment, we set an IWBC eddy radius r_e of 90 km and eddy speed v_e of 0.2 m s^{-1}; we set the BC width to 50 km, and the jet position aligned with the IWBC eddy center. The deformation radius is 50 km.

Experiment		Channel		BC
name	ν (m^2 s^{-1})	L^y (km)	n^y	spd (m s^{-1})
linear WEAK	02	2400	264	0.10
linear MEAN	04	2400	264	0.20
linear STRONG	12	2400	264	0.50
nonlinear WEAK	02	2400	264	0.10
nonlinear MEAN	04	3600	384	0.20
nonlinear STRONG	12	4800	512	0.50

linear term $J(\psi, \nabla^2\psi)$ from the full Jacobian $J(\psi, q)$ in (3.1), since $J(\psi, -Rd^{-2}\psi) = 0$.

4 Model results and discussion

Linear experiments

Figure 3.5 shows snapshots of streamfunction for the linear MEAN experiment ($v_0 = 0.2\,\mathrm{m\,s^{-1}}$). We only display the results for a region that extends about 300 km from the western boundary and about 450 km (150 km) south (north) of the lower-layer eddy. This channel strip is meant to represent the region between Abrolhos Bank (18 °S) and the Cape Frio High (24 °S), between the 200-m and 3500-m isobaths (see figure 3.1).

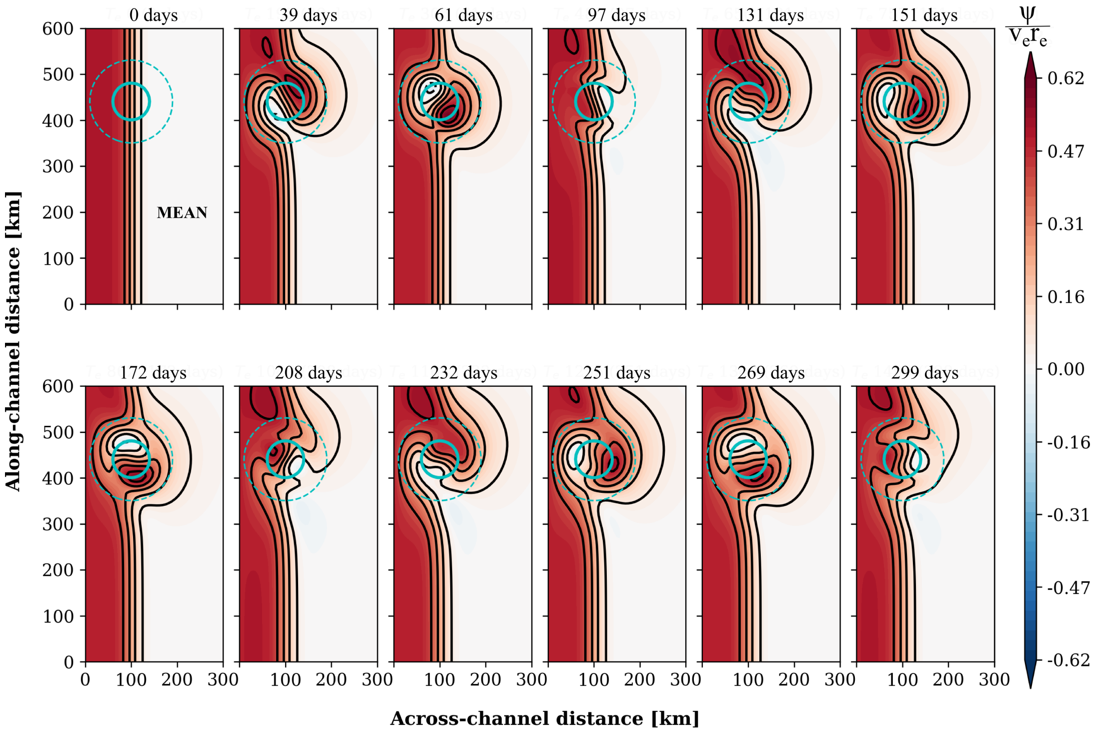

Figure 3.5: Dedalus snapshots for ∼300 days of simulation for the linear WEAK experiment. The colors and black streamlines represent the upper-layer modeled BC. The dashed cyan line represents the zero-velocity contour of the modeled lower-layer eddy, and the solid cyan contour represents the maximum eddy velocity.

The dynamics here are governed by

$$q_t = -J\left(\psi, \frac{\psi_2}{R_d^2}\right) . \tag{3.12}$$

We emphasize that the tendency on the right of (3.12) is linear because ψ_2 is prescribed, and topographic steering by the lower-layer eddy drives changes in ψ. (The dissipation term $-\nu\nabla^2\zeta$ is negligible, and the solutions are essentially inviscid.) The evolution of the flow for the MEAN experiment in figure 3.5 is also typical for the other linear experiments (WEAK and STRONG, not shown), and differs from the parallel flow condition in (3.3), since the steady state approximation is relaxed and $q_t \neq 0$. The upper-layer jet immediately responds to the lower-layer eddy by developing a meander with a cyclone (a crest) upstream of the eddy center and an anticyclone (a trough) downstream of the eddy center. This wavy perturbation has a wavelength of about 40-50 km, is trapped and seems to propagate around the lower-layer eddy. With this trapped-wave propagation, the meander appears to wear down and form periodically. No steady state is achieved.

In short, a stationary eddy (a Vitória Eddy) is not formed in the linear model, regardless the jet strength. We now turn to the evaluation of nonlinear solutions and discuss the parameters under which such eddy is formed.

Nonlinear experiments

Figure 3.6-A through 3.6-R show sequences of snapshots of the nonlinear evolution of the streamfunction for the cases of WEAK, MEAN, and STRONG upper-layer jet; all other flow parameters are fixed. In all three cases, the upper-layer jet quickly begins to meander in the lower-layer eddy region, but the solutions then begin to diverge. In the WEAK upper-layer jet case (figure 3.6-A to F), the meander grows to finite amplitude locally, with a strong cyclone (closed streamlines with $\psi > 0$) developing on top of the lower-layer eddy and an anticyclone (closed streamlines with $\psi < 0$) in the lee of the eddy (figure 3.6-C to F). The meander reaches its strongest amplitude in about 19 days (figure 3.6-D).

While the WEAK case leads to local meandering, the strong upper-layer jet rapidly advects the perturbation generated on top of the lower-layer eddy, which undergo explosive downstream growth (figure 3.6-G to L). In 17 days the cyclonic meander has grown to finite amplitude and travelled 300 km downstream (figure 3.6-D). Interestingly, an anticyclonic vortex forms in the wake of the cyclonic meander. This vortex interacts nonlinearly with the meander, growing in amplitude as both features are advected downstream (see sequence in figures 3.6-I to L).

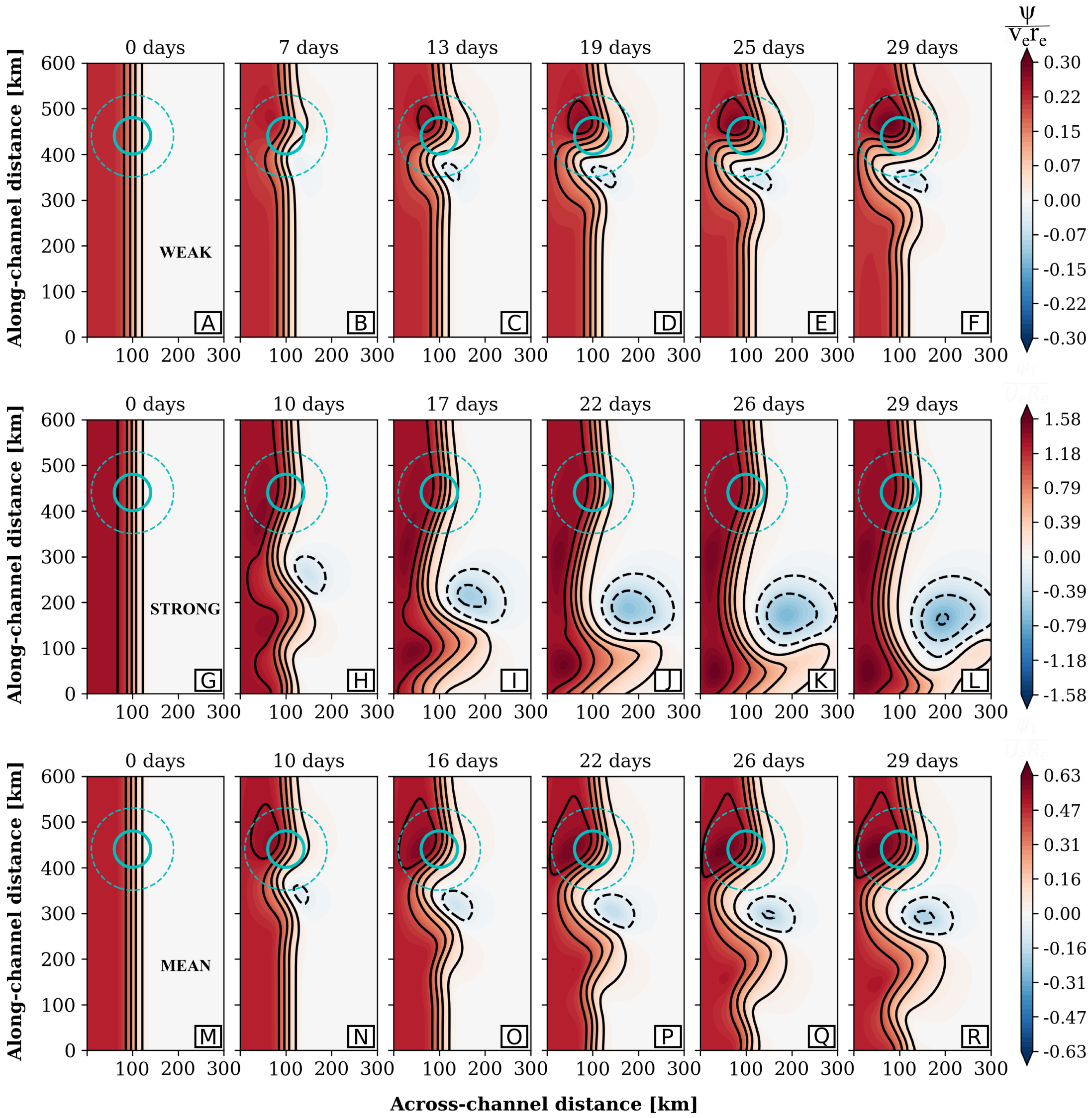

Figure 3.6: Dedalus snapshots for ∼30 days of simulation for the nonlinear (A-F) WEAK, (G-L) MEAN, and (M-R) STRONG experiments. The colors and black streamlines represent the upper-layer modeled BC. The dashed cyan line represents the zero-velocity contour of the modeled lower-layer eddy, and the solid cyan contour represents the maximum eddy velocity.

The MEAN upper-layer jet case displays features of these two extreme regimes (figure 3.6-M to R). The meander grows locally, but there is also downstream advection and growth. Given this partial downstream advection of the initial perturbations, the local meander has a smaller amplitude than in the WEAK case. In cases where the eddy is formed, the anticyclonic part of the meander formed by the initial trigger (which is in the offshore part of the bump) is advected by the nonlinear term $J(\psi, \zeta)$. However, the cyclonic part of the meander remains trapped between the wall and the lower layer eddy stretching $J(\psi, \frac{\psi_2}{R_d^2})$.

Thus the jet velocity controls the magnitude of the nonlinear term $J(\psi, \zeta)$, which in turn drives changes in the flow: the stronger the upper-layer jet, the largest the initial $J(\psi, \zeta)$, and the faster the perturbations are advected downstream.

Our nonlinear quasi-steady solutions resemble the flow over topography problem discussed by Ingersoll (1969), who explored the formation of Taylor columns and the circulation around a topographic bump of different heights. Conversely, we vary the upper-layer jet velocity $v_0 = [0.1, 0.2, 0.5]\,\mathrm{m\,s^{-1}}$ and fix the "topographic bump" as an anomaly imposed by the steady lower-layer eddy (the IWBC Eddy),

$$h \overset{\text{def}}{=} \frac{h_b}{H} = \frac{\Psi_2}{f_0 R_d^2} = \frac{v_e}{f_0 R_d} \approx 0.08\,, \tag{3.13}$$

where $\Psi_2 = v_e R_d$ is the magnitude of the lower-layer streamfunction (v_e =0.2 $\mathrm{m\,s^{-1}}$ is the eddy velocity). With scales $R_d = 50\,\mathrm{km}$ and $f_0 = 5 \times 10^{-5}$, we obtain the Rossby number

$$R_o \overset{\text{def}}{=} \frac{v_0}{f_0 R_d} = [0.04, 0.08, 0.2] \tag{3.14}$$

for the WEAK, MEAN and STRONG upper-layer jet cases, respectively. Ingersoll (1969) remarks that a flat obstacle (a cylinder) yields solutions with closed streamlines when $h/R_o \geq 2$. In our experiments, we obtain closed streamlines not only with the weak upper-layer jet, where $h/R_o = 2$, but also in the MEAN case, where $h/R_o = 1$, possibly due to boundary effects.

A local steady state

We discussed above the first 30 days of simulations because it is the approximate time it takes for the meanders to reach finite amplitude locally or for the downstream meander to leave our region of interest. The changes after these 30 days are relatively small, and the solution slowly approaches an approximate steady state *within* the 300 × 600-km channel strip of the snapshot figures.

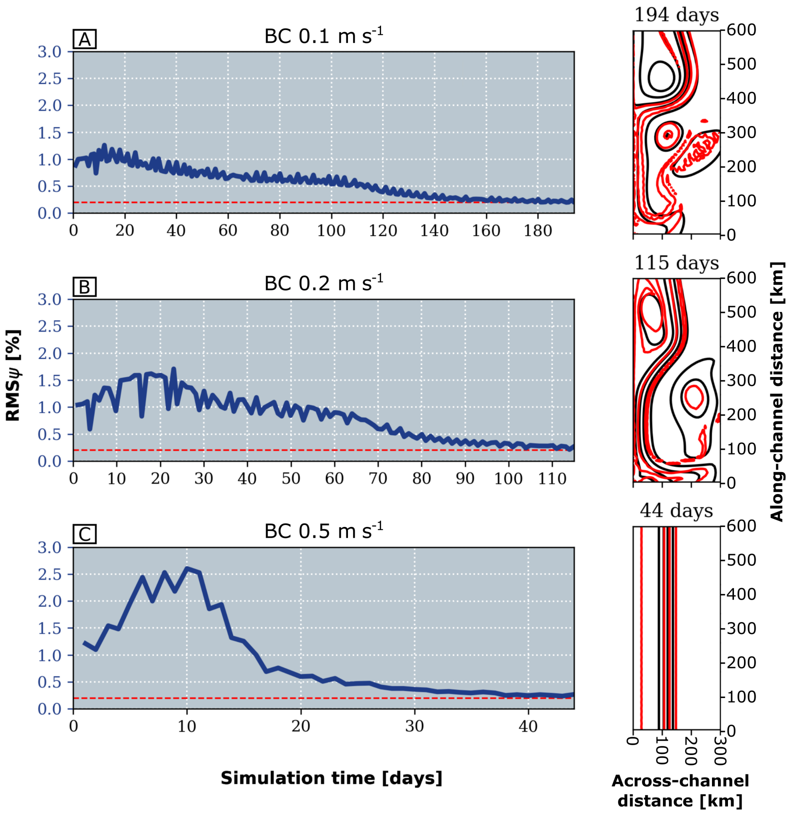

Figure 3.7: Root mean square differences between daily streamfunction fields. In the left panels, the dashed red line represents the $2{\times}10^{-3}$ threshold; in the right panels, solid red lines represent potential vorticity and solid black lines represent streamfunction for (A) the WEAK BC, (B) the MEAN BC and (C) the STRONG BC.

To assess the convergence of the solution to this local steady state, we define an iterative normalized root mean square streamfunction

$$RMS_{\psi} \overset{\text{def}}{=} \sqrt{\frac{\sum(\psi_i - \psi_{i-1})^2}{\sum \psi_i^2}}, \tag{3.15}$$

where i represents simulation days. A reasonable criterion to define a local steady state is that $RMS_{\psi} \leq 2 \times 10^{-3}$; i.e., the solution varies by less than 0.2% from the previous day.

Figure 3.7 shows timeseries of RMS_{ψ} for the BC nonlinear cases. The time taken to achieve an approximate steady state varies widely across the simulations. (Note the different time range in figures 3.7-A, B and C.) In the WEAK case, the solution reaches a steady state in 194 days (panel A), and in the MEAN case (panel B) it takes 115 days. In both cases the steady solution consists of a standing meander, with the jet deflecting toward the boundary downstream of the lower-layer eddy. On top of the lower-layer eddy, both solutions display closed contours of streamfunction and potential vorticity. Another common feature is a pinched-off anticyclonic eddy downstream of the meander and away from the boundary.

The strong upper-layer jet (STRONG BC, panel C) reaches an approximate steady state much faster, in about 44 days. While perturbations induced by the lower-layer eddy grow explosively as they are advected downstream, these transient eddies are swept out of the domain of interested. There are no closed contours of streamfunction and potential vorticity; the steady solution is a straight jet similar to the initial condition.

Linear vs nonlinear dynamics

We now step further into the dynamics of our nonlinear experiments to investigate the contribution of the linear relative to the nonlinear term of the solution for the WEAK, MEAN, and STRONG cases. Expanding the Jacobian in the potential vorticity equation (3.1) yields

$$J(\psi, q) = \underbrace{J(\psi, \zeta)}_{\text{nonlinear}} + \underbrace{J(\psi, \psi_2/R_d^2)}_{\text{linear}}, \tag{3.16}$$

where we recall that $\zeta = \nabla^2\psi$ is the relative vorticity. The linear term on the right of (3.16) represents the steering of the upper-layer flow by the lower-layer eddy, and it scales as

$$\text{LINEAR} \sim R_d^{-4}\Psi\Psi_2 = R_d^{-2} v_0 v_e \,. \tag{3.17}$$

The nonlinear term is the advection of relative vorticity by the upper-layer flow, and it has magnitude

$$\text{NONLINEAR} \sim R_d^{-4}\Psi^2 = R_d^{-2}v_0^2\,. \tag{3.18}$$

In the above scaling we assumed that the eddy quantities have deformation radius length scales. The ratio between these two terms is

$$\frac{\text{LINEAR}}{\text{NONLINEAR}} \sim \frac{\Psi_2}{\Psi} = \frac{v_e}{v_0} = \frac{h}{R_o}\,, \tag{3.19}$$

where h is the non-dimensional amplitude of the lower-layer eddy, which is equivalent to a topographic Rossby number [see the discussion surrounding (3.13)].

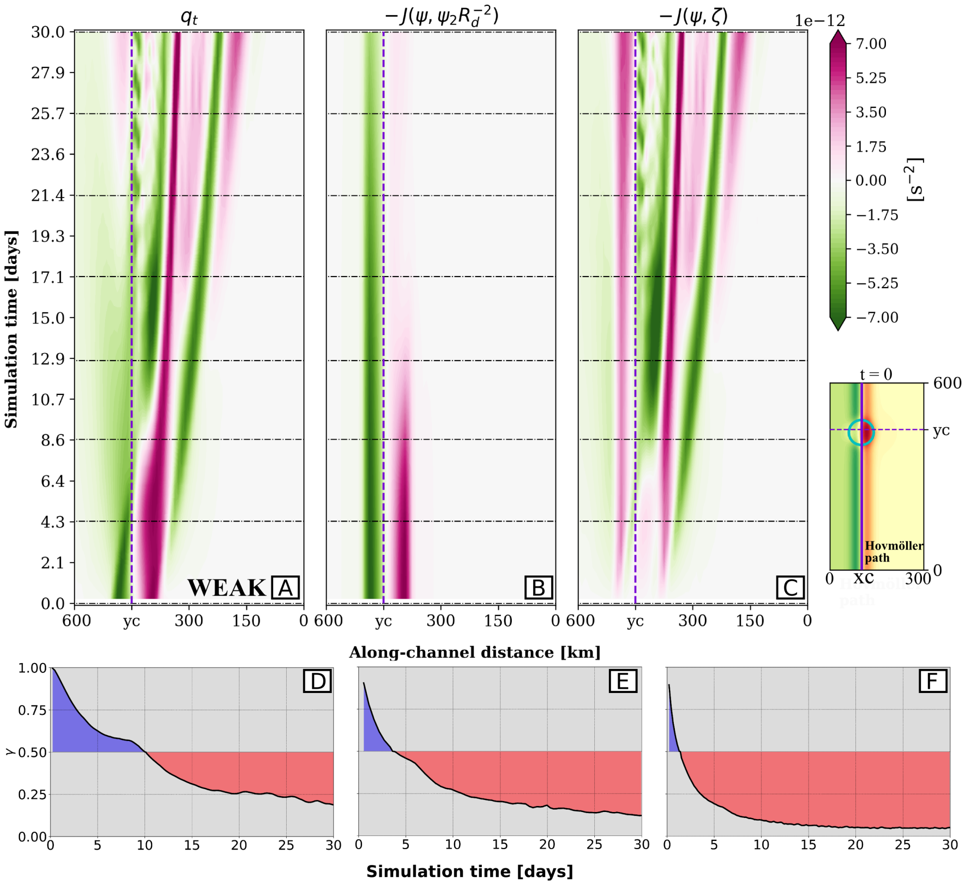

Figure 3.8: Hovmöller diagram of (A) variation of potential vorticity, (B) linear term of the Jacobian, (C) nonlinear term of the Jacobian in (3.1) for the nonlinear WEAK BC experiment. The vertical dashed line represents the center of the eddy at yc, separating the dynamics upstream and downstream of the lower-layer eddy. Horizontal dashed lines represent timesteps of the analyzed snapshots. The potential vorticity at $t = 0$ is shown in the lower right. The timeseries show the ratio between the linear and nonlinear terms throughout the simulation for (D) WEAK, (E) MEAN and (F) STRONG cases.

For the WEAK case, this ratio is 2. Thus we expect that both terms are important, with the linear term dominating within the lower-layer eddy region. Figure 3.8-A displays an along-channel Hovmöller diagram of the potential vorticity tendency (q_t) through the center of the lower-layer eddy ($x = x_c$). The vertical dashed line is $y = y_c$, the center of the lower-layer eddy. Panels B and C of figure 3.8 breaks down this tendency into the contributions of the linear and nonlinear terms in (3.16). This linear term provides the initial trigger for the jet meandering in the lower-layer eddy region, with the upper-layer jet being steered by the lower-layer eddy. In the initial few days of the simulation, the linear term accounts for most of the potential vorticity tendency. Downstream of the lower-layer eddy, where the linear term vanishes, the nonlinear term takes over, with the formation of a strong anticyclonic eddy and the slow propagation of a small meander (see the slanted pink and green strips in figure 3.8-C). To quantify the relative importance of linear and nonlinear dynamics, we compute a timeseries of

$$\gamma \overset{\text{def}}{=} \frac{\text{rms(linear)}}{\text{rms(linear+nonlinear)}}\,, \tag{3.20}$$

where rms denotes root mean square. The ratio γ quantifies the relative importance of the linear and nonlinear terms, being 1 for fully linear and zero for fully nonlinear dynamics.

Figure 3.8-D shows this ratio for the WEAK experiment. As indicated in the Hovmöller diagrams, the dynamics are fully linear at the beginning of the meandering process, but nonlinear advection becomes important after one day, and it dominates the dynamics after 10 days.

Figures 3.8-E and F show the ratio γ for the MEAN and STRONG experiments. In all cases the initial trigger is a linear process—the steering of the upper-layer jet by the lower-layer eddy. But the nonlinear takeover occurs more rapidly with the increasing upper-layer jet speed (and associated reduction of the h/R_o parameter). For the STRONG upper-layer jet experiment, where the local meandering is weak and most of the variability is accounted for by downstream meander growth, nonlinear advection dominates after about 2 days, and after 15 days it accounts for essentially all the dynamics. In this STRONG case, after the initial trigger, the upper-layer jet barely feels the lower-layer eddy, and it satisfies standard two-dimensional dynamics $q_t \approx -J(\psi, \zeta)$.

5 Final remarks

Using a simple theoretical model, we show that the intermediate-layer IWBC recirculation may be strong enough to steer the Brazil Current, leading to the formation of the Vitória Eddy above this recirculation. Thus the topographically constrained intermediate flow likely influences the Brazil Current eddying circulation. Our model simulates the IWBC recirculation as a steady eddy that acts like a topographic bump in a barotropic model, and the Vitória Eddy formation is treated effectively as a flow past topography problem. Thus the Vitória Eddy can be addressed as a stagnant region in the solution, i.e., a Taylor-column.

Our model results suggest that the initial trigger for the Vitória Eddy is a linear process—the steering of the Brazil Current jet by the IWBC recirculation flow. But nonlinearity, through advection of the anticyclonic portion of relative vorticity anomaly generated by the linear topographic steering of the Brazil Current, is also needed for the Vitória Eddy growth. In the linear experiments, the Vitória Eddy does not form (figure 3.5). But in the nonlinear experiments, the steady IWBC recirculation steers the current. When the Brazil Current jet is relatively weak ($\leq 0.2\,\mathrm{m\,s^{-1}}$), a standing meander forms on top of the IWBC recirculation, and nonlinearity drives downstream meander growth (figures 3.6-A to F; and 3.6-M to R). In this case, downstream of the recirculation, the

Brazil Current veers rapidly toward the boundary. In the local steady state the Brazil Current is attached to the boundary south of the Vitória Eddy (figure 3.7-A). When the Brazil Current is very strong ($0.5\,\mathrm{m\,s^{-1}}$; figure 3.6-G to L), the potential vorticity anomalies generated on top of the recirculation are quickly swept away, leading to explosive downstream meander growth. In this case, no Vitória Eddy is formed.

Given the complex structures and interactions depicted by our AVISO analysis (figure 3.3), our model cannot be used to fully explain the Vitória Eddy formation or to quantitatively represent the observed patterns. But it is certainly an initial step toward understanding the process. Future studies could add more complexity to the model, including changes in the upper-layer jet velocity, the Brazil Current feedback into the IWBC recirculation [i.e., adding an evolution equation for $v = v_0$ in (3.10) and for q_2, respectively]. Also, effects of topography, and eddy decay processes could be included. Recently, Napolitano et al. (2019) showed that the variability in the region is dominated by westward-propagating eddies, which are likely to complicate the picture. To further address the mechanisms that drive the Vitória Eddy, we call for a hierarchy of models, from solutions as simple as ours to idealized primitive-equation simulations to complex regional numerical models.

Acknowledgments

We thank Frank O. Smith for copy editing and proofreading this manuscript. This study was financed in part by Coordenação de Aperfeiçoamento de Pessoal de Nível Superior—CAPES, Brazil—Finance Code 001 and by Projeto REMARSUL (Processo CAPES 88882.158621/2014-01), Projeto VT-Dyn (Processo FAPESP 2015/21729-4) and Projeto SUBMESO (Processo CNPq 442926/2015-4). Altimeter products were produced by Ssalto/Duacs available at `www.aviso.altimetry.fr/duacs/`.

CHAPTER 4.

SUBMESOSCALE PHENOMENA DUE TO THE BRAZIL CURRENT CROSSING OF THE VITÓRIA TRINDADE RIDGE

Manuscript submitted in August 2020, to the *Journal of Geophysical Research–Oceans*. This manuscript is co-authored by Ilson C. A. Silveira, Amit Tandon, and Paulo H. R. Calil

Abstract

At 20.5 °S, the Brazil Current and the Intermediate Western Boundary Current interact with a quasi-zonal seamount chain, the Vitória-Trindade Ridge (VTR). While the mesoscale variability generated due to these western boundary currents crossing of the VTR has been recently studied, the submesoscale dynamics associated with such features have never been addressed. Here, we use new observations and a 2 km-resolution model to analyze the role of the VTR seamounts in the region submesoscale dynamics, their seasonality, and instabilities. We present new high-resolution velocity and density observations that capture submesoscale features associated with the flow. At these regions, potential vorticity reveals patches of symmetrically-unstable flow close to seamounts. The horizontal resolution ($\Delta x \simeq 1.5\,\mathrm{km}$) of our quasi-synoptic observations (10 h) partially resolves submesoscale instabilities. Our ROMS simulation shows that submesoscale activity in the region typically follows the seasonal mixed-layer cycle. But this seasonality is masked where the flow intercepts topography, generating deeper unstable regions. A spatio-temporal analysis of the vertical buoyancy fluxes points to flow-topography interactions as the main source for these recurrent, deeper instabilities. And these instabilities can displace isopycnals several meters, leading to important changes in nutrients and light, as well as enhance the carbon sink through submesoscale subduction. As the VTR emerges as a submesoscale hotspot in the oligotrophic South Atlantic, the lack of observations still remains the main obstacle to better understand submesoscale processes in the region.

1 Introduction

At latitudes north of which it becomes a robust western boundary current, the newly-formed, poleward-flowing Brazil Current (BC) encounters a zonal seamount chain—the Vitória-Trindade Ridge. Located at 20.5 °S, with seamounts reaching up to 30 m below the surface, the Vitória-Trindade Ridge poses an obstacle for the typically 150 m-deep BC southward path (Evans et al., 1983; Costa et al., 2017). Underneath the BC, the Intermediate Western Boundary Current (IWBC) flows equatorward, crossing the ridge in the opposite direction (Legeais et al., 2013; Napolitano et al., 2019). From 28 °S to 21 °S, the two opposing flows of the BC and the IWBC compose the so-called Brazil Current System (Silveira et al., 2004). The currents are generally vertically aligned, and frequently interact (e.g., Silveira et al., 2004, 2008; Mano et al., 2009). Downstream of the Vitória-Trindade Ridge, at 21.6 °S, where the BC reattaches to the slope after crossing the ridge, new microstructure data suggested that vertical shear below the surface mixed layer may drive intense turbulent mixing activity (Lazaneo et al., 2020). Individually, the BC and the IWBC cross the Vitória-Trindade Ridge in opposite directions, negotiating its channels and seamounts. The IWBC develops topographically forced structures and strong mesoscale activity (e.g., Legeais et al., 2013; Costa et al., 2017; Napolitano et al., 2019). The BC also develops mesoscale eddies up and downstream the ridge, e.g. the cyclonic Vitória Eddy (Schmid et al., 1995; Arruda and Silveira, 2019) and the anticyclonic Abrolhos Eddy (Soutelino et al., 2011, 2013).

Submesoscale motions in the ocean are characterized by horizontal scales of $\mathcal{O}(10)$ km, vertical scales of $\mathcal{O}(10)$ m and time scales of $\mathcal{O}(1)$ day (Capet et al., 2007). At these scales, typical mesoscale Rossby $[U/fL \ll \mathcal{O}(1)]$ and Richardson $[N^2H^2/U^2 \gg$

$\mathcal{O}(1)$] numbers become $\mathcal{O}(1)$ in localized regions (Mahadevan and Tandon, 2006). There, the dynamics are governed by submesoscale, which bridges hydrostatic to non-hydrostatic motions, and leads to vertical velocities of $\sim$100 m day^{-1} [$\mathcal{O}(10^{-3})\,\mathrm{m\,s^{-1}}$] within the mixed layer, against the observed $\sim$1 m day^{-1} [$\mathcal{O}(10^{-5})\,\mathrm{m\,s^{-1}}$] of the mesoscale (Thomas et al., 2008).

Earlier studies have hinted at the importance of ocean fronts by showing that they are preferential regions for the generation of large vertical velocities and the emergence of ageostrophic dynamics (e.g., Pollard and Regier, 1992; Rudnick, 1996). Klein et al. (1998) investigated the stirring of thermohaline anomalies and identified sharp thermohaline fronts driven by the mesoscale eddy field. At these fronts, the three-dimensional ageostrophic circulation is key in controlling their dynamics, strength and spatial distribution. Mahadevan and Archer (2000) modeled the impact of fronts on the mesoscale nutrient supply at different spatial resolutions. Their study identified that processes occurring at the scale of the fronts were not properly resolved by mesoscale. More recent investigations have accounted for submesoscale dynamics responsible for these and other important processes, such as mixed layer restratification (e.g., Boccaletti et al., 2007), regulation of primary productivity (e.g., Lévy et al., 2012), the vertical motion and distribution of tracers in the upper ocean (e.g., Mahadevan and Tandon, 2006; Thomas et al., 2008; Calil, 2017), and the forward cascade of energy (e.g., Capet et al., 2008).

New technologies and techniques allowed *in-situ* observations of submesoscale processes. Rocha et al. (2016a) analysed 13-yr of shipboard-ADCP data across Drake Passage, showing that ageostrophoc motions account for half of the surface kinetic energy at scales of $\mathcal{O}(10)$ km. Also in the Drake Passage, Viglione et al. (2018) used gliders to show submesoscale motions evolved differently in distinct geographical locations.

Ramachandran et al. (2018) observed dynamical signatures indicative of submesoscale processes at a salinity front in the Bay of Bengal. Latest developments in submesoscale sampling include the observation of two-dimensional velocity gradients.

Studies concerning flow-topography interactions at submesoscale are less common in the literature. It is known that islands and seamounts occupy less than 5 % of the ocean floor (Rogers, 2019). They interact with the adjacent flow boosting ocean processes, such as diapycnal mixing (e.g., Lueck and Mudge, 1997), generation and breaking of internal waves (e.g., Nikurashin and Ferrari, 2010), and dissipation of kinetic energy (e.g., Garabato et al., 2004). These flow-topography interactions may inject enough shear into the mesoscale field, leading to the formation of smaller-scale eddies and filaments (cf. D'Asaro, 1988; Molemaker et al., 2015; McWilliams, 2016; Gula et al., 2016; Morvan et al., 2019). Although the precise BC path through the Vitória-Trindade Ridge is still uncertain, the current must cross this seamount-populated area, where submesoscale-resolution observations are scarce.

In this paper, we provide new observations—with enough horizontal resolution to capture the submesoscale variability associated with the BC and the IWBC crossing the Vitória-Trindade Ridge—and a submesoscale-permitting numerical simulation. We aim to (i) describe the observed submesoscale-like features and test their stability, (ii) characterize the submesoscale instabilities and their seasonality, and (iii) analyze the role of the Vitória-Trindade Ridge seamounts in the BC submesoscale dynamics.

2 Submesoscale observations

In order to study flow-topography interactions in the Vitória-Trindade Ridge, we use velocity data from a 75-kHz shipboard Acoustic Doppler Current Profiler (sADCP), density derived from a towed Underway Conductivity, Temperature and Depth probe (uCTD), and local topography data from 12 and 38 kHz vessel-mounted Echosounders. We obtained the data from a 20-day cruise that took place the austral summer of 2017 (from 27 January to 16 February) onboard the RV Alpha Crucis. We analyzed data from the three westernmost transects of the entire dataset, i.e., in the region where the BC flows through the seamounts of the Vitória-Trindade Ridge (see figure 4.1-A). At each transect, the velocity and mass structure data are synoptic: in transects T1, T2 and T3, we covered approximately 125, 45, and 60 km in about 11, 7, and 7 h respectively. The longer transect (T1) occupied less than ⅓ of the inertial period ($^{2\pi}/_{f}$), estimated to be $\sim$35 h in the region. Since transects were sampled faster than the inertial time scales of the submesoscale, we may estimate the spatial gradients at each transect from the synoptic snapshots (Thomas et al., 2008).

Figure 4.1 displays the synoptic picture obtained for the three transects during the *Ilhas* survey. We processed the short-time averaged (120 s) sADCP data using the CODAS package (Firing et al., 1995). We then manually removed spurious data, which bypassed the previous processing stages, and discard the data acquired during stations. Using only downcast temperature and salinity profiles from the uCTD casts, we calculated the σ_0 potential density. To define the mixed-layer depth (MLD), we modified the difference criteria (e.g., Montégut et al., 2004), and set it as the depth of 0.25 kg m^{-3} increment from the value of σ_0 at 2 m. South of Abrolhos Bank, transect T1 (figures 4.1-B, E) exhibits a 0.5 m s^{-1} jet flowing past the topography, probably escaping through the Besnard passage into the Tubarão Bight. Altimeter-derived velocities (not shown) indicate this $\sim$30 km-wide jet to be a branch of the BC. Our data shows the BC as a 100 m-deep jet, which is not constrained by the summer shallow MLD of $\sim$30 m, and occupies the upper seasonal pycnocline. At 90 km from the beginning of the transect, outcropping isopycnals mark the limit of the jet, forming a sharp front (figure 4.1-E). Between ∼50–60 km, at 40–60 m depth, we depict a 10 km-wide patch of higher velocities, which suggests the presence of a shingle shed by the BC. On the density section, small lenses within the pycnocline, between 40–80 km, hint at the presence of anticyclonic intrathermocline eddies (cf. McWilliams, 1985; D'Asaro, 1988). Below 150 m in figure 4.1-B, T1 captures the quasi-permanent, 0.2 $\mathrm{m\,s^{-1}}$ IWBC cyclonic recirculation, as described by Costa et al. (2017) and Napolitano et al. (2019).

The south-north oriented transect T2 (figures 4.1-C, F) cuts through the Main channel of the Vitória-Trindade Ridge. A second 100 m-deep, 10-km wide branch of the BC flows westward close to the northern bank at 0.5 $\mathrm{m\,s^{-1}}$. Below the 50-m mixed layer, a 10 km counterflow is also seen at 30 km, indicating either a recirculation of the BC, a cyclonic eddy, or a detached filament (figure 4.1-C). Density from T2 displays two distinct interthermocline eddies within the MLD, centered at 5 km and 25 km; at 80 m, a slightly displaced isopycnal suggests the presence of a cyclone, with the smaller eddies at its border (figure 4.1-F). The IWBC at about 0.5 $\mathrm{m\,s^{-1}}$ strength escaping Tubarão Bight through the Main channel is captured on the northern 30 km of T2; at the southern end of T2, below 200 m, a patch of opposite (westward) velocities is seen next to the seamount (figure 4.1-C).

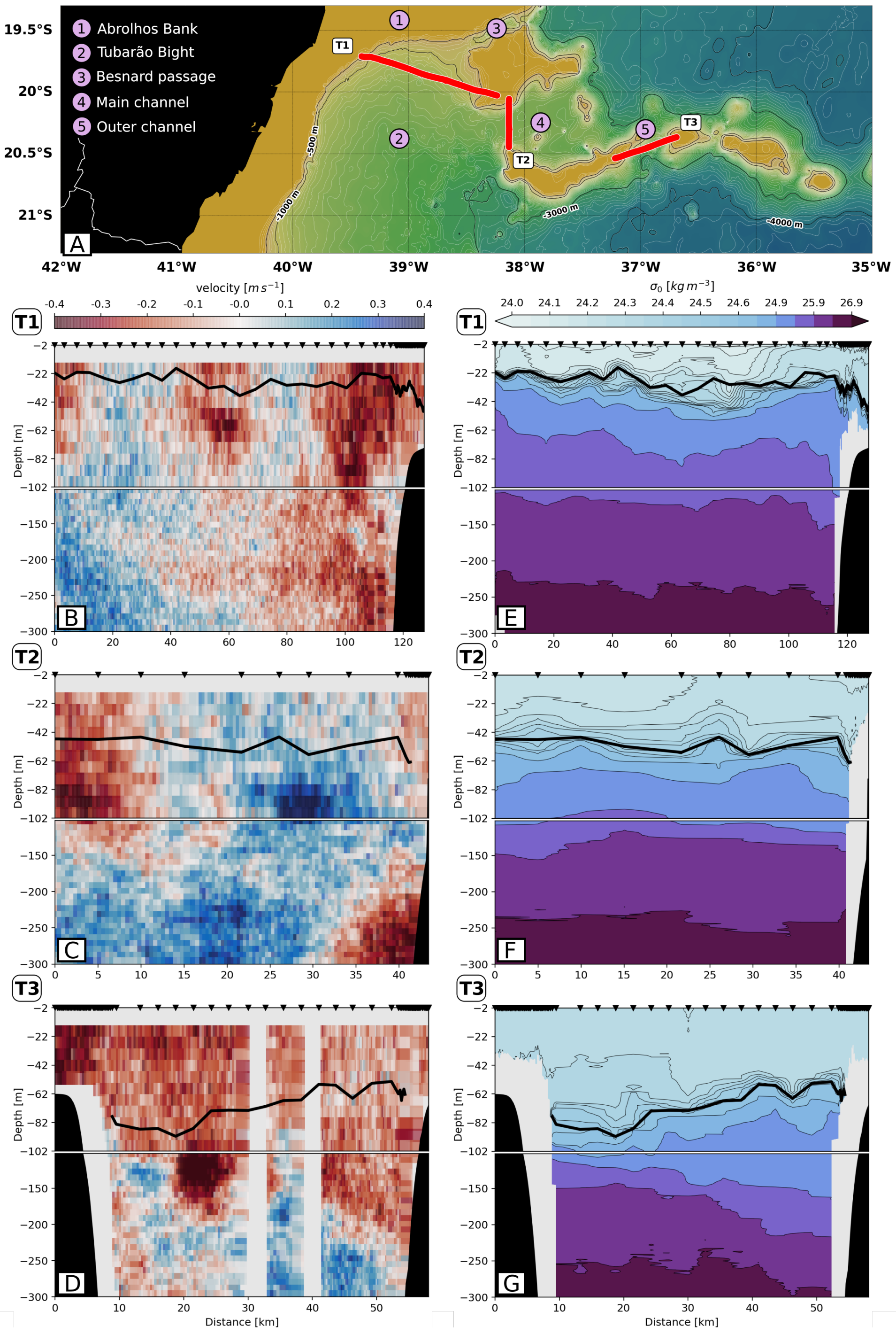

Figure 4.1: The *Ilhas* austral summer survey. (A) Vitória-Trindade Ridge region map with the dark yellow shading representing depths shallower than 300 m. Red lines indicate the location of transects T1, T2 and T3. (B, C, and D) Short-time averaged shipboard-ADCP cross-transect velocities with a blowout on the upper 100 m. Red pixels represent southward/westward velocities, while blue pixels represent northward/eastward velocities. (E, F, and G) Underway-CTD density with a blowout on the upper 100 m. Darker colors represent denser waters. The black thick line shows the depth of the mixed layer. Black triangles mark the position of the uCTD casts.

At 37 °W, a band of southward velocities spans across the Outer channel in transect T3 (figures 4.1-D, G). The highest surface velocities occur on top of the westbound seamount. The maximum MLD is 90 m, shoaling 40 m from west to east, where isopycnals are packed and stratification is strong. Below 200 m, a northward-flowing branch of the IWBC crosses the ridge through this channel, which agrees with modeling results by Costa et al. (2017).

On the western portion of T3, a strong southward flow ($>0.7\,\mathrm{m\,s^{-1}}$) appears in a background of northward flow. This pattern is consistent with an intrathermocline dipole of southward propagation, where the central southward flow represents the interface between the two eddies. Either a dipole, a filament or an isolated intrathermocline eddy, this structure—as well as the counterflow observed in T2—are likely to develop due to lateral shear between the IWBC and the seamount topography. This mechanism of eddy generation due to flow-topography interactions was first proposed by D'Asaro (1988), during the observation of submesoscale eddies in the Arctic Ocean.

Observational evidence of submesoscale instabilities at the Vitória-Trindade Ridge

Submesoscale instabilities act on the forward cascade of kinetic energy, conveying energy from the mesoscale *en route* to dissipation (Capet et al., 2008). In the process, ageostrophic secondary circulations arise from different types of submesoscale instabilities, leading to restratification. Gravitational instability occurs when there is gain of kinetic energy via buoyancy fluxes in the presence of unstable stratification ($N^2 < 0$), which consumes readily available potential energy (Thomas et al., 2013). Frontal instabilities present a secondary circulation associated with frontal shear (Molemaker et al., 2010). This class of instability includes symmetric instability—which extracts kinetic energy from the vertical shear of geostrophic flows (cf. Taylor and Ferrari, 2010; Thomas et al., 2013)—and ageostrophic baroclinic instability, which extract available potential energy by slumping isopycnals (cf. Fox-Kemper et al., 2008). While symmetric instabilities are essentially two-dimensional, ageostrophic baroclinic instabilities result also in vertical fluxes. Inertial instability (a.k.a. centrifugal instability) develops in anticyclonic motions with relative vorticity ($\zeta \equiv v_x - u_y$) stronger than planetary vorticity (f), drawing energy from the horizontal shear of the flow (cf. Thomas et al., 2013; Gula et al., 2016). According to Thomas et al. (2013), these instability types can be differentiated by their sources of kinetic energy. This can be conveniently visualized by the angle

$$\phi_{Ri_B} = \tan^{-1}(-Ri_B^{-1})\,. \tag{4.1}$$

where the balanced Richardson number is defined as

$$Ri_B = \frac{N^2 f^2}{M^4}\,. \tag{4.2}$$

Both N^2 and M^4 relate to the spatial variations of the buoyancy, defined as $b \equiv -g(\rho/\rho_0)$, where g is the acceleration due to gravity, ρ is the density, and ρ_0 =1025 kg m^{-3} is the reference density. $N^2 \equiv b_z$ is the stratification, and $M^4 \equiv b_x^2 + b_y^2$ is the magnitude of the lateral buoyancy gradient. (Subscripts indicate derivatives in the corresponding Cartesian directions.)

Thomas et al. (2013) state that the instability is gravitational when $-180° < \phi_{Ri_B} < -135°$ and is a hybrid of gravitational and symmetric when $-135° < \phi_{Ri_B} < -90°$. For anticyclonic ζ, symmetric instability arises for $-90° < \phi_{Ri_B} < -45°$ and a hybrid of symmetric and inertial instability occur for $-45° < \phi_{Ri_B} < \phi_c$ (ϕ_c is a critical, geostrophic Rossby number). Cyclonic ζ yields symmetric instability for $-90° <$

$\phi_{Ri_B} < \phi_c$. To properly employ such classification, however, observations and numerical modeling should fully resolve these instabilities, demanding small-scale measurements (D'Asaro et al., 2011; Nagai et al., 2012, e.g.,) and large eddy simulations with grid resolution of $\mathcal{O}(1)$ aspect ratio (Thomas et al., 2013; Stamper and Taylor, 2017, e.g.,).

Observations during the *Ilhas* summer cruise typically have a horizontal resolution $\Delta x \simeq 400 \pm 200\,\mathrm{m}$ and vertical resolution $\Delta z = 8\,\mathrm{m}$ for the sADCP. For the uCTD, these resolutions are $\Delta x \simeq 1.5 \pm 1.8\,\mathrm{km}$ and $\Delta z = 1\,\mathrm{m}$. (Higher resolution at the seamount-slopes reduced the mean Δx and yielded greater deviations in the uCTD measurements.) We perform an objective analysis (correlation lengths $x = 5\,\mathrm{km}$ and $z = 25\,\mathrm{m}$) based on the sADCP vertical resolution and the uCTD horizontal resolution (i.e., the coarser resolution comparing both instruments). To better understand the limitations imposed by the scales of the *Ilhas* dataset, we calculate the length and time scales for symmetric instability, e.g. Bachman et al. (2017),

$$L_{sym} = 2\frac{U}{|f|}\sqrt{1 - Ri_B}\,, \quad \text{and} \quad T_{sym} = \frac{H}{U}\frac{\sqrt{Ri_B}}{\sqrt{1 - Ri_B}}\,, \tag{4.3}$$

and for ageostrophic baroclinic instability according to Fox-Kemper et al. (2008),

$$L_{abi} = 2\pi\frac{U}{|f|}\sqrt{\frac{2}{5}(1 + Ri_B)}\,, \quad \text{and} \quad T_{abi} = \sqrt{\frac{54}{5}}\sqrt{\frac{(1 + Ri_b)}{|f|}}\,. \tag{4.4}$$

We replace the parameters in (4.3) and (4.4) with typical scales for the BC in the Vitória-Trindade Ridge region, $0.01 \leq U \leq 0.5\,\mathrm{m\,s^{-1}}$, $30 \leq H \leq 130\,\mathrm{m}$. In Ri_B conditions favorable for symmetric instability ($0.25 \leq Ri_B \leq 0.95$, see Stone, 1966), $L_{sym} = 100\,\mathrm{m}$–$15\,\mathrm{km}$, $T_{sym} = 1\,\mathrm{min}$–$15\,\mathrm{h}$, $L_{abi} = 1$–$55\,\mathrm{km}$, and $T_{abi} = 20$–$25\,\mathrm{h}$. Therefore, our dataset of quasi-synoptic observations ($10\,\mathrm{h}$) and gridded at $\Delta x \simeq 1.5$km only *partially resolves* modes of symmetric and ageostrophic baroclinic instabilities. The reader should be aware that, whenever we classify "symmetric instabilities" hereafter, it is implicit that we are only dealing with the partial modes discussed above, i.e. the larger scale part of the submesoscale.

We assess our observations for unstable-flow conditions by calculating the two-dimensional Ertel potential vorticity q_{2D} using the same one-ship approximation employed in recent studies, e.g. Ramachandran et al. (2018), Viglione et al. (2018), and Lazaneo et al. (2020). In this assumption, we neglect the across-transect gradients of the potential vorticity (PV), expressed by

$$q = (f\vec{k} + \nabla \times \mathbf{u}) \cdot \nabla b \, . \tag{4.5}$$

In (4.5), $\mathbf{u} = (u, v, w)$ and $\nabla = (\partial_x, \partial_y, \partial_z)$ are the velocity and gradient vectors in Cartesian coordinates, respectively. In the q_{2D} formulation, ζ and M^4 approximate to the along-transect derivative of the cross-transect velocity v and the buoyancy. Therefore,

$$\zeta \approx v_x \quad \text{and} \quad M^2 \approx b_x \tag{4.6}$$

yield

$$q_{2D} = (\zeta + f)N^2 - v_z M^2 \, . \tag{4.7}$$

To minimize errors in this approximation, we sailed perpendicular to the Vitória-Trindade Ridge channels, where the BC and the IWBC flow through (see figure 4.1-A, where T1, T2, and T3 are perpendicular to the Besnard passage, the Main channel, and the Outer channel, respectively). This sampling strategy aimed to reduce the cross-transect gradients ∂_y compared with the along-transect gradients ∂_x. Nevertheless, the reader must be aware of the limitations of this approximation: ∂_y may be important in some parts of the transect, occasionally compensating or increasing the effects of ∂_x. A thorough analysis of these caveats is presented in Shcherbina et al. (2013).

We made our analysis hemisphere-independent by normalizing the potential vorticity. Multiplying (4.7) by $f/(f^2 N^2)$, unstable (or marginally stable) flow regions appear as low and negative PV. Figures 4.2-A, B and C show the instantaneous PV for the three transects of the cruise. For every transect, negative PV appears within the upper portion of the mixed layer, close to 20 m. Low PV patches also appear in all transects below 200 m, in regions of weak stratification. Aided by the increased horizontal resolution of the observations near the seamounts, we also find negative PV patches associated with flow close to topography. These regions are detailed in a blowout displayed in figures 4.2-D, E and F.

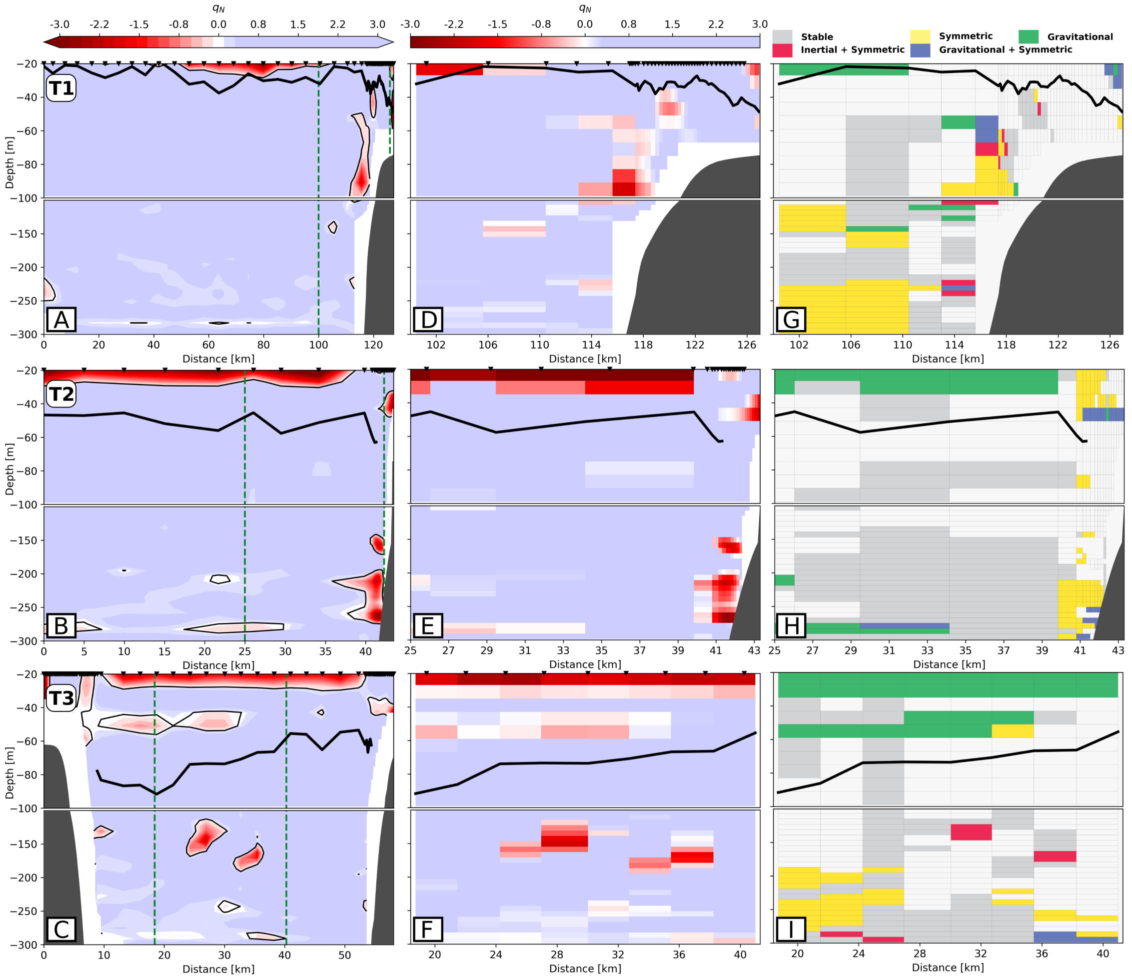

Figure 4.2: (A, B, and C): Potential vorticity under the $2D$ approximation for transects T1, T2, and T3. Stable q_{2D} regions are shaded in blue, while low and negative PV range from light blue to red. Green dashed lines delimits the blowout region shown in D, E, and F. (G, H and I): Instability types for the low PV regions in D, E, and F, following Thomas 2013's classification. The instability types are colored: green for gravitational, blue for gravitational plus symmetric, yellow for symmetric, red for symmetric plus inertial, and gray for stable low PV.

Figure 4.2-D zooms in on transect T1. Between about 40–100 m, an elongated patch of negative PV occurs where the lower portion of the BC rubs against the seamount (see figure 4.1-B). The negative PV patch in transect T2 (figure 4.2-E) is the deepest observed in the cruise, next to the seamount between about 150–250 m. The region is coincident with a reentrant flow of the IWBC into Tubarão Bight (see figure 4.1-C). Transect 3 in figure 4.2-F shows two negative PV patches in the channel comprised by two seamounts, associated with the anticyclonic portion of the structure observed between 20–30 km in figure 4.1-D. We classify the low PV patches based on the ϕ_{Ri_B} in (4.1), following Thomas et al. (2013), for the same blowout regions displayed in figures 4.2-D, E and F. We show our results based on the diagram proposed by these authors, hereafter the “Thomas’s diagram” (see figure 1 of Thomas et al., 2013). This classification was previously employed by Thompson et al. (2016) and Viglione et al. (2018) for glider observations, with horizontal resolution similar to ours.

Figures 4.2-G, H and I show the instability types observed in the Vitória-Trindade Ridge. In all three transects, we observe gravitationally unstable conditions widespread across the upper mixed layer. Such instability is associated with air-sea interactions, which are not extensively discussed in this work [for more information on submesoscale air-sea interactions, see e.g., Calil (2017), Ramachandran et al. (2018), and Wenegrat et al. (2018)]. Figure 4.2-G shows that, in T1, between 114 and 119 km from its start, symmetric instability and its hybrid forms dominate the unstable regions where the BC flows adjacent to topography. Conditions for symmetric instability also appear in the low PV region below 200 m, east of 110 km. Figure 4.2-H displays symmetric instability patches close to the topography in T2, where the IWBC reenters Tubarão Bight, between 40 and 43 km. Unstable conditions favoring symmetric instability also appear within the mixed layer. In T3, figure 4.2-I reveals the inertial-symmetric hybrid instability at 150 m depth, associated with the detached patches of negative PV flow (figure 4.1-D). We also observe a deeper symmetric instability patch in the 20–25 km portion of T3, part of the low PV band that extends from the westbound seamount up to 40 km (see figure 4.2-C).

From the *Ilhas* summer survey dataset, we observe several features, which hint at the BC and IWBC flows interacting with the Vitória-Trindade Ridge seamounts. At these sites, PV becomes negative and submesoscale instabilities may develop. Constantly slanted isopycnals close to seamounts give rise to symmetric instabilities, which prevail in the flow directly associated with topography; localized inertial instabilities appear in seemingly pinched-off structures generated by flow-topography interactions, as observed by D'Asaro (1988).

Next, we conduct a regional numerical experiment to further advance on the characterization of the submesoscale instabilities in the Vitória-Trindade Ridge region. In particular, we address the role of flow-topography interactions relatively to the snapshot obtained from the *Ilhas* summer cruise dataset.

3 Submesoscale permitting simulations

A full characterization of the Vitória-Trindade Ridge's submesoscale activity requires high resolution synoptic observations for different seasons, nonexistent in the region at present. Timeseries at selected locations along its nearly 1000 km extension would also be necessary. Therefore, we opt to use the Regional Oceanic Modeling System (ROMS; Shchepetkin and McWilliams, 2005), employing a nested approach.

The parent grid spans from 41°16′ S–62°34′ W to 10°01′ S–19°49′ W, with 6 km of horizontal resolution and 30 vertical levels in terrain-following coordinates. We employed temperature and salinity fields from the Simple Ocean Data Assimilation (SODA) project to initialize the simulation, forced by climatological monthly surface winds and heat fluxes from QuikSCAT and COADS, respectively. We run the simulation enforcing SODA fields as boundary conditions. This (parent) simulation was used in Napolitano et al. (2019), in which a thorough comparison of the model fields with observations of mesoscale features is presented.

The child grid resolution is 2 km, with 30 vertical levels in terrain-following coordinates, comprising the southeast Brazilian Margin ($30°00'$ S–$16°22'$ S, $50°16'$ W–$25°07'$ W). Wind forcing and heat fluxes are the same used in the parent simulation. To better resolve the complex topography of the Vitória-Trindade Ridge, the bathymetry resolution is about 4 km in the child grid, against 8 km of the parent grid. We used the last 5 years of the simulation in our analyses. In doing so, we interpolated the sigma-like vertical coordinates to standard depth levels, with resolution of 2 m between 0–20 m, 5 m between 20–100 m, and 10 m between 100–200 m. We emphasize that our goal in using the nested model is to obtain a submesoscale permitting simulation of the region, rather than a hindcast simulation of the observed transects.

As our quasi-synoptic observations, our model horizontal resolution of 2 km and time scale of a few hours capture only the larger scale end of the submesoscale, which may permit submesoscale features to develop—see discussion surrounding equations (4.3) and (4.4). We reinforce that the simulation cannot fully resolve symmetric instabilities, save only some modes of it, with lower growth rates (Bachman and Taylor, 2014). Moreover, with aspect ratio $>> 1$, we acknowledge that gravitational instability also cannot be resolved: instead, the model allows convective adjustment. The term “gravitational instability" will thus refer to the model acting to restratify regions of $N^2 < 0$, using a KPP parametrization for vertical mixing.

The model resolution issue might account for an underestimation of the amount of unstable flow and the development of different types of instabilities. Idealized large eddy simulations (e.g., Thomas et al., 2013; Stamper and Taylor, 2017) and other submesoscale-modeling efforts (with horizontal grid resolution of hundreds of meters, e.g., Gula et al., 2016; McWilliams et al., 2019), have highlighted some limitations of coarser simulations such as our 2-km ROMS. On the other hand, a fully submesoscale-resolving resolution is prohibitive in a domain large enough to resolve the mesoscale western boundary currents, such as the BC and the IWBC. This stalemate will persist until computational resources allow large domains to be accommodated with the grid aspect ratio of unity.

Evaluation of the submesoscale dynamics in ROMS at 2 km resolution

To investigate the development of submesoscale in our numerical simulation outputs, we use the full horizontal gradients of velocity and buoyancy. The diagnostics of submesoscale flows implies order $\mathcal{O}(1)$ rates of the nondimensional variables

$$\text{VORTICITY} \overset{\text{def}}{=} \frac{\zeta}{|f|} = \frac{v_x - u_y}{|f|}\,, \tag{4.8}$$

$$\text{STRAIN} \overset{\text{def}}{=} \frac{\alpha}{|f|} = \frac{[(u_x - v_y)^2 + (v_x + u_y)^2]^{1/2}}{|f|}\,, \tag{4.9}$$

$$\text{DIVERGENCE} \overset{\text{def}}{=} \frac{\delta}{|f|} = \frac{u_x + v_y}{|f|}\,, \text{ and} \tag{4.10}$$

$$\text{GRADB} \overset{\text{def}}{=} \frac{M^2}{f^2} = \frac{|\nabla_h b|}{f^2}\,, \tag{4.11}$$

with (4.8), (4.9), and (4.10) usually associated with large lateral buoyancy gradients (4.11). Detailed diagnostics for submesoscale flows can be found in, e.g., Mahadevan and Tandon (2006), Capet et al. (2007), Thomas et al. (2008), Shcherbina et al. (2013), and Johnson et al. (2020).

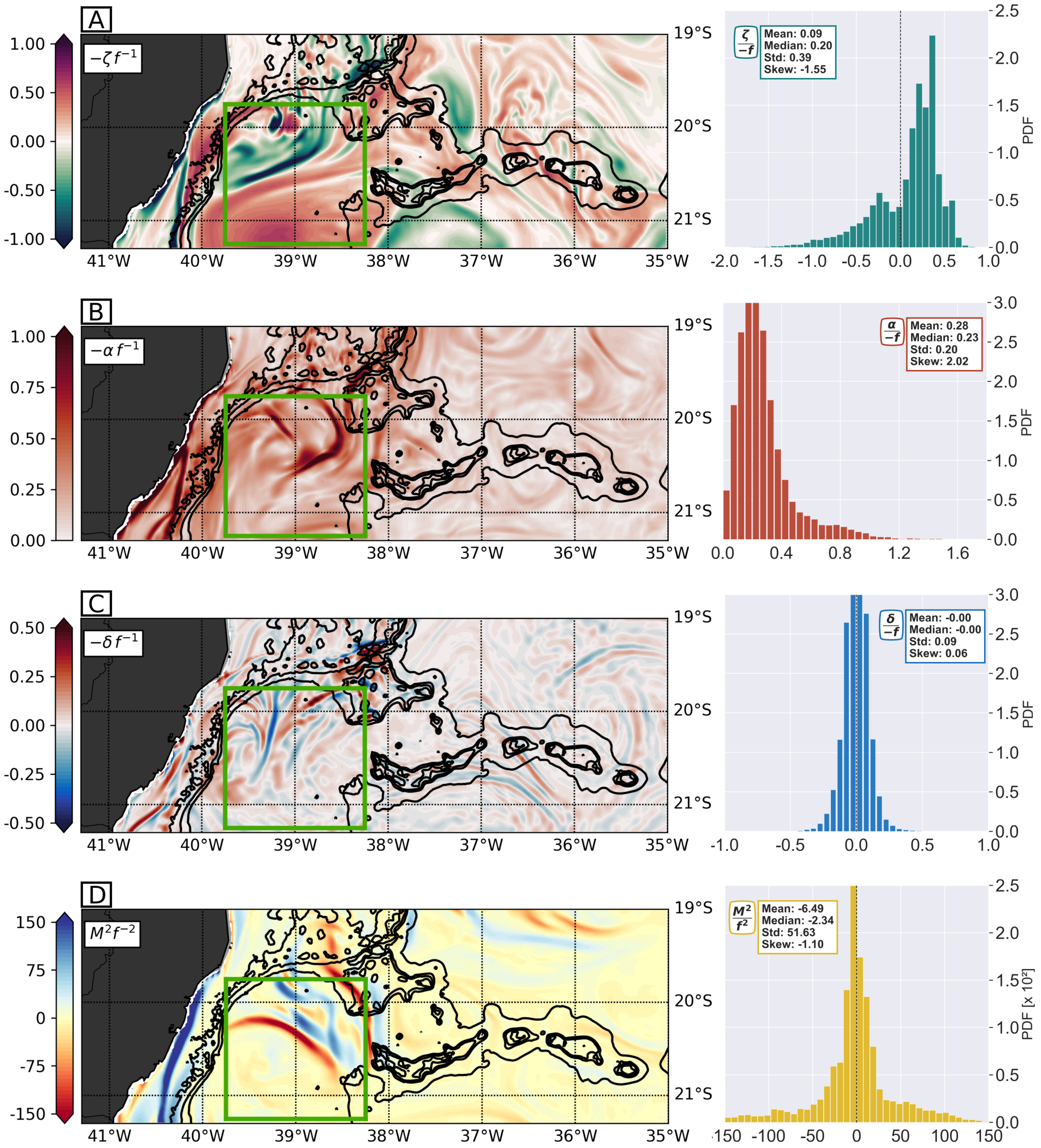

Figure 4.3: Snapshots and probability density functions (PDFs) of the 2-km ROMS simulation at the surface, showing rates of (A) relative vorticity $-\zeta/f$, (B) strain $-\alpha/f$, (C) divergence $-\delta/f$, and (D) lateral buoyancy gradient M^2/f^2. The PDFs are computed within the green box showed in the snapshots.

Figure 4.3 (left panels) display snapshots of VORTICITY, STRAIN, DIVERGENCE, and GRADB obtained from the 2-km ROMS simulation. We also computed the probability density function (PDF; see figure 4.3, right panels) of the aforementioned rates within

Tubarão Bight (the green square in the snapshots), following Shcherbina et al. (2013). We selected different days for each rate—which show the development of submesoscale-like features embedded in the mesoscale flow—and the corresponding PDFs, which present typical characteristics of submesoscale activity.

Figure 4.3-A shows the PDF of VORTICITY. It presents large asymmetry, with a long tail toward cyclonic motions and skewness of -1.55, which agrees with results by, e.g., Rudnick (2001), Calil and Richards (2010), Shcherbina et al. (2013), and Molemaker et al. (2015). The anticyclonic side of the VORTICITY PDF is restricted to order $\mathcal{O}(1)$ values, another signature of submesoscale activity (Mahadevan and Tandon, 2006).

The PDF of STRAIN in figure 4.3-B follows a χ^2 distribution, with mean 0.28 and skew 2.02. A tail of sporadic high STRAIN reveals extrema which are six times larger than the mean. Values of strain rate up to 2 are also reported by Rocha et al. (2016b) in daily-averaged model outputs, and by Johnson et al. (2020)'s observations. A skewed distribution is presented by Shcherbina et al. (2013) and Rocha et al. (2016b). In the ocean, such high strain rates intensify lateral buoyancy gradients, leading to frontogenesis and larger vertical velocities (Mahadevan and Tandon, 2006).

Divergence rates in the PDF of figure 4.3-C reveals order $\mathcal{O}(1)$ values, with a slightly skewed distribution toward convergence. This asymmetry is typical of submesoscale, associated with frontal sharpening and downwelling (McWilliams et al., 2009). Our PDF distribution is consistent with model results by Pérez and Calil (2017) for the Equatorial Atlantic, and observations reported by Johnson et al. (2020) off the California coast. A high-resolution theoretical simulation by McWilliams et al. (2019) shows order $\mathcal{O}(1)$ DIVERGENCE accompanying a mesoscale meander, associated with large vertical velocities [$\mathcal{O}(10^{-3})\,\mathrm{m\,s^{-1}}$]. However, our simulation results differ from the North

Atlantic, open ocean, winter observations of Shcherbina et al. (2013), who found larger values ($\sim$1.5) and a more skewed distribution (0.20).

In figure 4.3-D, the PDF of GRADB shows a nearly symmetric distribution, with large standard deviation of 51.63. We observe that strong fronts of buoyancy, with magnitude $4\times10^{-7}\text{s}^{-2}$, are responsible for these large deviations. In a review of submesoscale processes, Mahadevan (2016) points that lateral buoyancy gradients of 10^{-7}s^{-2} yields horizontal length scales of 1 km. Submesoscale idealized simulations by Thomas et al. (2016), and Wenegrat et al. (2018) use buoyancy gradients at fronts to about $5\times10^{-7}\text{s}^{-2}$. Strong fronts observed by Johnson et al. (2020) reveal high GRADB of about 200. A higher-resolution model of a Gulf Stream meander, presented by McWilliams et al. (2019), shows lateral buoyancy gradients of about 10^{-6}s^{-2}, therefore, half order of magnitude larger than our 2-km ROMS values.

The rates presented in figure 4.3 show that these model values are consistent with other numerical studies and recent observations, and adequate to characterize submesoscale phenomena. We observe weaker magnitude and substantial intermittency of the submesoscale motions throughout the model timeseries. The intermittent character of these motions seems intrinsic to how submesoscale manifest in the ocean (Capet et al., 2007).

Seasonal characterization

Traditionally, seasonality in submesoscale flows has been related to the mixed layer seasonal cycle. A deep, energetic mixed layer in winter presents more submesoscale activity than that of a shallow and stratified summer mixed layer (e.g., Mensa et al., 2013; Sasaki et al., 2014; Callies et al., 2015; Calil, 2017). In the Gulf Stream region, Mensa et al. (2013) showed a clear seasonal cycle in submesoscale comparing two numerical simulations of different horizontal resolutions. Later, Callies et al. (2015) confirmed this seasonality, reporting observations in winter and summertime. High-resolution numerical simulations have all but confirmed the enhanced submesoscale activity in the wintertime in the open ocean, primarily due to buoyancy loss and increased winds over frontal regions (Sasaki et al., 2014; Calil, 2017).

To assess the submesoscale seasonality in the BC-IWBC domain of our simulation, first we extract the blowout regions of the observed transects (T1, T2, and T3) from the model outputs (see figure 4.2-D, E, and F); second, we calculate the Ertel potential vorticity (4.5) for the upper 200 m of the water column. The percentage of unstable points (grid points with $PV<0$, not shown) in T3, the less influenced by the BC and topography, follows the typical mixed layer seasonal cycle. On average, 3% of T3 is unstable in summer, increasing in fall to about 8%. This percentage peaks in winter and spring, representing 17 and 19% of the transect, respectively. Our results are consistent with recent studies of submesoscale seasonality in the Kuroshio Extension, which report early-spring peaks (cf. Rocha et al., 2016b; Sasaki et al., 2017). T2 shows a slight increase in the percentage of unstable flow in summer(fall) from 3(8) to 6%(11%). But the mixed layer seasonal cycle still dominates the distribution of unstable points in the transect, with higher values in winter (16%) and spring (18%).

In T1, however, the occurrence of unstable flow diverges from the seasonal patterns of T2 and T3. This is the region where the BC flow strikes off through the seamounts (see observations in figure 4.1 and model snapshots in figure 4.3). The percentage of unstable flow cycles from 10 to 7% from summer to fall, as well as from winter to spring.

This suggests that the interaction between the western boundary currents and the topography generates unstable flow throughout the year.

Flow-topography interactions

Vertical fluxes of buoyancy are telltale of an ongoing instability process. Anomalies from a mean vertical buoyancy flux $\overline{wb'} < 0$ indicate that a water parcel is displaced from its average, stable depth. These unstable conditions lead to instabilities (or equivalent model responses) that act to restratify the water column, which in turn yield $\overline{wb'} > 0$. This destabilization–restratification cycle is recurrent throughout the model timeseries. Here, we define a buoyancy flux anomaly as the deviation from a slowly-varying vertical buoyancy flux, through the decomposition of the model outputs:

$$wb = \overline{wb} + wb' \, . \tag{4.12}$$

The daily term wb' in (4.12), associated with submesoscale, is the deviation from a low-pass filtered mean $(\bar{\cdot})$ of 3 days, equivalent to two times the inertial period. We then define an even slower varying submesoscale buoyancy flux (SBF) $\overline{w\prime b\prime}$ of 6 days, which corresponds approximately to a full destabilization–restratification cycle.

Figure 4.4 explores the spatio-temporal variability of the SBF in the model. Figures 4.4-A, B, and C show the time evolution of the along-transect averaged SBF for T1, T2, and T3, respectively. Also, they show the tendency of the MLD and the isopycnal ρ =1025.9 $\mathrm{kg\,m^{-3}}$ (hereafter 25.9), which marks the interface between the warmer surface waters and the colder, nutrient-rich waters occupying the pycnocline (cf. Lazaneo et al., 2020). From the full model timeseries, we observe that all transects show a mixed layer seasonal cycle. Nevertheless, this cycle is much more pronounced in T3 than in T1 or T2. Given the proximity between the transects, this difference can only be attributed to the presence of the BC in T1 and T2. This weakened seasonal effect appears to be related to the BC baroclinic geostrophic adjustment, which lifts the pycnocline (e.g., Calado et al., 2010), with upper-pycnocline waters observed at 150 m within Tubarão Bight (e.g., Costa et al., 2017).

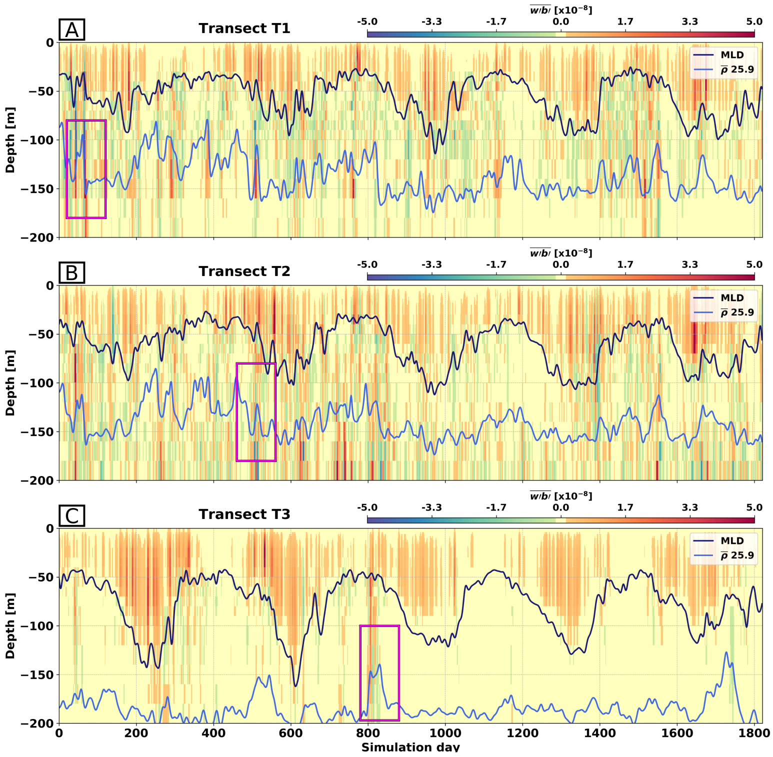

Figure 4.4: Model timeseries of the along-transect averaged SBF ($\overline{w'b'}$) for T1 (A), T2 (B), and T3 (C). The dark blue line represents the MLD, and the light blue line represents the $\overline{\rho} = 1025.9\,\mathrm{kg\,m^{-3}}$ isopycnal. The magenta boxes indicate periods of strong SBF events affecting $\overline{\rho}$.

Figures 4.4-A, B, and C show strong positive SBF associated with the thickness of the mixed (convective) layer (Taylor and Ferrari, 2010) and consistent with Thomas et al. (e.g., 2016). Below the MLD, patterns of SBF greatly differ. In transect T1, instabilities also develop between the MLD and the 25.9 isopycnal, with stronger SBF around 150 m. Even deeper unstable conditions are observed in transect T2, where the strongest SBF occurs below the 25.9 isopycnal (figure 4.4-B). In transect T3, however, unstable conditions develop almost solely within the mixed layer (figure 4.4-C).

As a consequence of the destabilization–restratification process, the submesoscale vertical fluxes move isopycnals up and down the water column. Left panels of figure 4.5 detail periods of strong SBF noted in figure 4.4, and the resulting vertical displacements of the 25.9 isopycnal. Additionally, snapshots of each transect when SBF is strongest show the spatial distribution of the instabilities.

Figures 4.5-A, B, and C compares the 25.9 isopycnal to a mean (6 days averaged) isopycnal $\overline{\rho}$ =25.9 kg m^{-3}. The time-mean $\overline{\rho}$ averages out the effects of submesoscale destabilization and restratification, dampening the variations in the 25.9 isopycnal. Therefore, while crossing regions of strong SBF, the curves instantly diverge. To track the daily changes in the depth of the 25.9 isopycnal, we simply subtract it from the depth of the mean isopycnal. Due to vertical motions induced by submesoscale processes, in our simulation the difference $z - \overline{z}$ reaches about 20 m day^{-1}, fluctuating ~0.04 kg m^{-3} around the mean isopycnal. Close to this depth range, Legal et al. (2007) obtained similar values for 0.05 kg m^{-3} density anomalies within elongated, filament-like structures. Also in a frontal region, Martin et al. (2001) showed that strong vertical velocities of $\mathcal{O}(10)$ m day^{-1}, associated with ageostrophic secondary circulations, drive productivity blooms in oligotrophic regions, as nutrients and organisms are exposed to increasing light levels. Downward variations are also important, leading to submesoscale subduction, potentially enhancing the carbon sink through slanted isopycnals (Omand et al., 2015; Mahadevan, 2016).

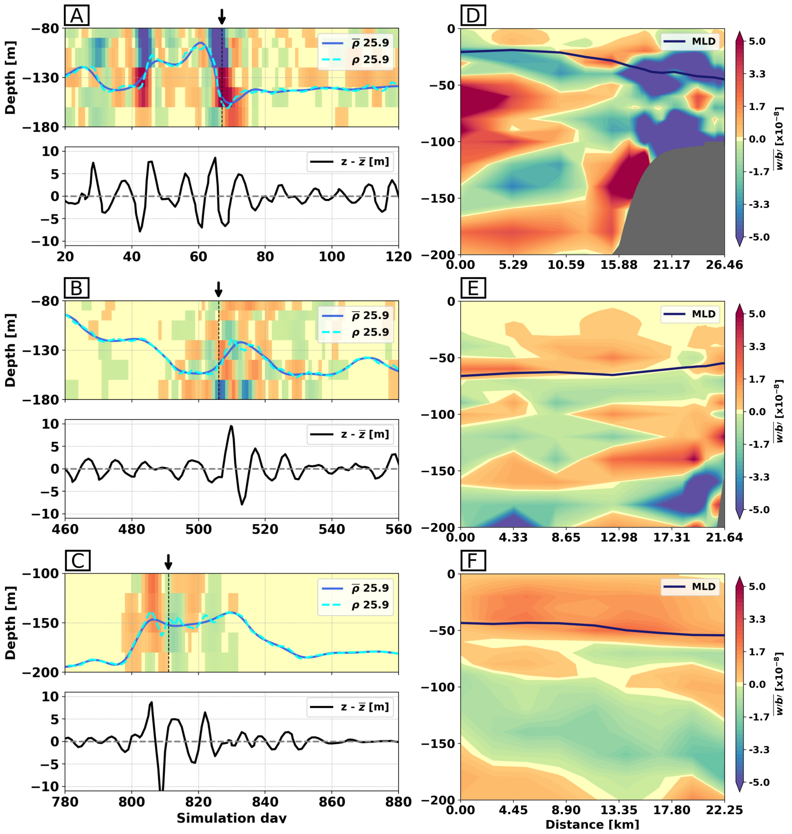

Figure 4.5: Blowout of strong SBF events within the model timeseries for transects T1 (A), T2 (B), and T3 (C). The cyan line represents the $\rho = 1025.9\,\mathrm{kg\,m^{-3}}$ isopycnal. The blue line represents the 6-day mean $\overline{\rho} = 1025.9\,\mathrm{kg\,m^{-3}}$ isopycnal. The black line in the lower panels represents the depth difference between the isopycnal ρ and the mean isopycnal $\overline{\rho}$. The arrow and dashed line indicate the day of simulation in the three snapshots on the right, on which the spatial distribution of the submesoscale buoyancy flux is shown: day 67 for T1 (D), day 506 for T2 (E), and day 811 for T3 (F).

The vertical sections associated with the strongest SBF (figures 4.5-D, E, and F) show that SBF peaks near topographic features. The intermittent peaks in the T1 timeseries (figure 4.4-A) clearly coincide with the depth range where the flow rubs against topography in figure 4.5-D. A similar pattern is seen in T2 (see the high SBF in the lower right of figure 4.5-E). The flow in T3, which is more akin to an open ocean condition—as there is no direct interaction with the topography—has a more homogeneous distribution, showing no distinct peak in figure 4.5-F.

At the Vitória-Trindade Ridge region, flow-topography interactions are likely to play a major role in generating submesoscale instabilities. Such interactions drive rapid changes in the depth of isopycnals, and are thus key to primary production and carbon export, as it lifts and subducts particles and organisms (Mahadevan, 2016). To further investigate the effects of the BC interacting with topography, we evaluate the unstable, PV< 0 flow throughout the model timeseries. At each transect, we calculate the $\tan(\phi_{Rib}) = -Ri_B^{-1}$ angle presented in (4.1) to classify, considering the model limitations, the regions and seasons prone to different instabilities, analogously to what we performed in section 2 for the observations.

Instability types

Along with the percentage of negative PV, instability types may change seasonally. In general, stable conditions in summer develops into unstable stratification in fall; a deeper mixed layer in winter, and restratification in early spring, favor symmetric instability (e.g., Thompson et al., 2016). Also, spatial heterogeneity can result in abrupt changes in the submesoscale instability types (e.g., Viglione et al., 2018). As already discussed above, both temporal and spatial variability of the flow across the Vitória-Trindade Ridge, i.e. the mixed layer seasonal cycle and the interaction between the BC and the seamounts, are likely to play a role in determining the types of instability.

In figure 4.6, we adapted the Thomas's diagrams to display not only the type of instability which the flow develops (shown azimuthally), but also the depth at which these instabilities occur (shown radially). The schematic diagram in the upper left of figure 4.6 shows the instability types related to the angle ϕ_{Ri_B}. To build the seasonal diagrams, we first computed the total amount of unstable flow at each grid point for T1, T2, and T3 for every season of the ROMS timeseries. Second, we classified the instabilities following Thomas et al. (2013), with their percentage displayed in the corresponding diagram slices.

Colors show the PDF of ϕ_{Ri_B}, normalized at every depth by the maximum PDF value. This normalization excludes the stable low PV region.

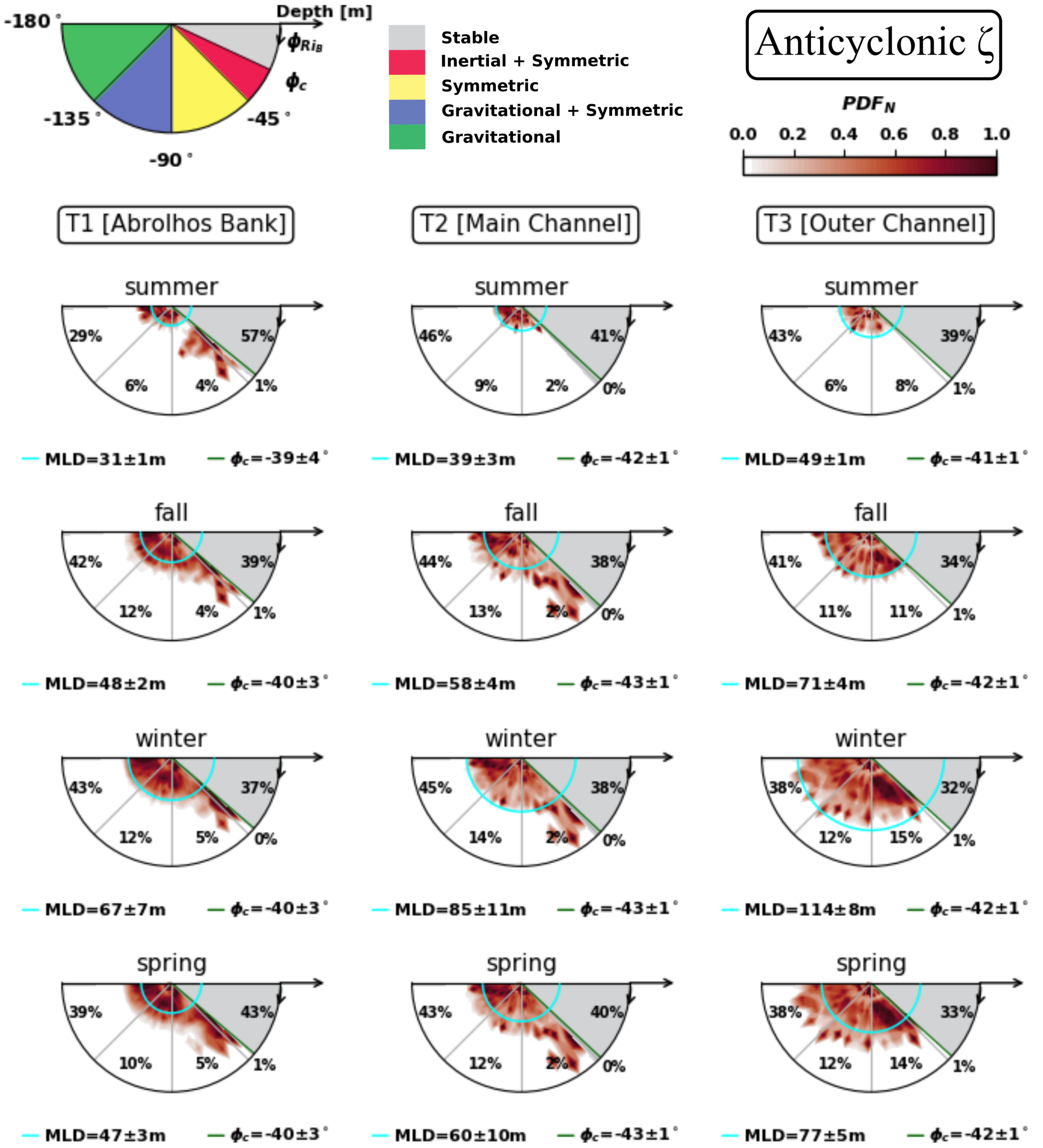

Figure 4.6: The adapted Thomas's diagrams for the classification of the instabilities for flow with *anticyclonic vorticity*, by type and depth, for transects T1, T2, and T3 of the ROMS simulation. The azimuth ϕ_{Ri_B} denotes the instability type, while the radial distance indicates the depth in which each instability type is identified. For every season, the slices of the diagram contain the average percentage of their corresponding instability type. Colors show the PDF of ϕ_{Ri_B}, normalized at every depth by the maximum PDF value, not considering the gray-shaded, stable low PV. For better visualization, the depth axis is restricted to 170 m. The cyan line represents the mean mixed layer depth for the season. The green lines delimit the region between -45° and the critical angle ϕ_c.

Figure 4.6 presents the Thomas's diagrams for flow with anticyclonic vorticity on T1, T2, and T3. As previously discussed, T3 (at the Outer channel) presents the deepest mixed layer in all seasons and undergoes a standard seasonal evolution, with higher submesoscale activity in winter and spring. Gravitational instability represents about 40% of the negative PV throughout 5 years of simulation. Modes of symmetric instabilities and its hybrid forms (symmetric-gravitational and symmetric-inertial) increase as the mixed layer deepens, responding for about 30% of the instabilities in winter and spring. Symmetric instabilities in T3 seldom occur below the MLD.

The percentage of unstable flow in T1 south of Abrolhos Bank does not follow the seasonal cycle of the MLD. But a portion of the 57% stable PV<0 in summer is classified as gravitationally unstable in fall (an increase from 29 to 42%), typical of the erosion process of the mixed layer. Thus, other types of instabilities drive the changes in the amount of negative PV in this transect, which do not follow the standard mixed-layer cycle. As in T3, mixed gravitational-symmetric instabilities are about 12% from fall to spring. The resolved modes of symmetric and symmetric-inertial instabilities represent 5% of the unstable flow independently of season. These instabilities generally peak below the MLD, dominating the unstable flow below 100 m.

We discuss T2 last, as it presents characteristics in between T3 and T1. In the Main channel, T2 shows a distribution of instabilities comparable to T3 in summer, with instabilities restricted to the mixed layer. Here, the percentage of gravitational instability also remains nearly constant throughout the year, accounting for about 45% of the negative PV. But from fall to spring, the T2 diagrams present a pattern similar to that of T1. Symmetric instabilities represent only 2% of the unstable flow, but occur mostly below the MLD. The observations depict symmetric instability developing from the interaction of the IWBC and a seamount; in ROMS, a smoothened topography and deeper IWBC may result in deeper instabilities, not fully captured by our 200-m depth transect. We observe no inertial instabilities in T2.

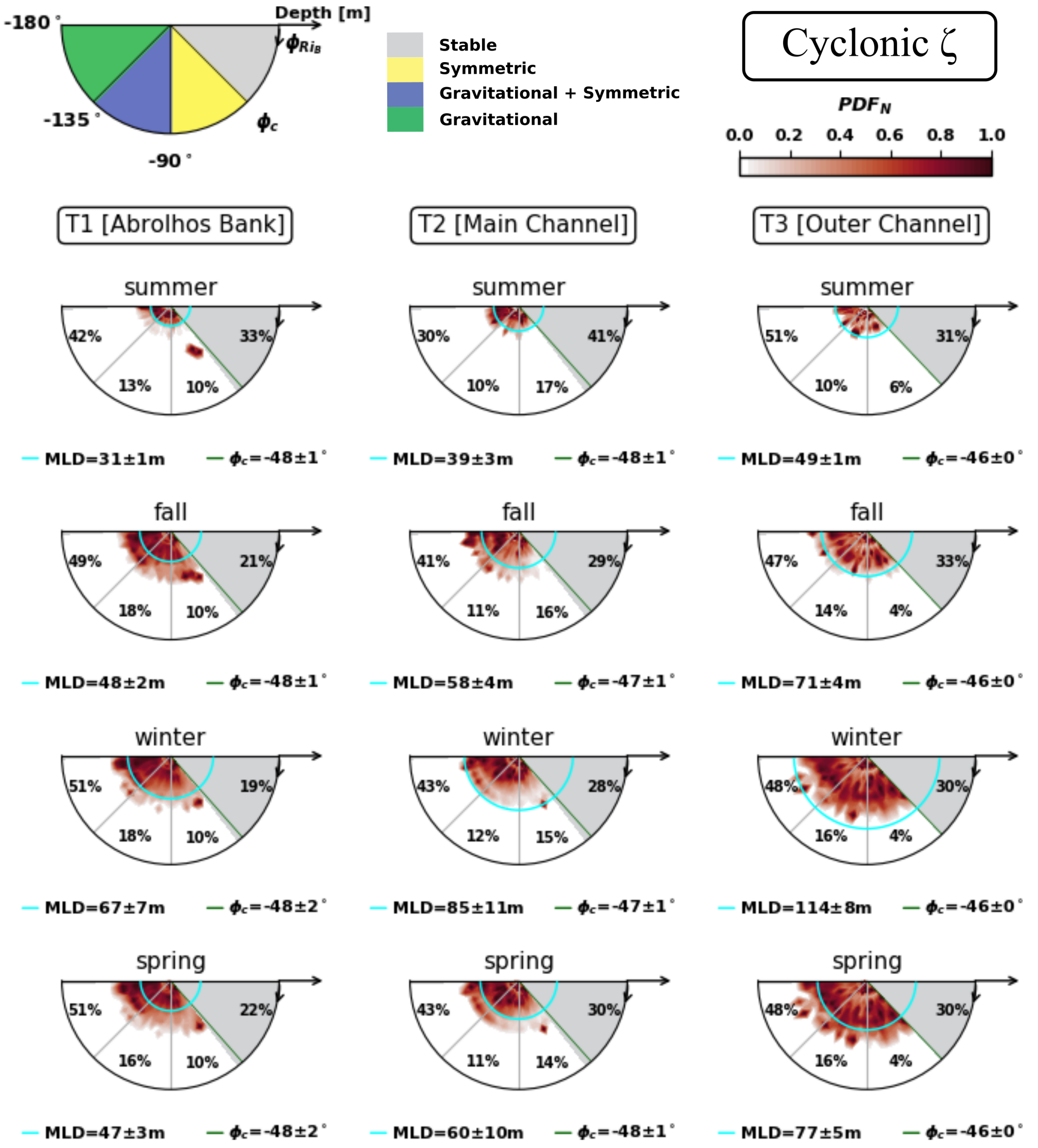

Figure 4.7: The adapted Thomas's diagrams for the classification of the instabilities for flow with *cyclonic vorticity*, by type and depth, for transects T1, T2, and T3 of the ROMS simulation. The azimuth ϕ_{Ri_B} denotes the instability type, while the radial distance indicates the depth in which each instability type is identified. For every season, the slices of the diagram contain the average percentage of their corresponding instability type. Colors show the PDF of ϕ_{Ri_B}, normalized at every depth by the maximum PDF value, not considering the gray-shaded, stable low PV. For better visualization, the depth axis is restricted to 170 m. The cyan line represents the mean mixed layer depth for the season. The green lines delimit the region between -90° and the critical angle ϕ_c.

The transition of the instability types occurring below the MLD seen from T3 to T1 follows the influence of topography. Although we do not observe an abrupt transition in the types of instabilities as those in Viglione et al. (2018), instabilities due to flow-topography interactions represent nearly all deep symmetric instabilities. Some of these occur in isolated patches, much deeper than the MLD. Even with coarse resolution and only partially resolving submesoscale instabilities, our simulation shows the importance of flow-topography interactions in generating such instability modes.

Flow with cyclonic vorticity presents a similar pattern for the three transects (figure 4.7). As in T3 for anticyclonic vorticity, instabilities occur mostly within the mixed layer. When compared to anticyclonic-vorticity diagrams, the percentage of stable PV< 0 decreases about 10%. Curiously, symmetric instability (plus its hybrids) present an opposite pattern: in T1 and T2, they represent about 30% of the unstable flow, whereas in T3 they account for about 4%. Cyclonic-vorticity flow instabilities seldom occur below the mixed layer, except for small patches of symmetric instabilities in T1.

4 Final remarks

The Vitória-Trindade Ridge region plays an important role in the dynamics of the western boundary current system off Eastern Brazil. Costa et al. (2017) showed that the IWBC crosses the Vitória-Trindade Ridge forming a quasi-stationary recirculation, which occupies Tubarão Bight at intermediate levels. The interaction of the jet, the recirculation and westward-propagating nonlinear waves cause advection and downstream perturbation growth, as they negotiate the Main and Outer channels (Napolitano et al., 2019). In the upper layers, the Brazil Current crosses the Vitória-Trindade Ridge forming a large cyclonic loop, occasionally forming the Vitória Eddy (Schmid et al., 1995), and reattaches to the continental margin south of 21 °S (Lazaneo et al., 2020). Hence, the mesoscale activity of the western boundary currents are already setup in that study, but not the submesoscale phenomena associated with those. This study aims to present a first glimpse of the submesoscale dynamics set off by these currents as they cross the Vitória-Trindade Ridge, or in other words, their interaction with the topography of the ridge's seamounts.

Three transects of shipboard-ADCP velocity and underway-CTD derived density in the region captures the first submesoscale features ever observed at the Vitória-Trindade Ridge region, associated with the Brazil Current and the Intermediate Western Boundary Current negotiating the ridge's complex topography. We analyzed low potential vorticity patches in the transects, each one presenting a different level of interaction between the flow and topography. While gravitational instabilities dominate the negative PV close to the base of the mixed layer, symmetric and the hybrids symmetric-gravitational and symmetric-inertial instabilities appear at unstable regions where the western boundary currents rub against the seamounts. Moreover, inertial instabilities dominate observed submesoscale eddies, which are likely formed due to topographic steering of the flow.

Using a submesoscale-motion permitting regional numerical simulation, we show that seasonal variations are important in the generation of negative PV at the Vitória-Trindade Ridge. But spatial differences, characterized by the presence of topography, imposes important changes in the seasonality of the modeled transects. Away from topography, transect T3 exhibits a typical seasonal cycle of submesoscale, with instabilities developing within the mixed layer. Transect T2 reveals deep symmetric instabilities ($>$150 m) developing below the mixed layer, with intermittent peaks close to 200-m depth, where the flow encounters topography. Symmetric instabilities frequently occur below the mixed-layer in transect T1, where a prominent seamount constantly interacts with the Brazil Current. There, flow-topography interactions mask the seasonality of submesoscale dynamics, showing no clear cycle in the amount of unstable flow throughout the years.

In the Vitória-Trindade Ridge region, topographically-driven instabilities appear as an important mechanism that displaces pycnocline isopycnals several meters. These upwelled isopycnals expose nutrient-rich waters to different sunlight, and may boost primary productivity below the mixed layer. As a counterpart effect, subducted isopycnals may fuel the carbon pump, driving particles and organisms away from sunlit regions.

Finer-resolution simulations than the 2 km grid employed in this work are already under development for the region. However, the lack of observations still remains as the main obstacle to better understand the submesoscale processes linked to the BC-IWBC system and the Vitória-Trindade Ridge, and how they change the dynamics up and downstream the ridge.

Acknowledgments

Dante Napolitano was financed in part by Coordenação de Aperfeiçoamento de Pessoal de Nível Superior—CAPES, Brazil—Finance Code 001 and by Projeto Santos (Petrobras 3368). This study is supported by Projeto REMARSUL (Processo CAPES 88882.158621/2014-01), Projeto VT-Dyn (Processo FAPESP 2015/21729-4) and Projeto SUBMESO (Processo CNPq 442926/2015-4).

CHAPTER 5.

FINAL REMARKS

This dissertation investigates the meso and submesoscale dynamics of the Brazil Current and the Intermediate Western Boundary Current at the Vitória-Trindade Ridge region. The IWBC, which flows equatorward, interacts with the ridge's topography, recirculating within Tubarão Bight. This recirculation is topographycally forced to quasi-steadiness, yet nonlocal, westward-propagating eddies interact with the flow. Swept away from Tubarão Bight by the IWBC, these advected eddies most likely interact with the seamounts. The perturbations experience explosive growth downstream of the ridge, by feeding off the mean flow through horizontal shear production.

Within Tubarão Bight, the poleward-flowing BC meanders cyclonically, occasionally forming the Vitória Eddy. In simple theoretical simulations, a quasi-steady IWBC recirculation may be strong enough to steer the BC within Tubarão Bight, triggering the formation of the Vitória Eddy. The steady IWBC recirculation acts as a topographic bump for the upper-layer flow. During the Vitória Eddy formation, a weak upper-layer jet rapidly veers toward the boundary, and flows attached to it in a local steady state. On the other hand, in cases of a too-strong jet, perturbations are swept off the lower-layer eddy domain, triggering downstream meander growth; no eddy is formed within Tubarão Bight. The dynamics leading to eddy formation in the upper-layer are both linear and nonlinear, and intimately related to the ratio between the velocity in the upper and lower layers.

Associated with the mesoscale mean flow, submesoscale phenomena develop within the BC and the IWBC as they cross the Vitória-Trindade Ridge. An original dataset in the region shows uncommon submesoscale-like structures below the mixed layer depth. These structures are generally associated with the western boundary currents interacting with topography. A seasonal characterization of the flow from a regional numerical simulation shows that, away from topography, submesoscale activity undergoes a typical seasonal cycle, with peaks in winter and early-spring. But flow-topography interactions affect this pattern, suggesting that such interactions generate unstable flow throughout the year. Within these regions, symmetric instability accounts for nearly all the deeper patches of unstable flow.

Future work

This dissertation presents a glimpse of an ongoing effort to understand the complex meso and submesoscale dynamics of the western boundary currents within the Vitória-Trindade Ridge region. Toward the future, the constantly-improving numerical models will continue to play a major role in our research. Nevertheless, direct observations are inestimable, and the paucity of such still represents a major obstacle to study the region. Following this study, future work will aim to investigate the role of topography in the energy conversions within the IWBC; as for the Vitória Eddy formation, a hierarchy of models may further address the mechanisms that drive such process. At the submesoscale, future work will address the biological implications of generated instabilities by flow-topography interactions.

Bibliography

Andres, M., 2016: On the recent destabilization of the Gulf Stream path downstream of Cape Hatteras. *Geophysical Research Letters*, **43 (18)**, 9836–9842, doi: 10.1002/2016GL069966.

Arruda, W. Z., E. J. D. Campos, V. Zharkov, R. G. Soutelino, and I. C. A. Silveira, 2013: Events of equatorward translation of the Vitoria Eddy. *Continental Shelf Research*, **70**, 61 – 73, doi: https://doi.org/10.1016/j.csr.2013.05.004, URL http://www.sciencedirect.com/science/article/pii/S0278434313001519, oceanography, ecology and management of Abrolhos Bank.

Arruda, W. Z., and I. C. A. Silveira, 2019: Dipole-induced Central Water extrusions south of Abrolhos Bank (Brazil, 20.5S). *Continental Shelf Research*, 103976, doi: doi.org/10.1016/j.csr.2019.103976.

Bachman, S. D., B. Fox-Kemper, J. R. Taylor, and L. N. Thomas, 2017: Parameterization of frontal symmetric instabilities. I: Theory for resolved fronts. *Ocean Modelling*, **109**, 72–95.

Bachman, S. D., and J. R. Taylor, 2014: Modelling of partially-resolved oceanic symmetric instability. *Ocean Modelling*, **82**, 15–27.

Biló, T. C., I. C. A. Silveira, W. C. Belo, B. M. Castro, and A. R. Piola, 2014: Methods for estimating the velocities of the Brazil Current in the pre-salt reservoir area off southeast Brazil (23 S–26 S). *Ocean Dynamics*, **64 (10)**, 1431–1446, doi: 10.1007/s10236-014-0761-2.

Blumen, W., 1968: On the stability of quasi-geostrophic flow. *Journal of the Atmospheric Sciences*, **25 (5)**, 929–931.

Boccaletti, G., R. Ferrari, and B. Fox-Kemper, 2007: Mixed layer instabilities and restratification. *Journal of Physical Oceanography*, **37 (9)**, 2228–2250, doi: 10.1175/JPO3101.1.

Boebel, O., R. Davis, M. Ollitrault, R. Peterson, P. Richardson, C. Schmid, and W. Zenk, 1999: The intermediate depth circulation of the western South Atlantic. *Geophysical Research Letters*, **26 (21)**, 3329–3332.

Boebel, O., C. Schmid, and W. Zenk, 1997: Flow and recirculation of Antarctic Intermediate Water across the Rio Grande rise. *Journal of Geophysical Research: Oceans*, **102 (C9)**, 20 967–20 986.

Bretherton, F. P., and D. B. Haidvogel, 1976: Two-dimensional turbulence above topography. *Journal of Fluid Mechanics*, **78 (1)**, 129–154.

Burns, K. J., G. M. Vasil, J. S. Oishi, D. Lecoanet, and B. P. Brown, 2019: Dedalus: A Flexible Framework for Numerical Simulations with Spectral Methods. *arXiv e-prints*, arXiv:1905.10388, 1905.10388.

Calado, L., I. Da Silveira, A. Gangopadhyay, and B. De Castro, 2010: Eddy-induced upwelling off cape são tomé (22 s, brazil). *Continental Shelf Research*, **30 (10-11)**, 1181–1188.

Calil, P. H., 2017: Wind-induced subduction at the south atlantic subtropical front. *Ocean Dynamics*, **67 (10)**, 1351–1365, doi: doi.org/10.1007/s10236-017-1090-z.

Calil, P. H. R., and K. J. Richards, 2010: Transient upwelling hot spots in the oligotrophic North Pacific. *Journal of Geophysical Research: Oceans*, **115 (C2)**.

Callies, J., R. Ferrari, J. M. Klymak, and J. Gula, 2015: Seasonality in submesoscale turbulence. *Nature communications*, **6 (1)**, 1–8.

Campos, E. J., 2006: Equatorward translation of the Vitória Eddy in a numerical simulation. *Geophysical Research Letters*, **33 (22)**, doi: 10.1029/2006GL026997.

Capet, X., J. C. McWilliams, M. J. Molemaker, and A. F. Shchepetkin, 2007: Mesoscale to Submesoscale Transition in the California Current System. Part I: Flow Structure, Eddy Flux, and Observational Tests. *Journal of Physical Oceanography*, **38 (1)**, 29–43, doi: 10.1175/2007JPO3671.1.

Capet, X., J. C. McWilliams, M. J. Molemaker, and A. F. Shchepetkin, 2008: Mesoscale to submesoscale transition in the california current system. part iii: Energy balance and flux. *Journal of Physical Oceanography*, **38 (10)**, 2256–2269, doi: 10.1175/2008JPO3810.1.

Chelton, D. B., M. G. Schlax, and R. M. Samelson, 2011: Global observations of non-linear mesoscale eddies. *Progress in Oceanography*, **91 (2)**, 167–216, doi: 10.1016/j.pocean.2011.01.002.

Chen, R., G. R. Flierl, and C. Wunsch, 2014: A description of local and nonlocal eddy–mean flow interaction in a global eddy-permitting state estimate. *Journal of Physical Oceanography*, **44 (9)**, 2336–2352, doi: 10.1175/JPO-D-14-0009.1.

Costa, V. S., G. N. Mill, M. Gabioux, G. S. Grossmann-Matheson, and A. M. Paiva, 2017: The recirculation of the intermediate western boundary current at the Tubarão Bight–

Brazil. *Deep Sea Research Part I: Oceanographic Research Papers*, **120**, 48–60, doi: 10.1016/j.dsr.2016.12.001.

D'Asaro, E. A., 1988: Generation of submesoscale vortices: A new mechanism. *Journal of Geophysical Research: Oceans*, **93 (C6)**, 6685–6693.

D'Asaro, E., C. Lee, L. Rainville, R. Harcourt, and L. Thomas, 2011: Enhanced turbulence and energy dissipation at ocean fronts. *science*, **332 (6027)**, 318–322.

Evans, D. L., S. R. Signorini, and L. B. Miranda, 1983: A note on the transport of the Brazil Current. *Journal of Physical Oceanography*, **13 (9)**, 1732–1738.

Evans, D. L., and S. S. Signorini, 1985: Vertical structure of the Brazil Current. *Nature*, **315 (6014)**, 48–50.

Firing, E., J. Ranada, and P. Caldwell, 1995: Processing ADCP data with the CODAS software system version 3.1. *Joint Institute for Marine and Atmospheric Research, University of Hawaii & National Oceanographic Data Center.*

Fox-Kemper, B., R. Ferrari, and R. Hallberg, 2008: Parameterization of mixed layer eddies. part i: Theory and diagnosis. *Journal of Physical Oceanography*, **38 (6)**, 1145–1165, doi: doi.org/10.1175/2007JPO3792.1.

Garabato, A. C. N., K. L. Polzin, B. A. King, K. J. Heywood, and M. Visbeck, 2004: Widespread intense turbulent mixing in the Southern Ocean. *Science*, **303 (5655)**, 210–213.

Gill, A., J. Green, and A. Simmons, 1974: Energy partition in the large-scale ocean circulation and the production of mid-ocean eddies. *Deep Sea Research and Oceanographic Abstracts*, Elsevier, Vol. 21, 499–528.

Gula, J., M. J. Molemaker, and J. C. McWilliams, 2016: Topographic generation of submesoscale centrifugal instability and energy dissipation. *Nature communications*, **7**, 12 811.

Hart, J., 1974: On the Mixed Stability Program for Quasi-Geostrophic Ocean Currents. *Journal of Physical Oceanography*, **4 (3)**, 349–356.

Huang, R. X., 2005: Available potential energy in the world's oceans. *Journal of Marine Research*, **63 (1)**, 141–158.

Hurlburt, H. E., and P. J. Hogan, 2008: The gulf stream pathway and the impacts of the eddy-driven abyssal circulation and the deep western boundary current. *Dynamics of Atmospheres and Oceans*, **45 (3-4)**, 71–101.

Hurlburt, H. E., E. J. Metzger, P. J. Hogan, C. E. Tilburg, and J. F. Shriver, 2008: Steering of upper ocean currents and fronts by the topographically constrained abyssal circulation. *Dynamics of Atmospheres and Oceans*, **45 (3-4)**, 102–134.

Ingersoll, A. P., 1969: Inertial Taylor columns and Jupiter's great red spot. *Journal of the Atmospheric Sciences*, **26 (4)**, 744–752.

Isern-Fontanet, J., B. Chapron, G. Lapeyre, and P. Klein, 2006: Potential use of microwave sea surface temperatures for the estimation of ocean currents. *Geophysical research letters*, **33 (24)**.

Johnson, L., C. M. Lee, E. A. D'Asaro, L. Thomas, and A. Shcherbina, 2020: Restratification at a california current upwelling front, part 1: Observations. *Journal of Physical Oceanography*, **(2020)**.

Klein, P., A.-M. Treguier, and B. L. Hua, 1998: Three-dimensional stirring of thermohaline fronts. *Journal of Marine Research*, **56 (3)**, 589–612.

Lazaneo, C. Z., D. C. Napolitano, I. C. Silveira, A. Tandon, D. G. MacDonald, R. A. Ávila, and P. H. Calil, 2020: On the role of turbulent mixing produced by vertical shear between the brazil current and the intermediate western boundary current. *Journal of Geophysical Research: Oceans*, doi: doi.org/10.1029/2019JC015338.

Lebedev, K. V., H. Yoshinari, N. A. Maximenko, and P. W. Hacker, 2007: *Velocity data assessed from trajectories of Argo floats at parking level and at the sea surface*.

Legal, C., P. Klein, A.-M. Treguier, and J. Paillet, 2007: Diagnosis of the vertical motions in a mesoscale stirring region. *Journal of Physical Oceanography*, **37 (5)**, 1413–1424.

Legeais, J.-F., M. Ollitrault, and M. Arhan, 2013: Lagrangian observations in the Intermediate Western Boundary Current of the South Atlantic. *Deep Sea Research Part II: Topical Studies in Oceanography*, **85**, 109–126, doi: 10.1016/j.dsr2.2012.07.028.

Lévy, M., R. Ferrari, P. J. Franks, A. P. Martin, and P. Rivière, 2012: Bringing physics to life at the submesoscale. *Geophysical Research Letters*, **39 (14)**.

Lima, M. O., M. Cirano, M. M. Mata, M. Goes, G. Goni, and M. Baringer, 2016: An assessment of the Brazil Current baroclinic structure and variability near 22 S in Distinct Ocean Forecasting and Analysis Systems. *Ocean Dynamics*, **66 (6-7)**, 893–916, doi: 10.1007/s10236-016-0959-6.

Lueck, R. G., and T. D. Mudge, 1997: Topographically induced mixing around a shallow seamount. *Science*, **276 (5320)**, 1831–1833.

Magalhães, F. C., J. L. L. Azevedo, and L. R. Oliveira, 2017: Energetics of eddy-mean flow interactions in the Brazil Current between 20–36 S. *Journal of Geophysical Research: Oceans*, **122**, doi: 10.1002/2016JC012609.

Mahadevan, A., 2016: The impact of submesoscale physics on primary productivity of plankton. *Annual review of marine science*, **8**, 161–184.

Mahadevan, A., and D. Archer, 2000: Modeling the impact of fronts and mesoscale circulation on the nutrient supply and biogeochemistry of the upper ocean. *Journal of Geophysical Research: Oceans*, **105 (C1)**, 1209–1225.

Mahadevan, A., and A. Tandon, 2006: An analysis of mechanisms for submesoscale vertical motion at ocean fronts. *Ocean Modelling*, **14 (3-4)**, 241–256.

Mano, M. F., A. M. Paiva, A. R. Torres Jr, and A. L. Coutinho, 2009: Energy flux to a cyclonic eddy off Cabo Frio, Brazil. *Journal of Physical Oceanography*, **39 (11)**, 2999–3010, doi: 10.1175/2009JPO4026.1.

Martin, A. P., K. J. Richards, and M. J. Fasham, 2001: Phytoplankton production and community structure in an unstable frontal region. *Journal of Marine Systems*, **28 (1-2)**, 65–89.

Mata, M. M., M. Cirano, M. R. van Caaspel, C. Fonteles, G. Goni, and M. Baringer, 2013: Observations of the Brazil Current baroclinic transportation near 22 S: variability from the AX97 XBT transect and satellite altimetry. *20 Years of Progress in Radar Altimetry*, Vol. 710.

Mata, M. M., S. E. Wijffels, J. A. Church, and M. Tomczak, 2006: Eddy shedding and energy conversions in the East Australian Current. *Journal of Geophysical Research: Oceans*, **111 (C9)**.

McWilliams, J. C., 1977: A note on a consistent quasigeostrophic model in a multiply connected domain. *Dynamics of Atmospheres and Oceans*, **1 (5)**, 427–441, doi: https://doi.org/10.1016/0377-0265(77)90002-1.

McWilliams, J. C., 1985: Submesoscale, coherent vortices in the ocean. *Reviews of Geophysics*, **23 (2)**, 165–182, doi: doi.org/10.1029/RG023i002p00165.

McWilliams, J. C., 2016: Submesoscale currents in the ocean. *Proc. R. Soc. A*, **472 (2189)**, 20160 117.

McWilliams, J. C., F. Colas, and M. J. Molemaker, 2009: Cold filamentary intensification and oceanic surface convergence lines. *Geophysical Research Letters*, **36 (18)**.

McWilliams, J. C., J. Gula, and M. J. Molemaker, 2019: The gulf stream north wall: Ageostrophic circulation and frontogenesis. *Journal of Physical Oceanography*, **49 (4)**, 893–916.

Mensa, J. A., Z. Garraffo, A. Griffa, T. M. Özgökmen, A. Haza, and M. Veneziani, 2013: Seasonality of the submesoscale dynamics in the gulf stream region. *Ocean Dynamics*, **63 (8)**, 923–941.

Mill, G. N., V. S. da Costa, N. D. Lima, M. Gabioux, L. A. A. Guerra, and A. M. Paiva, 2015: Northward migration of cape são tomé rings, brazil. *Continental Shelf Research*, **106**, 27–37.

Molemaker, M. J., J. C. McWilliams, and X. Capet, 2010: Balanced and unbalanced routes to dissipation in an equilibrated eady flow. *Journal of Fluid Mechanics*, **654**, 35–63, doi: doi.org/10.1017/S0022112009993272.

Molemaker, M. J., J. C. McWilliams, and W. K. Dewar, 2015: Submesoscale instability and generation of mesoscale anticyclones near a separation of the california undercurrent. *Journal of Physical Oceanography*, **45 (3)**, 613–629.

Montégut, C. B., G. Madec, A. S. Fischer, A. Lazar, and D. Iudicone, 2004: Mixed layer depth over the global ocean: An examination of profile data and a profile-based climatology. *Journal of Geophysical Research: Oceans*, **109 (C12)**, doi: doi.org/10.1029/2004JC002378.

Morten, A. J., B. K. Arbic, and G. R. Flierl, 2017: Wavenumber-frequency analysis of single-layer shallow-water beta-plane quasi-geostrophic turbulence. *Physics of Fluids*, **29 (106602)**, 18, doi: 10.1063/1.5003846.

Morvan, M., P. L'Hégaret, X. Carton, J. Gula, C. Vic, C. de Marez, M. Sokolovskiy, and K. Koshel, 2019: The life cycle of submesoscale eddies generated by topographic interactions. *Ocean Science*, **15 (6)**.

Motoki, A., K. F. Motoki, and D. P. de Melo, 2012: Caracterização da morfologia submarina da cadeia vitória-trindade e áreas adjacentes, es, com base na batimetria predita do topo versão 14.1. *Revista Brasileira de Geomorfologia*, **13 (2)**.

Müller, T. J., Y. Ikeda, N. Zangenberg, and L. V. Nonato, 1998: Direct measurements of western boundary currents off Brazil between 20 S and 28 S. *Journal of Geophysical Research: Oceans*, **103 (C3)**, 5429–5437.

Nagai, T., A. Tandon, H. Yamazaki, M. J. Doubell, and S. Gallager, 2012: Direct observations of microscale turbulence and thermohaline structure in the kuroshio front. *Journal of Geophysical Research: Oceans*, **117 (C8)**.

Napolitano, D. C., I. C. A. da Silveira, C. B. Rocha, G. R. Flierl, P. H. R. Calil, and R. P. Martins, 2019: On the steadiness and instability of the Intermediate Western Boundary Current between 24 and 18 S. *Journal of Physical Oceanography*, **49 (12)**, 3127–3143, doi: 10.1175/JPO-D-19-0011.1.

Nikurashin, M., and R. Ferrari, 2010: Radiation and dissipation of internal waves generated by geostrophic motions impinging on small-scale topography: Application to the southern ocean. *Journal of Physical Oceanography*, **40 (9)**, 2025–2042, doi: 10.1175/2010JPO4315.1.

Oliveira, L. R., A. R. Piola, M. M. Mata, and I. D. Soares, 2009: Brazil Current surface circulation and energetics observed from drifting buoys. *Journal of Geophysical Research: Oceans*, **114 (C10)**, doi: 10.1029/2008JC004900.

Omand, M. M., E. A. D'Asaro, C. M. Lee, M. J. Perry, N. Briggs, I. Cetinić, and A. Mahadevan, 2015: Eddy-driven subduction exports particulate organic carbon from the spring bloom. *Science*, **348 (6231)**, 222–225.

Park, J. J., K. Kim, B. A. King, and S. C. Riser, 2005: An advanced method to estimate deep currents from profiling floats. *Journal of Atmospheric and Oceanic Technology*, **22 (8)**, 1294–1304.

Pedlosky, J., 1987: *Geophysical fluid dynamics*. Springer Science & Business Media.

Pérez, J. G., and P. H. Calil, 2017: Regional turbulence patterns driven by meso-and submesoscale processes in the Caribbean Sea. *Ocean Dynamics*, **67 (9)**, 1217–1230.

Phillips, N. A., 1954: Energy transformations and meridional circulations associated with simple baroclinic waves in a two-level, quasi-geostrophic model. *Tellus*, **6 (3)**, 274–286, doi: 10.1111/j.2153-3490.1954.tb01123.x.

Pollard, R. T., and L. A. Regier, 1992: Vorticity and vertical circulation at an ocean front. *Journal of Physical Oceanography*, **22 (6)**, 609–625.

Polzin, K., J. Toole, J. Ledwell, and R. Schmitt, 1997: Spatial variability of turbulent mixing in the abyssal ocean. *Science*, **276 (5309)**, 93–96.

Qiu, B., and S. Chen, 2005: Variability of the Kuroshio Extension Jet, Recirculation Gyre, and Mesoscale Eddies on Decadal Time Scales. *Journal of Physical Oceanography*, **35 (11)**, 2090–2103, doi: 10.1175/JPO2807.1.

Ramachandran, S., and Coauthors, 2018: Submesoscale processes at shallow salinity fronts in the bay of bengal: Observations during the winter monsoon. *Journal of Physical Oceanography*, **48 (3)**, 479–509.

Read, P., P. Rhines, and A. White, 1986: Geostrophic scatter diagrams and potential vorticity dynamics. *Journal of the Atmospheric Sciences*, **43 (24)**, 3226–3240.

Rintoul, S. R., 1991: South Atlantic interbasin exchange. *Journal of Geophysical Research: Oceans*, **96 (C2)**, 2675–2692.

Rocha, C. B., T. K. Chereskin, S. T. Gille, and D. Menemenlis, 2016a: Mesoscale to submesoscale wavenumber spectra in Drake Passage. *Journal of Physical Oceanography*, **46 (2)**, 601–620, doi: doi.org/10.1175/JPO-D-15-0087.1.

Rocha, C. B., S. T. Gille, T. K. Chereskin, and D. Menemenlis, 2016b: Seasonality of submesoscale dynamics in the Kuroshio Extension. *Geophysical Research Letters*, **43 (21)**, 11–304, doi: doi.org/10.1002/2016GL071349.

Rocha, C. B., I. C. Silveira, B. M. Castro, and J. A. M. Lima, 2014: Vertical structure, energetics, and dynamics of the Brazil Current System at 22 S–28 S. *Journal of Geophysical Research: Oceans*, **119 (1)**, 52–69, doi: 10.1002/2013JC009143.

Rogers, A. D., 2019: Threats to seamount ecosystems and their management. *World seas: an environmental evaluation*, Elsevier, 427–451, doi: doi.org/10.1016/B978-0-12-805052-1.00018-8.

Rudnick, D. L., 1996: Intensive surveys of the Azores Front: 2. Inferring the geostrophic and vertical velocity fields. *Journal of Geophysical Research: Oceans*, **101 (C7)**, 16 291–16 303.

Rudnick, D. L., 2001: On the skewness of vorticity in the upper ocean. *Geophysical research letters*, **28 (10)**, 2045–2048.

Sasaki, H., P. Klein, B. Qiu, and Y. Sasai, 2014: Impact of oceanic-scale interactions on the seasonal modulation of ocean dynamics by the atmosphere. *Nature communications*, **5 (1)**, 1–8.

Sasaki, H., P. Klein, Y. Sasai, and B. Qiu, 2017: Regionality and seasonality of submesoscale and mesoscale turbulence in the North Pacific Ocean. *Ocean Dynamics*, **67 (9)**, 1195–1216.

Schmid, C., and S. L. Garzoli, 2009: New observations of the spreading and variability of the Antarctic Intermediate Water in the Atlantic. *Journal of Marine Research*, **67 (6)**, 815–843, doi: 10.1357/002224009792006151.

Schmid, C., and S. Majumder, 2018: Transport variability of the Brazil Current from observations and a data assimilation model. *Ocean Science*, **14 (3)**, 417–436.

Schmid, C., H. Schäfer, W. Zenk, and G. Podestá, 1995: The Vitória eddy and its relation to the Brazil Current. *Journal of physical oceanography*, **25** **(11)**, 2532–2546.

Schmid, C., G. Siedler, and W. Zenk, 2000: Dynamics of intermediate water circulation in the subtropical South Atlantic. *Journal of Physical Oceanography*, **30** **(12)**, 3191–3211.

Schmitz, W. J., 1995: On the interbasin-scale thermohaline circulation. *Reviews of Geophysics*, **33** **(2)**, 151–173.

Shchepetkin, A. F., and J. C. McWilliams, 2005: The regional oceanic modeling system (roms): a split-explicit, free-surface, topography-following-coordinate oceanic model. *Ocean Modelling*, **9** **(4)**, 347 – 404, doi: http://dx.doi.org/10.1016/j.ocemod.2004.08.002, URL http://www.sciencedirect.com/science/article/pii/S1463500304000484.

Shcherbina, A. Y., E. A. D'Asaro, C. M. Lee, J. M. Klymak, M. J. Molemaker, and J. C. McWilliams, 2013: Statistics of vertical vorticity, divergence, and strain in a developed submesoscale turbulence field. *Geophysical Research Letters*, **40** **(17)**, 4706–4711, doi: doi.org/10.1002/grl.50919.

Silveira, I., L. Calado, B. Castro, M. Cirano, J. Lima, and A. d. S. Mascarenhas, 2004: On the baroclinic structure of the Brazil Current–Intermediate Western Boundary Current system at 22–23 S. *Geophysical Research Letters*, **31** **(14)**.

Silveira, I., J. Lima, A. Schmidt, W. Ceccopieri, A. Sartori, C. Franscisco, and R. Fontes, 2008: Is the meander growth in the Brazil Current system off Southeast Brazil due to baroclinic instability? *Dynamics of Atmospheres and Oceans*, **45** **(3)**, 187–207, doi: 10.1016/j.dynatmoce.2008.01.002.

Silveira, I. C., and G. R. Flierl, 2002: Eddy formation in $2\,1/2$-layer, quasigeostrophic jets. *Journal of physical oceanography*, **32 (3)**, 729–745.

Soutelino, R. G., A. Gangopadhyay, and I. C. Silveira, 2013: The roles of vertical shear and topography on the eddy formation near the site of origin of the Brazil Current. *Continental Shelf Research*, **70**, 46–60, doi: https://doi.org/10.1016/j.csr.2013.10.001.

Soutelino, R. G., I. C. Silveira, A. A. Gangopadhyay, and J. Miranda, 2011: Is the Brazil Current eddy-dominated to the north of 20 S? *Geophysical research letters*, **38 (3)**, doi: 10.1029/2010GL046276.

Stamper, M. A., and J. R. Taylor, 2017: The transition from symmetric to baroclinic instability in the Eady model. *Ocean Dynamics*, **67 (1)**, 65–80.

Stommel, H. M., 1965: *The Gulf Stream: a physical and dynamical description*. 2nd ed., University of California Press, Berkeley, and Cambridge University Press, London, 248 pp.

Stone, P. H., 1966: On non-geostrophic baroclinic stability. *Journal of the Atmospheric Sciences*, **23 (4)**, 390–400.

Stramma, L., Y. Ikeda, and R. G. Peterson, 1990: Geostrophic transport in the Brazil Current region north of 20 S. *Deep Sea Research Part A. Oceanographic Research Papers*, **37 (12)**, 1875–1886.

Taylor, J. R., and R. Ferrari, 2010: Buoyancy and wind-driven convection at mixed layer density fronts. *Journal of Physical Oceanography*, **40 (6)**, 1222–1242, doi: doi.org/10.1175/2010JPO4365.1.

Thomas, L. N., A. Tandon, and A. Mahadevan, 2008: Submesoscale processes and dynamics. *Ocean modeling in an Eddying Regime*, **177**, 17–38.

Thomas, L. N., J. R. Taylor, E. A. D'Asaro, C. M. Lee, J. M. Klymak, and A. Shcherbina, 2016: Symmetric instability, inertial oscillations, and turbulence at the Gulf Stream front. *Journal of Physical Oceanography*, **46 (1)**, 197–217.

Thomas, L. N., J. R. Taylor, R. Ferrari, and T. M. Joyce, 2013: Symmetric instability in the gulf stream. *Deep Sea Research Part II: Topical Studies in Oceanography*, **91**, 96–110.

Thompson, A. F., A. Lazar, C. Buckingham, A. C. Naveira Garabato, G. M. Damerell, and K. J. Heywood, 2016: Open-ocean submesoscale motions: A full seasonal cycle of mixed layer instabilities from gliders. *Journal of Physical Oceanography*, **46 (4)**, 1285–1307.

Tsuchiya, M., L. D. Talley, and M. S. McCartney, 1994: Water-mass distributions in the western South Atlantic; A section from South Georgia Island (54S) northward across the equator. *Journal of Marine Research*, **52 (1)**, 55–81.

Vallis, G. K., 2017: *Atmospheric and Oceanic Fluid Dynamics: Fundamentals and Large-Scale Circulation*. 2nd ed., Cambridge University Press, doi: 10.1017/9781107588417.

Viglione, G. A., A. F. Thompson, M. M. Flexas, J. Sprintall, and S. Swart, 2018: Abrupt transitions in submesoscale structure in southern drake passage: Glider observations and model results. *Journal of Physical Oceanography*, **48 (9)**, 2011–2027.

Weatherall, P., and Coauthors, 2015: A new digital bathymetric model of the world's oceans. *Earth and Space Science*, **2 (8)**, 331–345.

Wenegrat, J. O., L. N. Thomas, J. Gula, and J. C. McWilliams, 2018: Effects of the submesoscale on the potential vorticity budget of ocean mode waters. *Journal of Physical Oceanography*, **48 (9)**, 2141–2165.

Wienders, N., M. Arhan, and H. Mercier, 2000: Circulation at the western boundary of the South and Equatorial Atlantic: exchanges with the ocean interior. *Journal of Marine Research*, **58 (6)**, 1007–1039.

Wüst, G., 1935: The Stratosphere of the Atlantic Ocean. *(1987) The Stratosphere of the Atlantic Ocean: Scientific Results of the German Atlantic Expedition of the Research Vessel 'Meteor' 1925-27*, W. J. Emery, Ed., Amerind Publishing, 109–288.